Design of a Low Energy Single-phase Liquid Xenon Detector and its Applications

Pratibha Juyal

Supervisor

Prof. Karl Ludwig Giboni

Submitted in total fulfillment of the requirement for the

Degree of Doctor in

Experimental Particle Physics

Shanghai Jiao Tong University, Minhang campus, Shanghai, PRChina

Abstract

Dark matter (DM) has been a subject of intrigue and extensive research. Although the effects of DM have been observed in indirect observations, one would like to study the interactions of dark matter particles directly, especially of the Weakly Interacting Massive Particles (WIMP). Large Liquid Xenon (LXe) detectors emerged as the detectors of choice for this endeavor. Over the years, ever-larger detectors were deployed, reaching the 5 - 10 ton range. Despite this effort, no WIMPs were detected.

All these LXe Time Projection Chambers measure the charge and the light resulting from interactions. Since direct measurement of the minute charges with charge-sensitive amplifiers is impossible, the charges are extracted from the liquid into the gas phase, hence the name dual-phase (DP). PMTs can sense the extracted charges through proportional scintillation. However, the DP method also imposes severe restrictions on the operation and performance. Over the last years, an alternative method to measure the charge in the liquid phase was studied at SJTU. The proportional scintillation occurs within the liquid in the strong 1/r field close to stretched anode wires. Such single-phase (SP) detection exhibits significant advantages over DP in ease of design, performance, and stability. The benefits are more pronounced as the size of the detector increases.

The next generation of experiments could be in the 50 -100 ton range. The immense efforts and costs of such a system would strongly suggest enhancing the physics reach beyond the Dark Matter search. It should be an observatory for all physics phenomena such as Double Beta Decay of ^{136}Xe, Double Electron Capture in ^{124}Xe, Axions, and low energy neutrinos, e.g., solar and supernova neutrinos. It would complement existing neutrino observatories such as SuperK in Japan at much lower energies. The detection thresholds would be around 1 keV instead of 300 keV. Since this low energy range was never explored before, one should be prepared for many unexpected results in this new realm of physics.

The installation of the largest detector in the best underground lab would warrant the adoption of the suggestion by Y. Suzuki to isotope separate the xenon. A separation at 131.5 would yield two nearly equal samples with the lower masses containing all odd nuclei, and the upper range would be even. Such a cryogenic

isotope separation is currently under development to deplete argon of the radioactive ^{39}Ar for large LAr Dark Matter searches. The ARIA project in Sardegna collaborates with the Italian industry to build two 350 m tall distillation columns.

The isotope separation would enable source-on/source-off experiments, a well-established technique in spectroscopy for background subtraction. Moreover, it would tremendously improve the sensitivity not only for spin-dependent DM search but also for Double Beta Decay and Double Electron Capture. The results of such an observatory in CJPL-II would not be equaled by any other experiment for a very long time to come.

Key words: Dark matter, Detector modeling and simulations, Electroluminescence in liquid xenon, Isotope separation in xenon, Noble liquid detectors, Time projection chamber.

Contents

Abstract i
Contents iii
List of figures vii
List of Tables xii
1 Introduction 1
2 Dark Matter prediction and physics significance 5
2.1 Evidence of dark matter 5
2.1.1 Galaxy cluster 5
2.1.2 Galactic Rotation Curves 6
2.1.3 Collision of galaxies 6
2.1.4 Cosmic Microwave Background (CMB) 8
2.2 Dark matter candidates 9
2.2.1 Baryonic Dark Matter 9
2.2.2 Neutrinos 10
2.2.3 Axions 11
2.2.4 Dark Photon 12
2.2.5 Kaluza-Klein particles 13
2.2.6 Weakly Interacting Massive Particle 14
2.3 Detection Techniques or Methods of observation 15
2.3.1 Production at accelerators and colliders 16
2.3.2 Indirect detection techniques 17
2.3.3 Direct detection Techniques 17
2.4 Detection of WIMPs via direct detection 18
3 Past and present Detectors for DM searches 23
3.1 Cryogenic bolometers: 23
3.2 Crystal detector: 24
3.3 Ionization detector: 25

3.4 Bubble chambers: 25
3.5 Noble Liquid Gas detectors: 26
4 Detector medium 33
4.1 Media: LNe, LAr, LXe 33
4.2 Liquid Xenon as a detector medium 35
4.2.1 Properties of Xenon: 35
4.3 Time projection chamber 38
4.4 Ionization and Scintillation Process in liquid Xenon 39
4.5 Dark matter dual-phase detectors 40
4.5.1 Principle of Dual-Phase method 40
4.5.2 Limitations of Dual-phase: 42
4.5.3 Other challenges: 44
5 Detector Development program at SJTU 46
5.1 Background of the idea 47
5.2 Single-phase detector: 48
5.2.1 Principle of operation: 49
5.3 Small detector experimental Setup in SJTU: 49
5.3.1 Single photoelectron (SPE) calibration: 51
5.3.2 S2 and energy resolution 53
5.4 Geometrical configuration for anode wires at SJTU and comparison with CAL setup: 54
5.4.1 Aligned Anode 55
5.4.2 Staggered Anodes 58
5.5 Assumed disadvantages for DM detectors 58
5.5.1 Triple pulse component 59
5.5.2 Effect of shadowing 60
5.5.3 S2 efficiency 61
5.6 Electric Field dependence on the geometry 62
5.7 Electrode design 63

5.8 Advantages of 'Single-Phase' technique 64
5.9 Possibility of Pulse Shape Discrimination (PSD) for NR-ER separation in LXe 66
6 Proposal of a large multi-ton LXe single-phase detector 69
6.1 Single TPC 71
6.2 Dual TPC 72
6.3 Prerequisites for the detector 73
6.3.1 Photon sensors: 73
6.3.2 PMT Arrangement 77
6.3.3 Read Out of PMTs 77
6.3.4 Field Cage 79
6.4 Simulation study for Single phase and Dual-phase method 79
6.4.1 With PMT R11410 79
6.4.2 With PMT R12699 81
6.5 Detector with no reflections 83
6.6 Requirements for the large detectors system 83
6.6.1 Staged approach 83
6.6.2 Recirculation – purification 84
6.6.3 Cooling 86
6.6.4 Modular cooling system 89
6.6.5 Active internal shield 89
6.6.6 Shielding with a water shield 90
6.6.7 ^{85}Kr removal with distillation column 90
6.6.8 Radon removal 91
7 Physics Reach of a Large, Low Energy Detector 93
7.1 Double Beta Decay 93
7.1.1 Large scale isotope separation with Source on-off Experiments for DBD 94
7.1.2 Present DBD experiments: 95

7.1.3 Other DBD experiment 97
7.2 Axions 98
7.3 124-Xe double electron capture 99
7.4 Neutrinos 101
7.4.1 Atmospheric neutrinos 101
7.4.2 Solar Neutrinos 102
7.4.3 Supernova neutrinos 104
7.4.4 Extra-Terrestrial Neutrinos 104
7.4.5 Neutrinos experiments 104
8 Summary and outlook 109
9 References 111
10 Acknowledgements 126
11 Published Papers 128

List of figures

Figure 2.1 Rotation curves for the galaxy NCG 6503. Figure is taken from ref.[24]. 6

Figure 2.2 The gravitational potential and X-ray emission from colliding galaxy clusters 1E 0657558. Figure is taken from ref. [25]. 7

Figure 2.3 A full-sky map produced by the Wilkinson Microwave Anisotropy Probe (WMAP) showing cosmic background radiation, a very uniform glow of microwaves emitted by the infant universe more than 13 billion years ago. Color differences indicate tiny fluctuations in the intensity of the radiation, a result of tiny variations in the density of matter in the early universe Figure is taken from ref. [29]..8

Figure 2.4 Abundance of the isotopes of ^{4}He, D, ^{3}He, and ^{7}Li as predicted by the standard model of Big-Bang nucleosynthesis. The figure is taken from ref. [30]. .10

Figure 2.5 The mass and coupling parameter space. There is the representation of the sensitivity that can be accessed by ADMX and ADMX-HF [42]. It also shows the results from CERN Axion Solar Telescope (CAST) [43] and International Axion Observatory (IAXO) [44]. The yellow band represents two axions models, KSVZ (Kim–Shifman–Vainshtein–Zakharov) [45] and DFSZ (Dine–Fischler–Srednicki–Zhitnitsky) model [46]. Figure is taken from ref.[42]............................12

Figure 2.6 Sensitivities for the dark photon of mass less than 1 MeV in the plane of yield variable y as a function of dark matter mass $m\chi$. Figure is taken from ref. [54]...13

Figure 2.7 The number density of WIMPs plotted against time. WIMPs remain in thermal equilibrium as the universe expands and cools, and the abundance is Boltzmann suppressed. When the universe's expansion rate drops below the annihilation rate of the WIMPs, relic abundance freezes out and remains as the dark matter. Figure is taken from ref. [57] 15

Figure 2.8 Pictorial representation of the three methods of DM detection. First, two SM particles collide with each other and produce DM particles in colliders. Second, to find the SM particles which could form by the DM particles present in nature and third, when DM particle and SM particle collide with each other and produce new DM and SM particles via direct detection..16

Figure 2.9 Schematic overview of the direct detection methods.............................19

Figure 2.10 A number of underground labs are built under a mountain, namely LNGS, LSC, LSM, Baksan, CJPL, Kamioka, Y2L, ARF. Figure is taken from ref. [87]. 20

Figure 2.11 Left, radon level in underground labs, right underground volume for present (blue) and future (red) labs. Both figures are taken from ref. [87]. 21

Figure 3.1 Noble liquid gaseous detectors. Figures are taken from ref. [77, 82, 84, 107-109] 27

Figure 3.2 Schematic picture of Jinping underground lab. Figure is taken from ref. [118]. 30

Figure 3.3 The 90% C.L. upper limit vs. DM mass for the SI WIMP-nucleon elastic cross section from PandaX-4T commissioning data (red). The figure is taken from ref. [123] 31

Figure 4.1 Comparison of event rate between the target materials. Figure is taken from ref. [128]. 35

Figure 4.2 Working principle of a TPC. Figure is taken from ref. [132] 38

Figure 4.3 Schematic working principle of a DP (left) and an SP (right) LXe detector. The differences are mainly in the position of the liquid level and the diameter of the anode wires. Figure is taken from ref. [6]. 41

Figure 4.4 Distortion in S2 pulses in single and double scatter events. Figure is taken from ref. [140]. 44

Figure 5.1a) Picture and pictorial representation of SJTU and b) CAL's setups ref. [5]. 51

Figure 5.2 SPE spectrum of R8520 (1-inch PMT) at the voltage of -722 V. The gain is 3.3×10^5...52

Figure 5.3 Left, S2 vs S1 plot from ref. [6]. The 662 Kev full energy peak is located at the red spot in the plot; right, S2 pulse height of full energy peak vs drift time. An exponential decay fit presents a lifetime of 110 μ sec. The dark spots represent the median of S2 for each drift time bin. 53

Figure 5.4 662 keV full energy peak in S1, S2, and combined energy spectrum with energy resolution 12.83%, 10.4%, and 9.7% respectively. Figures are taken from ref. [6]. 53

Figure 5.5 Aligned and staggered arrangement for anode and shielding grids. Figure is taken from ref. [8]. 54

Figure 5.6 a.) Fieldline distribution in the anode region with aligned wires of the detector. The wire diameter is 20um. The spacing between wires is 3 mm. The dense field lines originate on the cathode of the detector and are focused by the grid wires. b.) Zoom in around a single wire. The lines from the cathode are compressed to a very small region and hit the anode wire from both sides. c.) The region in proximity of the wire. The threshold for electroluminescence is at 17.6 μm (dashed circle) from the wire center. Only electrons within the red triangle contribute to the S2 signal. Figures are taken from ref. [8]. 56

Figure 5.7 Fieldline distribution as in Figure 5.6.c, but with asymmetric grid potentials. The bottom grid is on ground potential and the upper grid is at +300 V. The thick line shows the horizontal. Compared to Figure 5.6c the angular range of incidence is now turned upward. Figure is taken from ref. [8]..............................57

Figure 5.8 a.) Field line distribution in the anode region with staggered wires as in Figure 5.5b. The wire diameter and the pitch are the same as before. The field lines from the cathode are again focused by the grid wires and impinge on the anode from below. The region of electro-luminescence is indicated by the dashed circle. b.) The region in proximity of the anode wire. The two distinct ranges at opposite sides of the anode wire are now adjacent to each other. Figure is taken from [8]. .58

Figure 5.9 Drift paths of ionization electrons from a point source to the anode wire in the CAL experiment. Reproduced from ref.[5]. a) On the left, the original plot, i.e., the case of a single anode wire. The three different flight paths can be identified. b) In the center, the case with three anode wires. The plot was not redrawn but modified by symmetry arguments. All the flight paths are now the same, but the two additional components end on the adjacent anode wires. c) The field simulation for staggered anode mesh in SJTU. 60

Figure 5.10 The calculation of electric field strength for the distance from the center axis for a 20µm (left) from ref. [6] and 50µm (right) diameter of the anode from ref. [140]. 63

Figure 5.11 Discriminator profiles for NR (red) and ER (blue) events, 10000 events each. Figure is taken from ref. [147]. 67

Figure 6.1 Dual-phase and single-phase geometry. In a single-phase, the liquid level is above the upper PMTs. Figure is taken from ref. [8]. 70

Figure 6.2 Schematic comparison of detectors with four drift spaces (a) Single TPC with the additional anode in the center, (b) Twin TPC with two identical TPCs on top of each other. Figure is taken from ref. [8]. 73

Figure 6.3 Difference between NR and ER signal due to different transit time spread (TTS). The left plot is for the R8778 PMT, 2" hexagonal PMT used in XMASS. The right plot is for the R11410, a 3" round PMT used for XENON and PandaX. Figure is taken from ref. [147]. 74

Figure 6.4 Different Hamamatsu PMTs. left, R8520 PMTs; center, R12699 PMT and right, R11410 PMT 76

Figure 6.5 Schematic design for top and bottom PMT array. Left, Hamamatsu R11410 round PMTs and Right, Hamamatsu R12699 square PMT. 76

Figure 6.6 a) Proposed Circuit with Kapton Flex Line and Pulse Transformer b) Alternative PMT Connection Scheme. Figure is taken from ref. [156]. 78

Figure 6.7 Bar graph representation of the simulation results. Comparison between single and dual-phase TPC for two type of PMTs (Hamamatsu R11410 and Hamamatsu R12699). a) Total number of photons capture by the PMTs. b) Number of reflection on PTFE surface. c) Average distance traveled by the photons. d) Number of photons directly hit the PMTs. e) Total internal reflections in dual-phase detector. 82

Figure 6.8 Schematics of the gas handling and supply system. The figure is taken from ref. [157]. 86

Figure 6.9 Schematics of cold finger. Figure is taken from ref. [7]. 88

Figure 6.10 Cooling bus system for PandaX detector. Figure is taken from ref. [159]. 89

Figure 6.11 The decay chain of radon-222. Figure is taken from ref. [161] 92

Figure 7.1 Left, 2 neutrinos double-beta; right, neutrinoless double beta decay. Figure is taken from ref. [162]. 94

Figure 7.2 The energy spectrum of the 241Am events in 5 bar Xe-(1%) TMA gas mixture with all selection criteria applied. The figure is taken from ref. [163]. 96

Figure 7.3 Overview of AXEL detector. The figure is taken from ref. [166]. 97

Figure 7.4 The Feynman diagram of 0vbb for ^{76}Ge. Figure is taken from ref. [167]. 97

Figure 7.5 The excess observed in XENON1T in the electronic recoil background at low energies, compared to the level expected from known backgrounds indicated as the red line. Figure is taken from ref. [10]. 99

Figure 7.6 Two-neutrino double electron capture. The figure is taken from ref. [169]. 100

Figure 7.7 Left, Production of neutrinos by cosmic-ray interactions with the air nucleus in the atmosphere[172]. The typical height of the neutrino production is 15 km above the ground. Right, Comparison of the flavor ratio r from three calculations [174-176]. This figure is taken from ref. [179]. 102

Figure 7.8 Solar neutrino flux. Figure is taken from ref. [181]. 103

Figure 7.9 Left, Schematic overview of super-k detector and right, inside the detector. Figure is taken from ref. [188]. 105

Figure 7.10 Schematic overview of the hyper-k detector. Figure is taken from ref. [187] 106

Figure 7.11 A schematic view of the JUNO detector. Figure is taken from ref. [189]. 106

Figure 7.12 Pictorial representation of a) Dune lab from ref. [193] and b) Icecube lab from ref. [194]. 108

List of Tables

Table 3.1 Comparison of different detectors and their sensitivity in WIMP cross-section 32

Table 4.1 Comparison of Noble gases 34

Table 4.2 Physical properties of xenon 37

Table 5.1 Comparison between single and dual-phase techniques 68

Table 6.1 Characteristics of different PMTs 75

Table 6.2 Comparison of the DP and SP detector's parameters with different PMTs 81

Table 6.3 Requirement of PMTs for the large mass LXe detector 84

1 Introduction

The universe never fails to surprise us at any given point. Only 5% of the universe is observable. The remaining 95% is an enigma; it remains undetected and unfathomable. It contains 25% Dark Matter (DM) particles, and the rest is Dark Energy, a cause of the universe's expansion. It shows that the observable part of the universe is only one-fifth of the DM particles. Therefore, DM is arguably the most mysterious matter in the universe. However, it has not been found yet. Even the evaluation of the Standard Model (SM) of particle physics cannot comprehensively explain DM.

There are ample indirect rationales to prove the existence of dark matter [1]. They indicate that our universe is filled with non-luminous matter or matter which we do not see directly. The universal observational data from gravitational effects prove that the strong and the electromagnetic forces do not interact with DM particles. The search for missing mass in the universe associates the DM particle with gravitational and weak forces. As the coupling constants for these interactions are small, it will be hard to detect DM candidates. It might even be possible that an unknown form of force exists behind the existence of DMs. Therefore, DM is often called ghost particles as no significant detection has been made of its existence.

A continuous hunt for DM has been going on for the last three decades, but we could not find it yet. However, acknowledging this fact, the curiosity to find DM intensifies day by day. Therefore, there is an aspiration to detect DM by developing new techniques, new analysis methods, and optimizing the detector parameters to provide the best possible match with cross-section regions for DM.

Many modes of DM detection have been evolving in the last few decades, such as direct, indirect, and collider techniques. With the help of these methods, we are looking for various kinds of hypothetical DM candidates, weakly interacting massive particles (WIPMs), neutrinos, axions, etc. The direct detection techniques using liquid xenon (LXe) time projection chambers (TPC) to search WIMPs have shown tremendous development in this area. It sometimes appears that they are the detector of choice for direct DM search. These TPCs are scalable to large mass masses with always diminishing cross-section thresholds. They also continue to reduce the background from competing processes.

This thesis describes the development of a very promising, novel LXe TPC concept. For DM search, all noble liquid TPCs measure two quantities of an event, the produced scintillation light and the amount of liberated charges in the form of electrons drifting in an electric field. However, the charges are too few to be observed using an electronic amplifier. A quite ingenious way [2] is commonly used to measure the drifting charges. They are extracted through the liquid level and produce proportional scintillation in the gas phase above. This light can be seen and quantified by arrays of Photo Multiplier Tubes (PMT) already in existence for light detection. Since the method involves two phases of xenon, the liquid, and the gas, it is called Dual Phase (DP). It was astonishingly successful in the past but also imposes its own limits and challenges. Furthermore, it becomes increasingly difficult to match these requirements as detectors grow larger and larger in mass.

Proportional scintillation also exists in the liquid in the strong 1/r field around stretched wire electrodes. This was first successfully tested in the late seventies by the Waseda group [3, 4]. However, LXe was a novel medium for nuclear detectors at that time, and the technological challenges did not warrant the expense and the difficulties of this scheme at that time. This method of detecting the charges in a single-phase detector (SP) soon passed into oblivion since it apparently did not bring any advantages. It only caused technological challenges difficult to meet. It was not used anymore because of different interests then and a lack of technology. In the meantime, all the technological obstacles have been overcome, and we can practically employ the SP method in LXe.

The SP scheme was picked up again in two recent studies by the Columbia Astrophysics Lab [5] and SJTU [6]. Most of the technological obstacles have been overcome in the last 40 years, and now SP provides many benefits in searching for rare, low-energy DM interactions. It would provide a detector that is easier and cheaper to design than a DP and would be easier to operate, provide higher sensitivity, reduced background, and much better long-term stability needed for year-long data taking runs. Since now very large detectors in the 50 - 100 ton range appear on the horizon, the time has come to look at SP again.

The initial study of SP was extended at SJTU over the past years. Not only were solutions found for some remaining technological aspects [7], but also it was established that SP would outperform a DP [8, 9]. However, a detector in the 50 - 100 ton range will be very expensive and require a lengthy preparation limited by commercial availability, e.g., the xenon and the PMTs. Moreover, it might be that such a large detector will be the largest to be constructed for a long time to come. I, therefore, also look at the extension of the physics range to extract as much scientific knowledge as possible from this endeavor. Effects like Double Beta Decay of ^{136}Xe, Double Electron Capture in ^{124}Xe, Axions, and low energy neutrinos, e.g., solar and supernova neutrinos, come directly to mind. These physics phenomena require further optimization of the detector to provide a lasting advance in research.

It might be remarkable in this context that one of the completed DM experiments, the XENON 1T, observed a curious enhancement [10] in part of their data. The observed enhancement is detected in data normally rejected as background during a standard WIMP search. It can be interpreted as Axions, but simple background interactions cannot yet be excluded. If the existence of Axions would be confirmed, it might change the field of DM altogether away from WIMP search. This anecdote reminds us that we should be prepared for a significant amount of new, unexpected physics since we also will be sensitive to low-energy neutrinos. This is a new field not systematically explored until now. Moreover, there always were sensational; unpredictable results discovered when entering a new realm of physics.

Finally, when proposing such a large detector in the deepest underground lab in the world, CJPL-II, we could take advantage of a suggestion by Y. Suzuki originally made in the year 2000 [11]. He realized that if one isotope separates natural xenon into 2 samples, one above the mass of 131.5, the other below, one obtains two samples of nearly the same size. The lower range sample contains only odd isotopes, and the other sample is all even. Running with the two samples consecutively, one can subtract the results from each other and isolate phenomena that only appear with a specific isotope or a specific spin of the nucleus. Such background rejection or 'source-on/source-off' techniques are regularly applied in spectroscopy. They can identify signals buried under an overwhelming background. In our case, we could use it to search for spin-dependent DM interactions as well as Double Beta Decay (^{136}Xe) or Double Electron Capture (^{124}Xe) with an unprecedented and sensitivity.

The large-scale isotope separation has recently been developed for the removal of radioactive ^{39}Ar from natural argon. For this purpose, two cryogenic distillation columns of 350 m height are being assembled in Sardegna, Italy. The depleted argon will then be used in the Darkside experiment for DM search [12]. These giant columns are assembled in collaboration with Italian industry in the so-called ARIA project [13]. Our case might be easier since we do not intend to extract one single isotope but split the full range into two equal parts.

2 Dark Matter prediction and physics significance

DM is the bridge that will link our present to our future to indicate future events. It will also profoundly affect our understanding of the past by solving the ambiguity of the universe's existence. We want to know how our universe emerged and where we will be going in the future. But, unfortunately, all the answers are camouflaged until we find dark matter.

In this way, many experiments have been done, and many more are in progress to find the range of different kinds of dark matter. Numerous theories and experiments are being considered for the pursuit of Dark Matter candidates. In terms of direct detection of DM, the most promising hypothetical candidates are Weakly Interacting Massive Particles (WIMPs) and Axions. The other predicted candidates are neutrinos, Kaluza-Klein particles, and other baryonic DM.

The evidence of DM is based on astronomical observations of the effect of a large ensemble of DM particles on astronomical objects. The evidence is called 'indirect' since we cannot identify a single DM particle with these methods.

2.1 Evidence of dark matter

Some studies postulated the presence of DM in the missing mass of the galaxies in the 19th century [14-16]. A few years later, Fritz Zwicky showed in his study on the Coma cluster that the mass of the galaxies by the velocity dispersion method is not the same as the mass obtained by computing the luminous matter in the galaxy. The variation in the luminous mass and the mass needed for observable velocity dispersion [17], indicate the presence of an invisible mass in the universe. In the 1970s, astronomers explained the deviation between the observed 'flat' rotation curves of gas in galaxies and the 'declining' curves that had been predicted based on the observed stars in those systems. After that, there was a series of studies that proved the existence of DM [18-21].

2.1.1 Galaxy cluster

In 1933, Fritz Zwicky applied the virial theorem (kinetic energy is half of the potential energy) to estimate the mass of the Coma galaxy cluster. According to his research, the velocity dispersion of visible galaxies in the Coma cluster is far less than the velocity dispersion along the line of sight. Therefore, it indicates an extra amount of mass existing in the galaxy cluster other than luminous mass [22].

2.1.2 Galactic Rotation Curves

Rotation curves of the galaxies are a possible way to find out the distribution of mass in galaxies. In the 1980s, Vera Rubin investigated the non-luminous matter by observing the velocity dispersions of the components within a single galaxy [23]. According to this study, it is proved that the Newtonian dynamics for gravitational force and velocity are ineffective for the galaxies. In principle, for the luminous mass in a galaxy, velocity should increase with the radius. However, the velocity curve plunged for big galaxies after reaching a peak velocity (~ 100kms^{-1}) for a certain radius. On the other hand, the observable value for rotational velocity increases with the radial distance from the galaxy center, no matter how big the galaxy is. Thus, it is contradictory to the results from Newton's law. These results were validated by another study [24], see Figure 2.1. This study also showed the disagreement between the observable and predicted velocity dispersion for the galaxy NCG 6503 and proved the existence of other non-luminous matter present in the galaxy, which could be a form of dark matter.

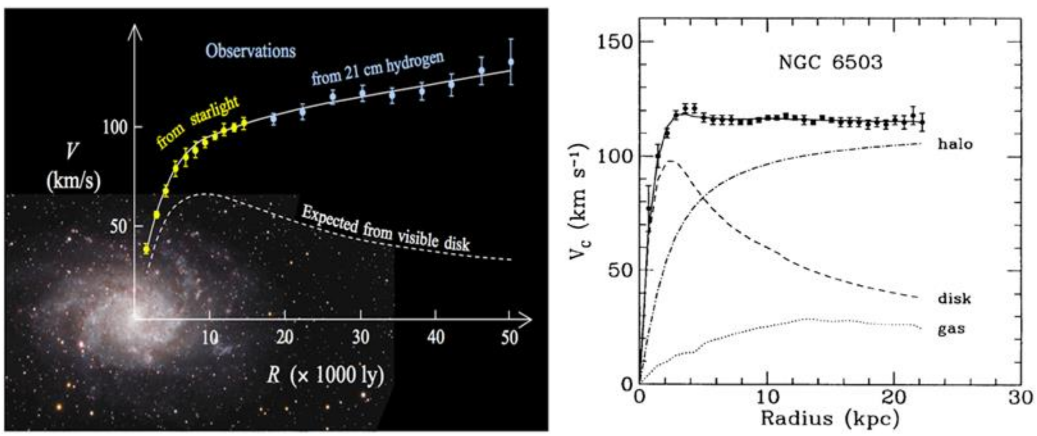

Figure 2.1 Rotation curves for the galaxy NCG 6503. Figure is taken from ref. [24].

2.1.3 Collision of galaxies

A group of galaxies is known as a galaxy cluster. The galaxy cluster contains many galaxies and intergalactic gas. Intergalactic gas is present in the form of luminous matter. When two such galaxy clusters collide, they produce a high pressure of intergalactic particles, resulting in atomic excitation, de-excitation, and emission of X-rays. After the collision, galaxies and intergalactic particles get separated from each other. Figure 2.2 shows the bright orange color of the intergalactic hot gas, whereas the blue part could be an effect of gravitational lensing[1] or might be a form of dark matter. An example of this type of collision was observed in system 1E 0657558 [25], referred to as the bullet cluster.

The gravitational potential in the system governs the spatial distribution among the components of the galaxy cluster. The weak lensing technique measures the gravitational potential. It helps to determine the distortion of the galaxy's images far from the observer. The amount of distortion is proportional to the mass contained within the gravitational potential [26], known as the gravitational lens. This technique was used to build a gravitational profile for the collision in 1E 0657558, Figure 2.2.

After the studies by Fritz Zwicky and Vera Rubin, it was assumed that the modified Newtonian could explain collisions between the clusters. But it cannot, as the amount of mass required for a gravitational profile is greater than the intergalactic particles. It indicates the deficiency of mass filled by non-luminous mass. Thus dark matter must be present to explain the missing mass, or else there must be another unknown reason.

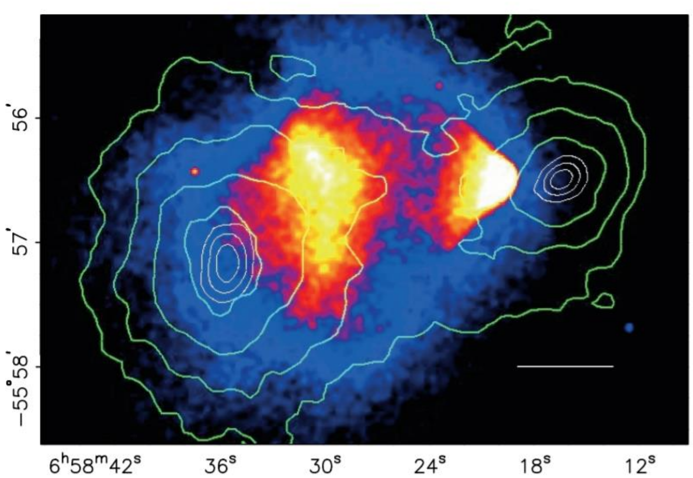

Figure 2.2 The gravitational potential and X-ray emission from colliding galaxy clusters 1E 0657558. Figure is taken from ref. [25].

---

[1] **Gravitational lensing:** Einstein's theory of general relativity provides a unified description of gravity as a geometric property of space and time or space-time. In this model, the curvature of space-time is directly related to the energy and momentum of matter and radiation. There are several important implications of Einstein's theory, such as the bending of light by the gravity of a massive object. It can lead to the phenomenon of gravitational lensing. When a distant light source, such as a star or quasar, is aligned with a massive compact foreground object, the gravitational field of the foreground object acts as a lens and causes the bending of light.

2.1.4 Cosmic Microwave Background (CMB)

According to the Hot Big Bang model [27], the universe is expanding exponentially with the span of inflation. Due to the continuous expansion, the temperature of the universe decreased, and it became transparent to light and electromagnetic radiation. It means that the photons which are generated by Thomson scattering become thermally decoupled and lose their energy. These photons were detected as cosmic microwave background (CMB) in 1965 [28]. CMB is the uniform background of radio waves.

We can see a map [29] shown in Figure 2.3. It indicates the slight changes in the intensity of the CMB across the sky. The map depicted is from the Wilkinson Microwave Anisotropy Probe (WMAP). Due to the slight variations in the density of matter, there are tiny fluctuations in the intensity of the radiation, which is indicated by the color differences in the Figure 2.3. According to inflation theory, these variations were the foundation of the galaxies. WMAP's data support the big bang and inflation models. The study of CMB has uncovered new evidence for dark energy, which is the cause of the expansion of the universe. It also helps to understand the nature of DM particles.

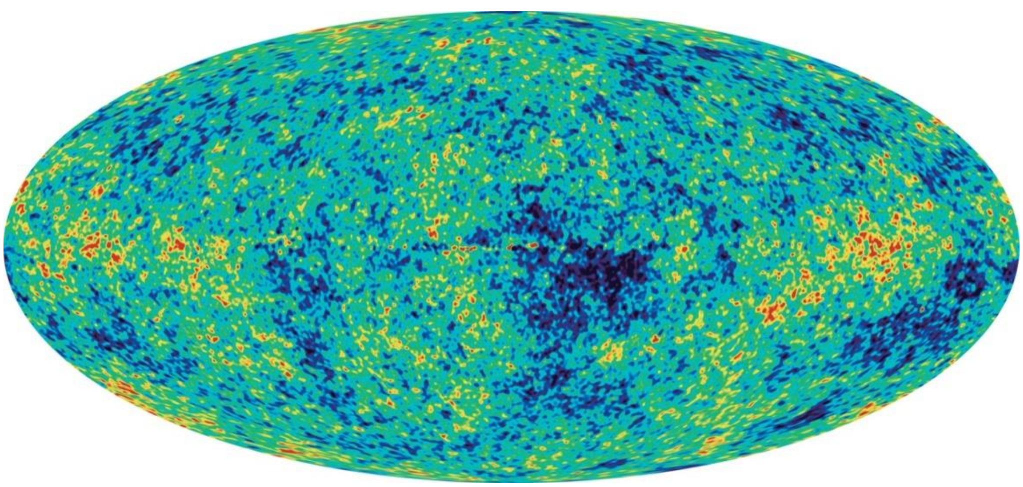

Figure 2.3 A full-sky map produced by the Wilkinson Microwave Anisotropy Probe (WMAP) showing cosmic background radiation, a very uniform glow of microwaves emitted by the infant universe more than 13 billion years ago. Color differences indicate tiny fluctuations in the intensity of the radiation, a result of tiny variations in the density of matter in the early universe Figure is taken from ref. [29].

2.2 Dark matter candidates

Several theories have been considered in the past to explain the particle nature of the DM.

2.2.1 Baryonic Dark Matter

In this case, the dark matter consists of non –luminous baryonic matter [26]. A hypothesis of the Big Bang, which is known as the origin of the universe, stated that a few seconds after the Big Bang, there was a production of the lightest baryons, which are isotopes of Deuterium (D), Helium (^3He), (^4He), and lithium (^7Li). All these elements are studied under Big Bang Nucleosynthesis (BBN) [30]. It is found that ^4He is the first produced component to have 25% of mass fraction of baryonic mass, i.e., $^4He/H \sim 0.008$, where H represents the 'Hubble expansion rate', the parameter of expansion of the universe. The abundance of the other two isotopes (D/H and $^3He/H$) is on the scale of 10^{-5}, whereas $^7Li/H$ abundance is about 10^{-10}, least among the other isotopes [31]. Figure 2.4 shows the abundance of these elements. These constraints have a small portion of the density of the assumed DM density, which indicates that there must be a large amount of non –luminous baryonic matter.

In previous searches and studies of dark matter, it was considered by most astronomers and astrophysicists that the missing mass might consist of compact objects that were much less luminous than ordinary stars. Candidates for such objects included planets, brown dwarfs, red dwarfs, white dwarfs, neutron stars, and black holes. These objects are named "MACHOs" (Massive Astrophysical Compact Halo Object). They emit negligible radiation, which means it is hard to detect them. However, they can be detected via gravitational lensing when they pass by stars.

Due to immense mass (10^{-8} to 100 solar mass) [32, 33], MACHOs bend and focus rays of light around themselves, which causes the rays to appear brighter. By observing the light, we can calculate the amount of hidden matter present in the galaxies. However, the fraction of galactic halo mass from MACHOs is not more than 20% which is far less than the expected mass (~80%) [26]. Therefore, we cannot say that all dark matter is present in the form of MACHOs. There must be another form of dark matter in the universe.

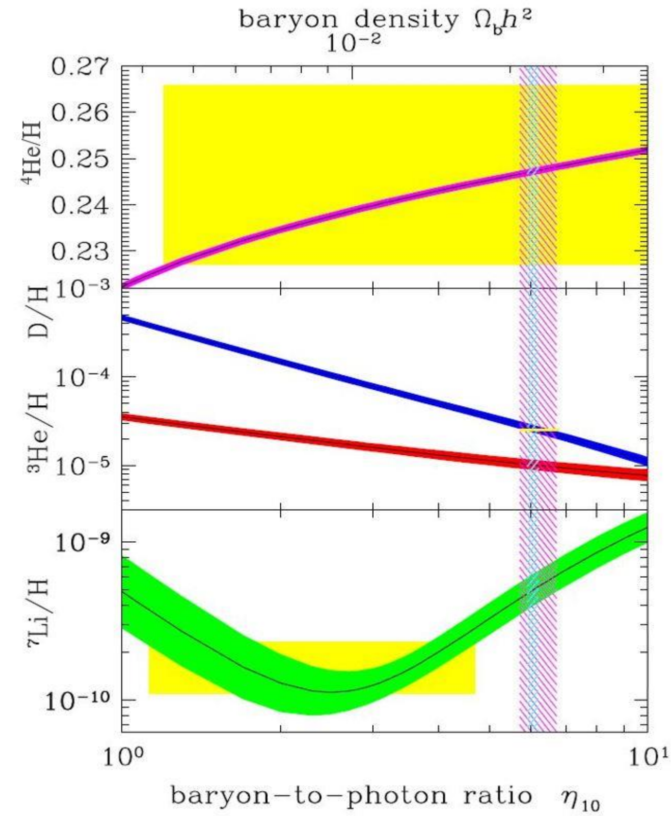

Figure 2.4 Abundance of the isotopes of ^{4}He, D, ^{3}He, and ^{7}Li as predicted by the standard model of Big-Bang nucleosynthesis. The figure is taken from ref. [30].

2.2.2 Neutrinos

Neutrinos are elementary particles in the Standard Model of particle physics that are stable, electrically neutral, and do not interact via strong interactions. Neutrinos are considered hot dark matter (HDM), travel with relativistic velocity, and have a non-zero mass of few electron volts. There are three types of neutrinos and their anti-particles: electron neutrino (ν_e), muon neutrino (ν_μ) and tau neutrino (ν_τ). Since they have non-zero mass, they can be a candidate for dark matter, which could have decoupled from the early universe and exist as a cosmic neutrino background. If one type of neutrinos is significantly more massive than the others, it creates the mass difference between the flavor masses [27], by which neutrinos as a DM candidate could lead to the formation of individual galaxies.

There is a prediction of another type of neutrino, which is considered the fourth type of neutrinos named "sterile neutrinos". Unlike the other three flavors (electron, muon, and tau neutrinos), they do not interact with other matter through weak forces. The ICARUS experiment [34] is investigating this new kind of neutrino. The presence of this type of neutrinos has also been indicated by other experiments like LSND [35], MiniBooNE [36], and other solar neutrino experiments [37, 38]. And some other experiments are still waiting for final results on sterile neutrinos.

2.2.3 Axions

The term ‘Axion’ came into the knowledge after the problem of CP (Charge –Parity) violation in quantum chromodynamics (QCD) in 1977 [39], the scientists Roberto Peccei and Helen Quinn predicted the light pseudo-scalar boson named ‘Axion’. Axions are neutrally charged and much more feebly interacting particles than Supersymmetry (SUSY) particles[2]. Axions have mass billions of times lighter than electrons. Axions are challenging to detect because they are light and stable over cosmological time scales, and only a narrow range of masses can be considered a candidate of DM. The axions would have a mass range from 10^{-2} to 10^{-6} eV [40]. It postulates that they would have been created during the QCD phase transition when hadrons were formed by quarks in the early universe ($\sim 10^{-6}$ s) at a temperature of 100 MeV.

There is a weak coupling of axions to photons. Axions can decay into two photons with a long lifetime ($\sim 10^{50}$ s) [41]. However, the coupling could be amplified with a strong electromagnetic field which suggests a potential strategy to search for them. Based on this, Pierre Sikivie invented the axion haloscope to search for axions [41]. In addition, the Axion Dark Matter Experiment (ADMX) was carried out in 1995 to search for axions with mass varying from 3.4 eV to 1.9 eV. Theoretically, when axions pass through a magnetic field, they could be able to decay spontaneously into two photons. If axions from the Milky Way are constantly and quickly passing through the Earth's surface, they would not be noticed. Then the powerful magnet in the ADMX experiment would convert some of them into microwave photons. Figure 2.5 shows the results from different experiments in the field of axion search.

Some new results from XENON 1T reported an excess of events in their electron recoil data [10]. One interpretation suggests that they are solar axions. However, other interpretations explain the excess by some specific background. Therefore, we have to wait for more data in the next round of experiments.

.

[2] Supersymmetry predicts that each of the particles in the Standard Model has a partner with a spin that differs by half of a unit.

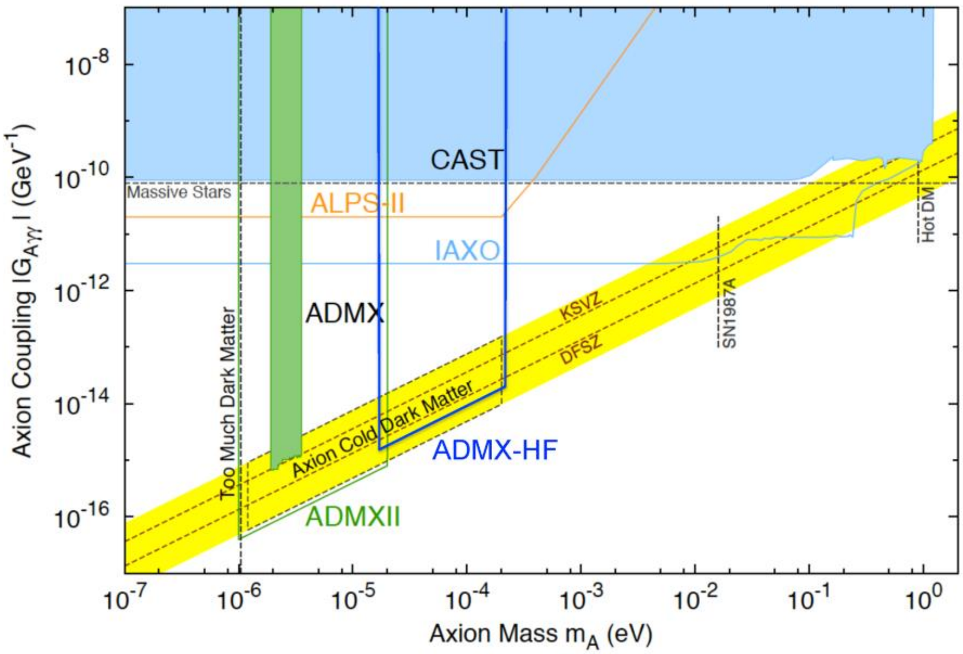

Figure 2.5 The mass and coupling parameter space. There is the representation of the sensitivity that can be accessed by ADMX and ADMX-HF [42]. It also shows the results from CERN Axion Solar Telescope (CAST) [43] and International Axion Observatory (IAXO) [44]. The yellow band represents two axions models, KSVZ (Kim–Shifman–Vainshtein–Zakharov) [45] and DFSZ (Dine–Fischler–Srednicki–Zhitnitsky) model [46]. Figure is taken from ref.[42]

2.2.4 Dark Photon

Dark photons are hypothetical force mediators (gauge bosons) similar to regular photons with extremely low mass. Some researchers believe that gravitational waves, celestial ripples in the fabric of space and time, could be the key to uncovering these tiny particles. If dark photons are skulking around the universe, their distinctive signals could be picked up by highly sensitive gravitational waves detectors like LIGO and Virgo. These two experiments are described in [47].

There is a wait for the launch of the Laser Interferometer Space Antenna (LISA) [48], which will be the first space-based gravitational wave observatory. It is expected that it will give some favorable results in the direction of the DM.

The discovery of dark photons may reveal new interactions and the existence of a new sector of elementary particles. Figure 2.6 shows the sensitivities of proposed experiments for massive dark photons. SHiP [49], LDMX [50], SNOLAB [51], BDX [52], SBND [36], SuperCDMS [53] are main experiments in this field.

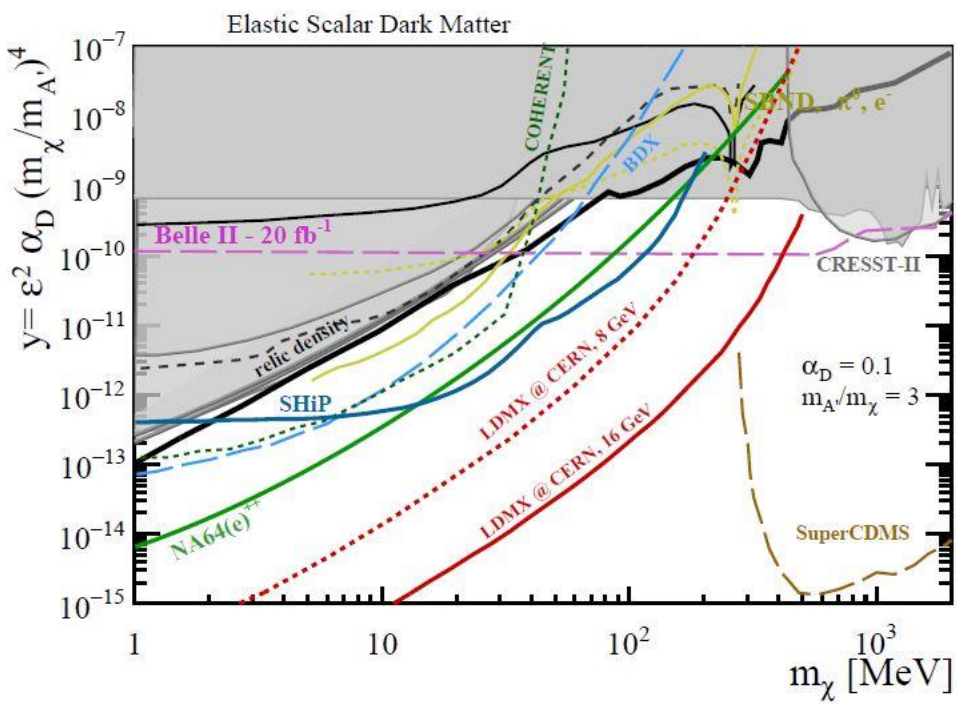

Figure 2.6 Sensitivities for the dark photon of mass less than 1 MeV in the plane of yield variable y as a function of dark matter mass mχ. Figure is taken from ref. [54]

2.2.5 Kaluza-Klein particles

According to Kaluza-Klein theory (KK theory), a unified field theory of gravitation and electromagnetism, if our universe is not merely a four-dimensional world but coexists with a fifth dimension, a viable dark matter candidate may exist in the high dimension [55, 56]. Thus, Theodor Kaluza and Oskar Klein predicted a hidden fifth dimension arching across the universe.

It is predicted that Kaluza-Klein (KK) particles are interactive in nature to be detected directly. When two KK particles collide together, they annihilate and decay into neutrinos and photons. The high-energy LHC continues to search for evidence of an extra dimension and KK particles. But so far, none has been reported.

2.2.6 Weakly Interacting Massive Particle

Weakly Interacting Massive Particles (WIMPs) are stable particles that arise from extensions of the standard model of electroweak interactions. In some scenarios, they are predicted as the lightest supersymmetric particle in Supersymmetry and the lightest Kaluza-Klein state in theoretical analysis.

WIMPs are an attractive candidate for DM because their properties and interaction rates can be computed in a well-defined particle physics model.

It is predicted that these particles interact with each other and with other particles with weak forces, and their masses are in the range of 10 GeV to a few TeV, hence they are named. Due to their high mass, they are cold dark matter which means their average speed is much less than light.

2.2.6.1 WIMP Miracle or WIMP freeze out:

It has been predicted that if any stable WIMPs are present in the universe, they would have been in thermal equilibrium with SM particles in the early universe. At that time, they might have had a high abundance. Let us assume that the particle χ has a mass M_χ with annihilation cross-section σ. When the temperature was too high in the early universe, the particles would have a high number density. When the temperature of the universe cools down, the number density of DM in equilibrium (n_χ^{eq}) decreases. The number density then follows:

$$\frac{dn_\chi}{dt} = -<\sigma v> \left[(n_\chi)^2 - (n_\chi{}^{eq})^2\right] - 3Hn_\chi \qquad (1)$$

Where v is the average velocity, H is the Hubble constant, and the term ($-3Hn_\chi$) in the equation (1) represents the fall in the number density due to expansion of the universe. As the expansion of the universe increases, there is a drop in density. We can see this in Figure 2.7. When the annihilation stops, the freeze-out state of the WIMP particles starts. At the freeze-out state, the mass density is independent of the mass of the particle and proportional to $<\sigma v>$ [57]. If the particle has weak scale interactions, then the annihilation cross-section is

$$\sigma v \sim 10^{-26} cm^3 s^{-1}$$

And the relic density of a particle is $\Omega h^2 \sim 10^{-27} cm^3 s^{-1}/\sigma v$, which is nearly 0.1 when putting the value of σv. It is equal to the correct order of magnitude for dark matter, which the CDM model predicts. This is WIMP's Miracle.

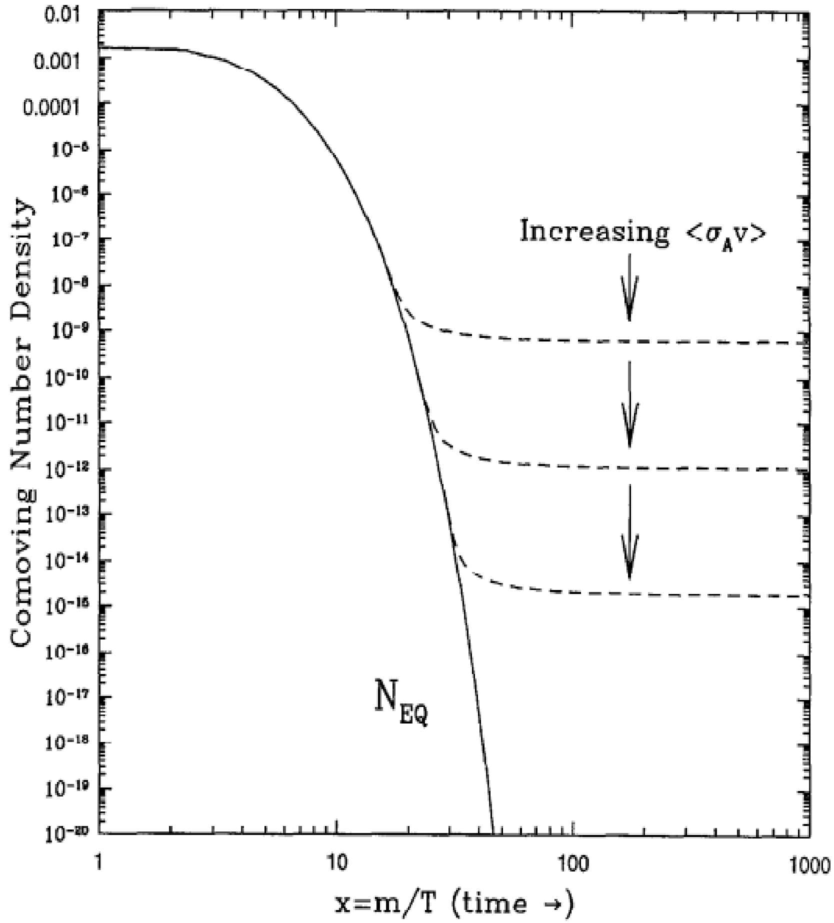

Figure 2.7 The number density of WIMPs plotted against time. WIMPs remain in thermal equilibrium as the universe expands and cools, and the abundance is Boltzmann suppressed. When the universe's expansion rate drops below the annihilation rate of the WIMPs, relic abundance freezes out and remains as the dark matter. Figure is taken from ref. [57]

2.3 Detection Techniques or Methods of observation

The cosmological and gravitational evidence proves the existence of a mysterious matter or Dark Matter. There are many theories and studies to predict the nature of DM and the types of possible candidates. There has been a continuous search for DM over the last 30 years, but still, we have not established the physical existence of DM particles. We know that there is something unknown around us, and to find this, we are applying different methods, techniques, and theories to solve the mystery of DM. There are three main approaches widely used in this area as:

1. Collider and Accelerator search;
2. Indirect Detection,
3. Direct Detection

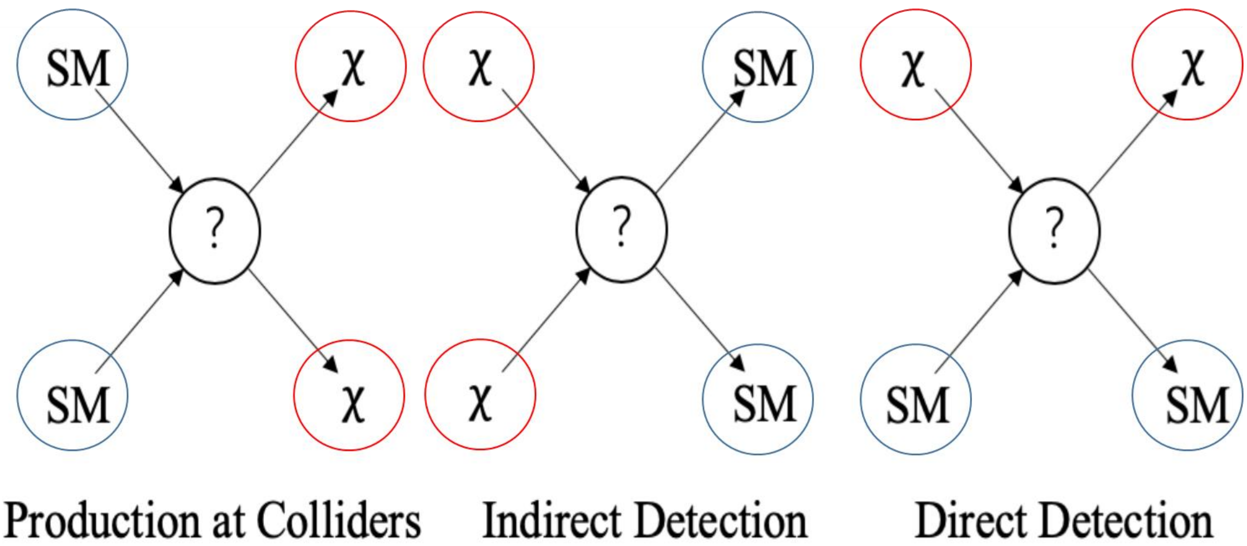

Figure 2.8 Pictorial representation of the three methods of DM detection. First, two SM particles collide with each other and produce DM particles in colliders. Second, to find the SM particles which could form by the DM particles present in nature and third, when DM particle and SM particle collide with each other and produce new DM and SM particles via direct detection.

WIMPs are the favored hypothetical candidates of DM because they would cover a large fraction of mass in the universe. Therefore, in the first part of this chapter, our focus will be on the WIMP search technique.

2.3.1 Production at accelerators and colliders

A collider can create DM particles rather than search for them. It means that the DM particle is a final product of the collision of SM particles in the colliders, e.g., p-p collider. After the collision, the different particles produced and the missing energy coupled with the correct combination of output products could indicate WIMP pair production. For example, in the p-p collider, two proton beams collide, and some of the products would be DM particles.

The Large Hadron Collider (LHC) is a particle accelerator where new particles can be produced. First, pump protons full of kinetic energy and then smash them together. In the collision, the energy can transform into mass in the form of new particles, which then decay into less massive particles. Particles collide at a variety of different energies. For example, in the LHC, two proton beams collide with the energy 13 TeV in the center of the mass system. The amount of energy that goes into a collision determines which kind of particles can be produced. For example, a collision with 125 GeV of energy can create a Higgs boson. ATLAS [58] and the CMS [59] are the leading experiments at the LHC.

2.3.2 Indirect detection techniques

The indirect search is looking for the excess of SM particles in space which may be the product of DM annihilation. These annihilations would be produced in the region of high-density DM, such as the Sun, Earth, galactic center, or the core of the galaxy. In addition, indirect searches look for the DM distribution by observing the interaction between DM and other universal constituents. The study of particle interaction can find the structure of DM [60].

There are many experiments involved in the indirect search for DM, such as Fermi-LAT [61], IceCube [62], Super-Kamiokande [63], DAMPE (DArk Matter Particle Explore) [64], AMS (Alpha Magnetic Spectrometer) [65]. They were designed to search for the products resulting from dark matter annihilation. The AMS experiment [66] is located on the International Space Station. A magnet spectrometer is searching for evidence of electron or positron pairs resulting from WIMP annihilation in the center of the galaxy. IceCube [67] is an example of a terrestrial indirect WIMP search. It is a large Cerenkov detector searching for neutrinos that could come from WIMP scatters.

2.3.3 Direct detection Techniques

Direct detection of DM is the technique in which DM particles elastically scatter off from target material and produce a signal by depositing energy [68]. In addition, the direct detection experiments also search for the annual modulation signals from DM. The annual modulation of a DM signal is due to the motion of Earth around the Sun. Therefore, it can enhance the signal to background ratio [69]. Background reduction and large exposure are the main factors that affect the sensitivity of the DM detectors. On average, the sensitivity on the cross-section is improved by order of magnitude every five years.

2.4 Detection of WIMPs via direct detection

Scatterings of DM particles off nuclei can be detected via three signatures: light (scintillation photons), charge (ionization of atoms), and heat (phonons). When the particle interacts with the detector medium, it produces some excited molecules, and when these excited molecules return to the ground state, they produce photons. Another process is ionization, which will generate free electrons. Some parts of the electrons will recombine with the ions. It makes additional scintillation light. The remaining electrons can drift in an electric field for a charge measurement. And some energy that is too small to produce light is converted into rotational and vibrational energy, i.e., heat.

Many direct detection experiments measure one or a combination of two phenomena in the system to find WIMP signals. Figure 2.9 shows the three signals as mentioned above and the related experiments.

1. The experiments IGEX [70], CoGeNT [71], and CDEX [72] are ionization detectors which measure ionization only.

2. The phonons (heat) measurement is done by CUORE [73], and CRESST-I [74],

3. DAMA/LIBRA [75], DEAP-3600[76] and XMASS [77] are for scintillation only.

The next experiments measure two phenomena:

1. Ionization and heat detectors (SuperCDMS [71] and EDELWEISS [53]

2. Light and heat detectors (CRESST-II [78] and ROSEBUD) [79]

3. Light and charge detectors (XENON [80], LUX [81], PandaX [82], DarkSide [83] and Darwin [84]. The Darwin experiment is in the R&D process.

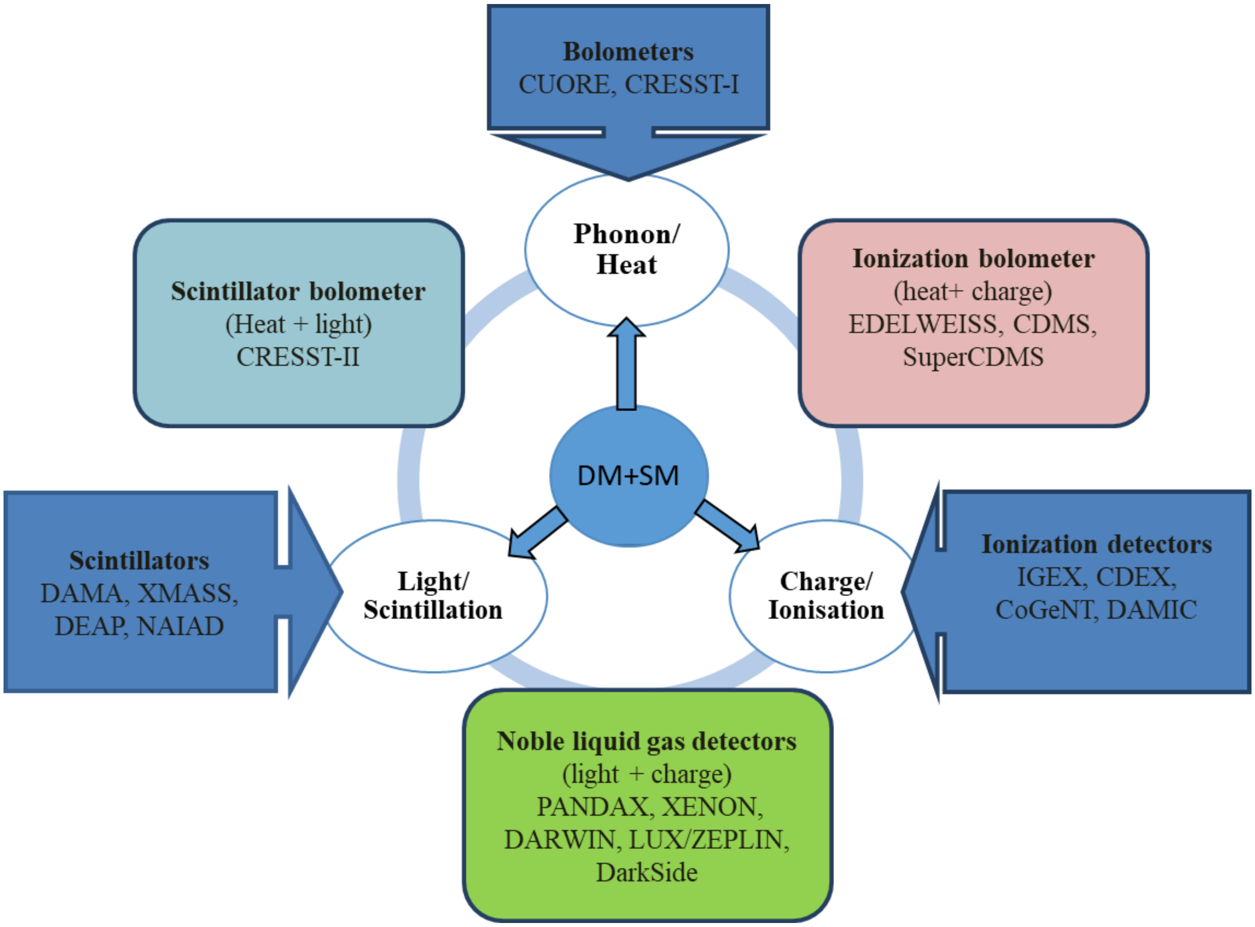

Figure 2.9 Schematic overview of the direct detection methods

The challenge of these detectors is to detect WIMP signals or nuclear recoil (NR) above electronic recoil (ER) background from γ-radiation (natural radioactivity) or β-decay of detector materials or surrounding rocks. Other major sources of background are neutrons or α-decays. They would make NR and thus cannot easily be rejected. Such a background will be critical for future detectors, especially for a DM mass below 10 GeV/c^2. Coherent neutrino scattering (CNNS) [85] is an additional background [85, 86]. The problem is that it also would interact with the nucleus and makes NR.

To eliminate the background, WIMP detectors need to employ methods such as:

1. Underground labs:

They are built to protect from cosmic rays and reduce the radioactive background. The depth of the lab affects the total muon flux. Therefore, the labs which are deeper underground have lower muon backgrounds. Figure 2.10 shows the muon flux against the depth under the flat surface [87]. The world's deepest lab is China JinPing underground Lab (CJPL), located in Sichuan, China. The depth of the lab is 2400m; therefore, it has the lowest cosmic muon flux in the order of 10^{-10} per cm^2 s [88]. CJPL-II is the second phase of CJPL, which is 20 times larger than CJPL-I. Figure 2.10 represents the underground labs that are presently operating or under construction.

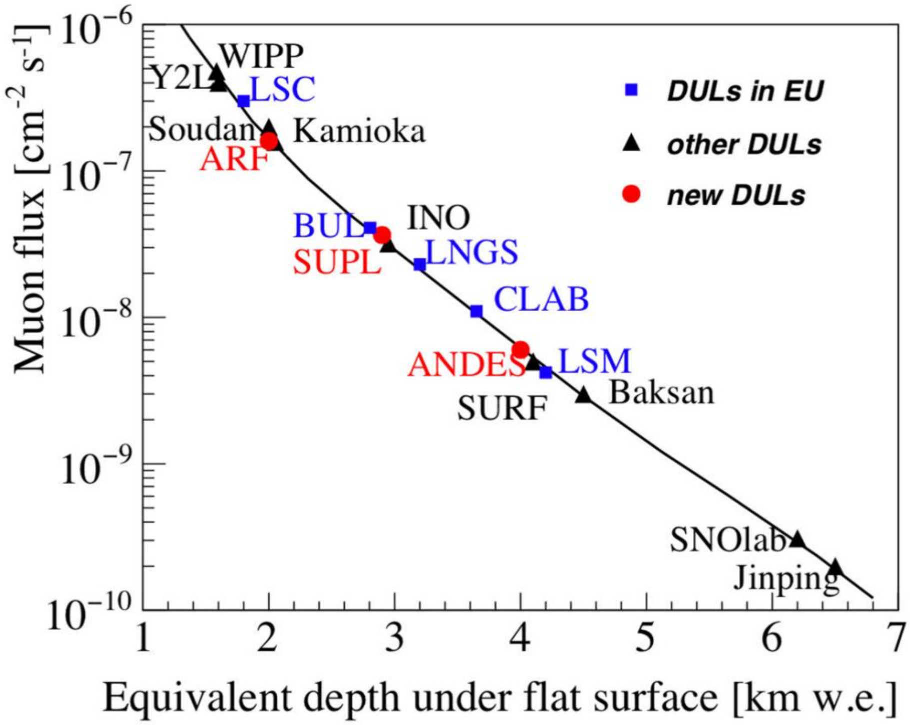

Figure 2.10 A number of underground labs are built under a mountain, namely LNGS, LSC, LSM, Baksan, CJPL, Kamioka, Y2L, ARF. Figure is taken from ref. [87].

The underground environment also reduces the neutron flux. The neutron flux mostly comes from (alpha, neutron) interactions and spontaneous fission. Another background comes from the radioactive elements which are present in the underground labs, e.g., radon. Due to its high radioactivity, it is necessary to reduce the concentration of radon in the lab. Figure 2.11 shows the radon level in the laboratories. The lowest radioactivity is found in the Boulby underground laboratory (BUL).

Even in the deepest labs, the background radiation is still too strong for a DM detector. Additionally, some essential facilities are needed in the underground labs, which add background such as cooling system, electronic read out, control and monitoring systems, gas and liquid handling and purification systems, clean rooms, radioactivity screening facilities, water purification plant, and liquid scintillator purification plant. Therefore, the detector is enclosed in a large shield, either with several 20 cm thick layers of lead and poly-ethylene or a water shield with about 5 m of purified water in all directions. A water shield can be made to an active shielding by replacing the water with a liquid scintillator. Water shields are used underground for XENON, PandaX, Darkside, SNOLab, and XMASS experiments.

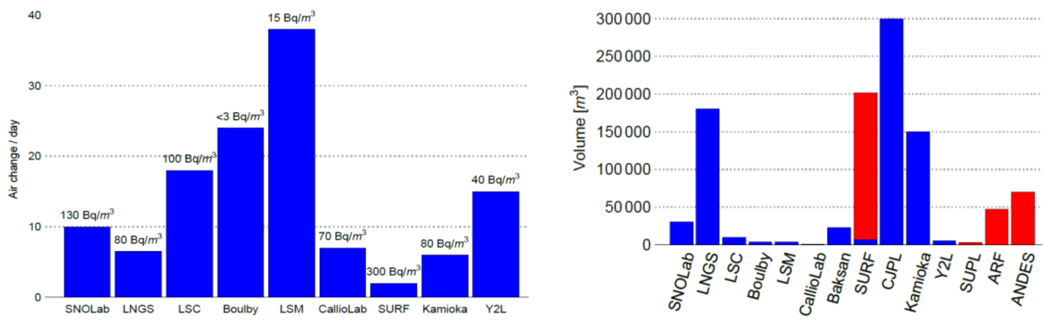

Figure 2.11 Left, radon level in underground labs, right underground volume for present (blue) and future (red) labs. Both figures are taken from ref. [87].

2. Detector Material

The materials used for the detector construction add to the background. The activities of all materials have to be measured, and the ones with the lowest radioactivity has to be chosen, e.g., PMTs, steel, for the vessel, etc. But even the xenon itself can contain radioactive substances. For example, commercial xenon contains a ppm level contamination of krypton, which has a radioactive isotope ^{85}Kr at an abundance of 10^{-12}. For DM experiments, the krypton concentration is reduced to well below ppb level by a distillation column.

Although the PMTs are specifically manufactured for low activity, a significant background component is produced in the PMTs. Therefore, The XENON group undertook the effort to measure the activities of all the PMT parts and thus, in collaboration with the manufacturer, developed special PMT types for their experiments [89].

PandaX-II reduced the vessel's background by using stainless steel (SS) specifically made for their experiment [90]. All the starting minerals were purified from radioactive contaminations. Particular care was taken to reduce the amount of ^{60}Co added during the foundry process. These were only two examples of the effort to reduce the activity of the experiment itself. Finally, the strategy is to count all the components and search for lower activity alternatives.

3. Discrimination Methods

These methods depend on the chosen detector principle. The aim is to use all the available information to differentiate between the WIMP signals and background gamma rays. One method is fiducialization. It cuts away from an outer layer of the active volume and uses the self-shielding property of xenon. Low energy background reacts predominantly soon after entering the detector.

Another method uses the charge to light ratio to distinguish between NR and ER interactions. This so-called S2/S1 cut reduces the background by nearly a factor of 100. Pulse Shape Discrimination could add another factor of 100 by using different timing, i.e., pulse shapes, of NR and ER events. This method is, however, not yet established for liquid xenon.

Also, the recognition of double events belongs in this category. If the charge measurement indicates two ionization points, the event is most probable a Compton scattering background event since WIMP interactions occur in one single interaction site.

3 Past and present Detectors for DM searches

Out of all DM candidates, WIMPs attract the most attention and are proposed as the lightest supersymmetric particle in Supersymmetry in some scenarios, and the lightest Kaluza-Klein state in theories with universal extra dimensions. However, low energy neutrino physics is also in the reach of these experiments. Furthermore, some experiments are looking for axion and axion-like particles.

3.1 Cryogenic bolometers:

These detectors used semiconductors, e.g., Silicon and Germanium or superconductors (Lead and Tin). They measure the total deposited energy of incident radiation by deposited heat in the material [91]. When a DM particle interacts with the target material, a small amount of energy deposits in the form of heat (phonon). Some cryogenic detectors measure two signals, the Ionization bolometer measures ionization and heat, and the Scintillator bolometer measures scintillation and heat. Heat signals can be observed by the detector medium when the temperature is near the transition temperature. A target material held at a temperature near its transition temperature absorbs this heat and goes normal.

CDMS [92] (cryogenic dark matter search), SuperCDMS [71] and EDELWEISS [53] are ionization bolometers whereas CRESST is a scintillator bolometer. They are sensitive to low mass WIMPs due to their low threshold (<1 keVnr). One can improve the sensitivity by applying methods such as the Neganov-Trofimov-Luke effect[3] [93] in the CDMS experiment and the Migdal effect[4] [94] in EDELWEISS. It helps to extend to interactions, the exclusion of particles with masses between 45 and 150 MeV c^{-2} with spin-independent cross-sections ranging from 10^{-29} to 10^{-26} cm^2.

[3] The Neganov–Trofimov–Luke effect was proposed to enhance heat signals of bolometers at low temperatures by applying voltage in the electric field. There is an acceleration of charges collected in the electrode in the form of electrons-holes pair. These charges emit phonons and increase the heat signals.

[4] Migdal effect: When a particle elastically scatters off an atomic nucleus, it has been assumed that electron clouds immediately follow the motion of the nucleus, but in reality, it takes some time for the atomic electrons to catch up, resulting in ionization and excitation of the atom. This effect is called the Migdal effect.

SuperCDMS and CRESST used germanium and CaWO4 semiconductors, respectively. The SuperCDMS have set the constraints on WIMP mass as low as 1.5 GeVc^{-2} (84), whereas CRESST-III has an upper limit of 160 MeV c^{-2} (85) with a threshold of 30 eV.

3.2 Crystal detector:

These detectors use scintillator crystals such as NaI(Tl), CsI(Tl), and CaF2(Eu) [95]. They have high light yields and are relatively inexpensive. For a detailed overview of the scintillator detectors, look at the reference [96]. The groups such as DAMA (DArkMAtter) [75], ANAIS (Annual modulation with NAI Scintillators) [97], and NAIAD (NaI Advanced Detector) used NaI(Tl). The Korea Invisible Mass Search (KIMS) [98] uses CsI(Tl) as a target material for their detector with a massive muon shield.

DAMA/LIBRA is situated in LNGS (Laboratori Nazionali del Gran Sasso) in Italy, searching for annual modulation signals using NaI(TI) crystal. It collected 2.46 t × year over 20 annual cycles at 12.9 σ significance [75]. The data collection for the next phase is expected to go on until the end of 2024.

DAMA claimed observation of DM, but other experiments could not verify this. Their main dispute is over the detected annual modulation, which is predicted for DM. Critics point out that in the LNGS, nearly everything has an annual modulation, even the muon spectrum.

ANAIS (Annual modulation with NAI Scintillators) is operating nine NaI(Tl) consisting of 112.5 kg total mass at the Canfranc Underground Laboratory in Spain (LSC). The first results presented after 1.5 years the model-independent results of an annual modulation of the exposure of 157.55 kg year [97]. The experiment continues till the 2 year run of the exposure of 220.69 kg × y. After the best fit, the results are incompatible with DAMA/LIBRA results at 2.6 σ [99]. ANAIS-112 can detect the annual modulation in the 3 σ region compatible with the DAMA/LIBRA result for 5 years of measurement [100].

COSINE experiment is situated at the Yangyang underground laboratory (Y2L) in Korea with the 8 NAI(Tl) detectors. It is a collaboration of KIMS and DM-Ice experiments [101]. The COSINE-100 used 1.7 years of data for the annual modulation analysis with exposure of 97.70 kg × year. The event rate for the energy range (2-6 keV) is 2.7 events/ keV × kg × day [102]. It is expected that the COSINE-100 can achieve the 3σ region of DAMA/LIBRA with 5 years of data exposure.

3.3 Ionization detector:

These detectors measure **The Neganov–Trofimov–Luke effect** ionization signals. Silicon, germanium, helium, and neon are used as detector media.

DAMIC is a Silicon-based Charge-Coupled Device (CCD) in the SNO underground laboratory for DM search. The CCD is used to target ionization signals produced by dark matter interactions from the galactic halo. DAMIC is sensitive to small ionization signals due to the low read-out noise of the CCD. It allows the low energy threshold (~ ev) to detect nuclear or electron recoils from the interaction of low mass WIMPs. The excellent charge resolution and extremely low leakage current of DAMIC CCDs allow limits on dark matter-electron scattering in the mass range from 0.6 MeV c^{-2} to 6 MeV c^{-2} [103]. Moreover, it sets the constraints on hidden-photon dark matter in the mass range 1.2^{-9} eV c^{-2}.

CDEX (China Dark matter EXperiment) uses P-type point-contact Ge (PPCGe) detectors operating at the China Jing Ping Laboratory (CJPL) in China. CDEX-I used two detectors of 1 kg each reaching an energy threshold of 160 keV electron-equivalent (keVee). Considering the Migdal effect, the limits for cross-section set by the experiment for DM masses ~50-180 $MeVc^{-2}$ are in the range of 10^{-32}~10^{-35} cm^2 for time-integrated (TI) analysis. For annual modulation, the range of cross-section is between 10^{-32} and 10^{-38} cm^2 [104] for masses ~75 $MeVc^{-2}$ - 3.0 $GeVc^{-2}$. The next upgrade is CDEX-10 with 10kg of PPCGe detectors immersed in liquid nitrogen [105]. The future detectors are CDEX-100 and CDEX-1T for large masses.

3.4 Bubble chambers:

These detectors use a liquefied gas as the target material. The temperature of these liquids is set below their boiling point due to a sudden decrease in pressure, and DM creates a bubble when the energy exceeds the threshold value. The bubble formation is caused by nuclear recoil, while ER background does not contribute. Stereoscopic cameras are used for bubble count and position determination. Some of the target liquids are CF3I, C3F8, C4F10, C2ClF5, and C3ClF8.

PICO: The PICO is the merger of PICASSO (Project In CAnada to Search for Supersymmetric Objects) and COUPP (Chicagoland Observatory for Underground Particle Physics). It is installed at SNOLAB [106]. Both detectors are based on the principle of a bubble chamber. PICO-60 is a 52 kg detector of C3F8, giving a threshold of 2.45 keV with 1404-kg-day exposure. PICO-40L is the upgraded version of PICO-60 with some design changes. It is presently in data collection mode. The PICO-500 is a next-generation detector with 250 liters of active volume. It is in the design stage.

3.5 Noble Liquid Gas detectors:

Noble gases as a detector medium provide outstanding advantages as they have self-shielding properties. Moreover, they are suited for massive detectors because they can be scaled up by increasing the volume. Xenon, Argon, and Neon are used as detector media either as a liquid or as gas. The remaining noble gases helium, krypton, and radon cannot be used in DM detectors. In helium, free electrons cannot be drifted. Radon does not have a stable isotope, and krypton has a radioactive isotope ^{85}Kr with a natural abundance of 10^{-12} in krypton. Although this concentration is relatively small, it is still a very strong source of background in a DM detector. To judge the background, one has to consider commercial xenon. It contains an admixture of krypton at ppm-level. The background from ^{85}Kr is still so strong that the krypton concentration has to be pushed far below the ppb level to be acceptable.

When a particle hits the target in the liquid phase, it excites an atom, moving electrons to higher orbital levels. The subsequent de-excitation results in a prompt scintillation signal (S1) or light signals. The energy deposition also produces ionization electrons which can be separated from the ion in an electric field for a charge measurement (S2). The leading DM experiments are XENON [80], PANDAX [82], LUX/ZEPLIN [81], DarkSide [83], and the future Darwin [84]. The XMASS [77] experiment also falls in this category; it measures only scintillation light.

XMASS: Although, the XMASS detector is not running anymore as a WIMP detector. It is kept alive as a neutrino observatory. In the Kamioka laboratory in Japan, SuperK is presently being upgraded, and HyperK is not yet completed. Thus, XMASS is the only running neutrino detector that could observe a nearby supernova like the SN87. However, it was initially planned as the LXe detector to measure the scintillation light of the dark matter. Its life span as an experiment contributed to the search of ^{7}Be and pp solar neutrinos and double beta decay. The active mass of the detector is 857 kg [77]. The light yield was measured to be 14.7 PE/keVee.

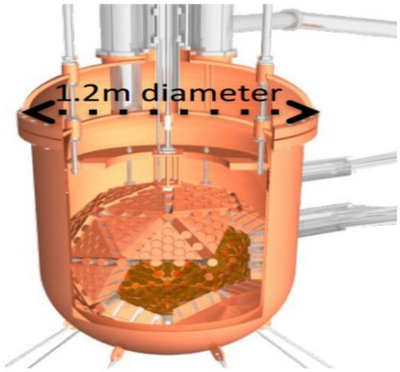

XMASS

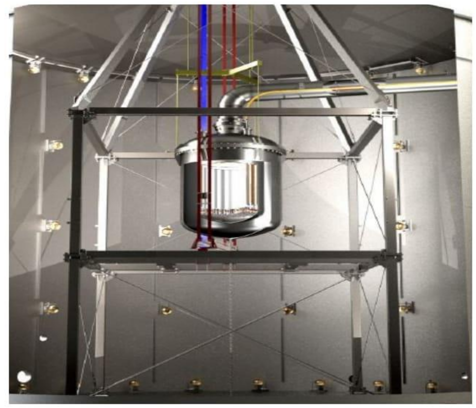

XENON

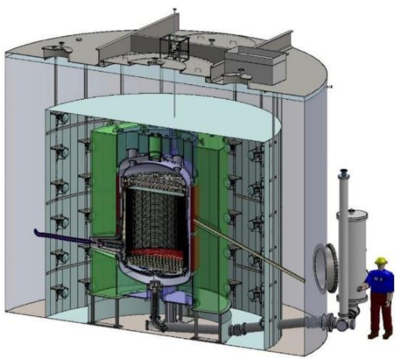

LUX/ZEPLIN

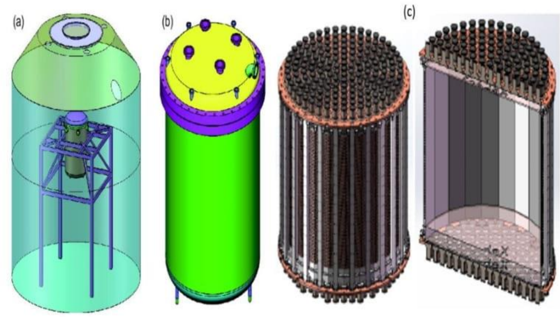

PANDAX

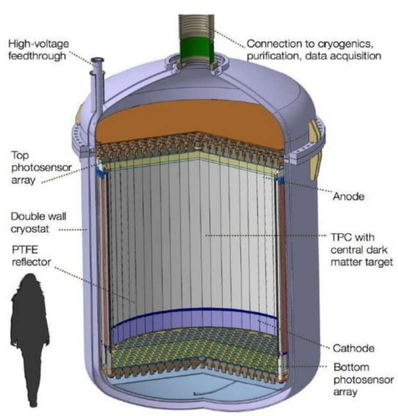

DARWIN

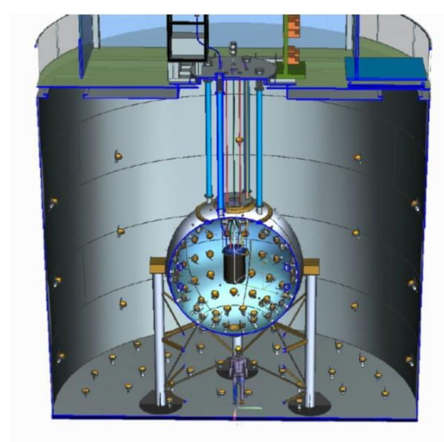

DARKSIDE-50

Figure 3.1 Noble liquid gaseous detectors. Figures are taken from ref. [77, 82, 84, 107-109]

WIMPs were searched with XMASS using 705.9 live days of data in a fiducial volume of 97 kg of liquid xenon [110]. This number reveals the disadvantage of a scintillator with no charge measurement. Out of 857 kg active mass, only 97 kg were used as a target. This seems to be very inefficient. The lack of charge measurement makes it impossible to use the standard charge over a light cut to reduce the background. It all depends on fiducial volume cuts. However, the location of the interaction is usually determined by the charge distribution. The resolution is a few mm, and a 5 cm fiducial cut from the walls is sufficient.

In XMASS, the location of the event is determined by the light pattern. With the limited position resolution from the light pattern at low energies, about 20 cm of LXe must be cut away, i.e., a large fraction of the active mass. The obtained upper limit on a spin-independent WIMP-nucleon cross-section was 2.2×10^{-44} cm^2 for a WIMP mass of 60 $GeVc^{-2}$ at the 90% CL.

XMASS also searched for solar axions, a product of the bremsstrahlung and Compton effects in the Sun. The model-independent limit on the coupling for mass much smaller than 1 keV is 5.4×10^{-11} with 90 % CL.

The search of neutrino-electron interactions in the XMASS-I using solar neutrino gives upper limits for neutrino electric (milli) charge is 5.4×10^{-12} e at 90% CL [111]. In addition, the neutrino magnetic moment was calculated as 1.8×10^{-10} μB, and the coupling constant of the dark photon range between 10^{-6} ~10^{-5}.

XENON is a TPC using liquid xenon as a sensitive detector medium to search for WIMPs. XENON10 started in the LNGS in 2006 [112]. It contained 15 kg of LXe to collect the scintillation light and the charge.

XENON100 with an active volume of 165 kg LXe was installed in 2008 and acquired 477 live-day data in total [113]. The experiment obtained an upper cross-section limit for the dark matter of 10^{-46} cm^2 at 50 $GeVc^{-2}$ and was the first detector with an instrumented shield around the active volume. There is a 5 cm liquid xenon layer above the top PMTs and below the cathode, in front of the bottom PMTs. Additionally, there were PMTs mounted below the bottom PMT array watching the space where all the cables were.

XENON 1T has 2 tons of active mass in the TPC out of 3.2 tons xenon in total. The first results from the run 0 of only 34 live days. The experiment was stopped to enlarge it to the XENON nT. It gives the limit of 7.7×10^{-47} cm^2 for WIMPs of 35 GeV c^{-2} at 90% confidence level [80].

The upgraded version of XENON1T is XENONnT [114] which is under commissioning at the Italian Gran Sasso Laboratory (LNGS). The total active mass is 5.9 tons of LXe. The design goal is to reach a concentration of 1 Bq/kg and an ER background of 0.05 events/ton/day/keVee.

LUX-ZEPLIN (LZ): The Large Underground Xenon (LUX) is 350 kg in a liquid xenon TPC at the Sanford Underground Research Facility in the Black Hills of South Dakota, USA. LUX started taking data in 2013 [115] and published results from the first exposure set on spin-independent WIMP-nucleon interactions [81]. The next phase, LZ (LUX and ZEPLIN), is proposed to be a 7 t LXe detector. The sensitivity of LZ to Spin-Independent WIMP-nucleon couplings is expected to be 1.5×10^{-48} cm^2 with 90% CL at 40 $GeVc^{-2}$ [107].

DARWIN (DARk matter WImp search with Noble liquid) is a next-generation, multi-ton dark matter project in Europe for the direct detection of dark matter candidates in the form of WIMPs. The goal proposed by DARWIN is to explore the entire accessible WIMP parameter space until the background is dominated by the irreducible coherent neutrino scattering events [84]. The DARWIN detector will be filled with 50 t of liquid xenon, of which 40 tons is the active target. It will be very hard to get such a huge amount of xenon because the production rate of xenon is very slow. Taking this concern into account, DARWIN is planning to make its first run in 2026. It is expected that the spin-independent cross-sections down to 2×10^{-49} cm^2 (90% CL for 40 $GeVc^{-2}$ WIMPs) can be reached in a 200 t × yr exposure[116], equivalent to 5 years.

The ultimate goal of the detector for WIMP sensitivity is to reach down to the neutrino floor, which is an irreducible background, and to study other fields such as double beta decay. 40 tons of active xenon contains 3.6 tons of ^{136}Xe. The projected half-life sensitivity is 2.4×10^{27} years, using a fiducial volume of 5 t of natural xenon and 10 years of operation with a background rate of less than 0.2 events/ (t × yr) in the energy region of interest [117].

PandaX (Particle AND Astrophysics experiment with Xenon) is situated in China Jinping Underground Laboratory (CJPL), the world's deepest lab (1μ/week/m2) [118]. There are two experiments named PANDAX and CDEX dedicated towards the DM searches and one neutrino experiment also running in CJPL. Figure 3.2 shows the schematic layout of the CJPL.

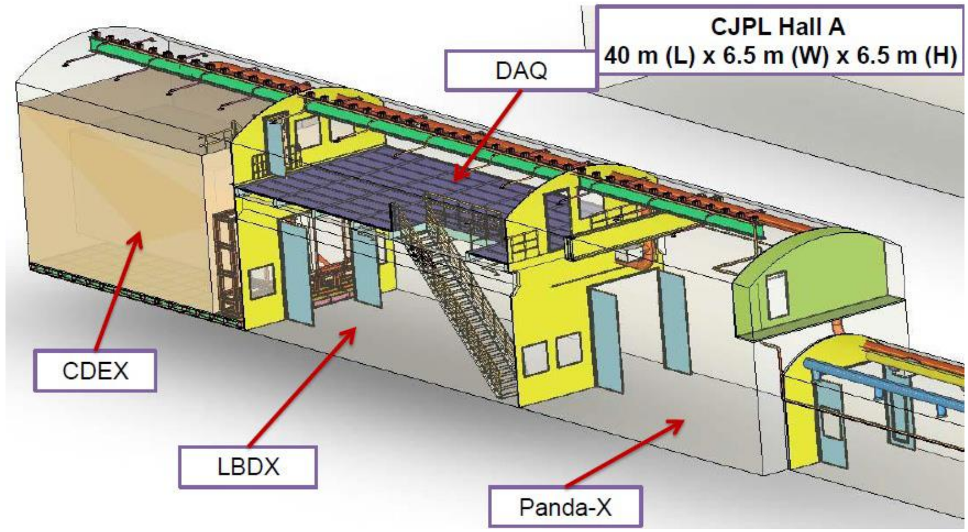

Figure 3.2 Schematic picture of Jinping underground lab. Figure is taken from ref. [118].

The first phase (2009-2014) was PandaX-I [119] which is 120 kg of total mass. The second phase (2014-2018) is PandaX-II [120], a 500 kg detector. There will be another experiment PandaX-III, a gaseous TPC which will search for the neutrinoless double-beta decay of ^{136}Xe [121].

The current project of the PandaX group is a multi-ton large LXe detector named PandaX-4T [122]. The active mass of the detector is 4 tons out of a total mass of xenon of 6 ton. Recently, PandaX-4T has released results for the data with an exposure of 0.63 ton. year. The upper limit is set on the dark matter-nucleon spin-independent interactions, with the lowest excluded value of 3.3×10^{-47} cm^2 at 30 GeV c^{-2} [123]. A further upgrade has been proposed with a 30-t scale PandaX-30T experiment.

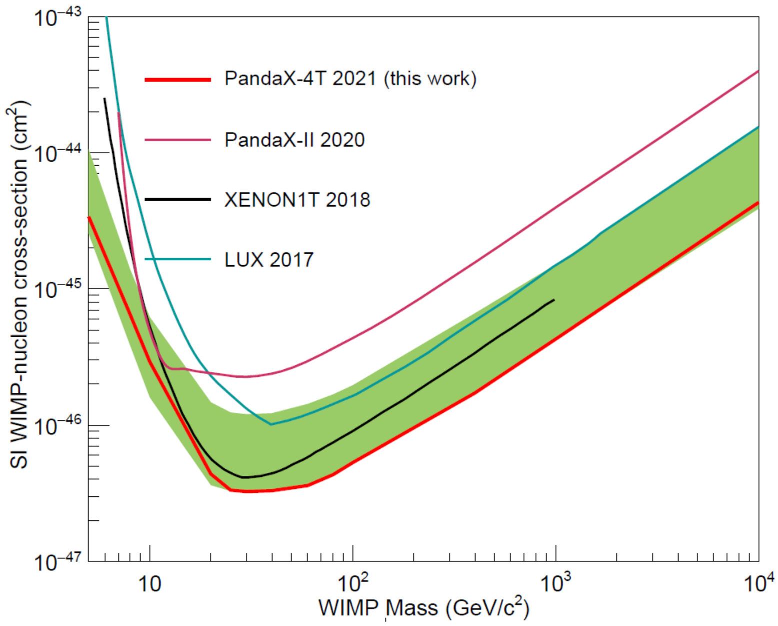

Figure 3.3 The 90% C.L. upper limit vs. DM mass for the SI WIMP-nucleon elastic cross section from PandaX-4T commissioning data (red). The figure is taken from ref. [123]

The DarkSide is a two-phase TPC at LNGS with liquid argon as the target material for the scattering of dark matter particles. The first detector, Darkside-50 (DS-50), contains 50 kg of argon. It gives a limit on the WIMP-nucleon spin-independent cross-section of 6.1×10^{-44} cm^2 at 100 $GeVc^{-2}$ corresponding to a 90% CL. Operating with atmospheric argon, DarkSide-50 provided a powerful assessment of Pulse Shape Discrimination (PSD). It measured a rejection factor better than one part in 1.5×10^7 [124].

DarkSide-50 has observed no background events over a run period over two years [83]. In addition to sensitivity to WIMPs with masses above 30 $GeVc^{-2}$, the two-phase DarkSide-50 detector has extended its reach to WIMP masses below 10 $GeVc^{-2}$ by detecting single ionization electrons (i.e., S2-only). The extremely low background, high stability, and low 100 eV_{ee} (600 eV_{nr}) analysis threshold of DarkSide-50 enabled a study of very-low energy events, which resulted in sensitivity for low-mass DM searches in the mass range 1.8–3.5 $GeVc^{-2}$ [125]
The group of LAr collaborations (ArDM, DarkSide-50, DEAP-3600, and MiniCLEAN) formed Global Argon Dark Matter Collaboration (GADMC) to build a series of future experiments that maximally exploit the advantages of LAr as a detector target.

Table 3.1 Comparison of different detectors and their sensitivity in WIMP cross-section

Experiments	**Detectors**	**Mass**	**Cross-section (cm^2)**	**WIMP mass (GeV/c^2)**
Cryogenic bolometers	SuperCDMS	24 kg	4×10^{-44}	2
	EDELWEISS	20 kg	1×10^{-43}	2
	CRESST	2.5 kg	6×10^{-43}	1
Crystal detector	DAMA/LIBRA	250kg	–	–
	ANAIS-112	112 kg	1.6×10^{-42}	40
	COSINE-100	106 kg	3×10^{-42}	30
Ionization detector	DAMIC	40 g	2×10^{-41}	3-10
	CDEX	10 kg	2×10^{-43}	5
Bubble chambers	PICO-40L	59 kg	5×10^{-42}	25
Noble Liquid Gas detectors	XMASS	857 kg	2.2×10^{-44}	60
	XENON1T	3.2 ton	7.7×10^{-47}	35
	PANDAX	4 ton	3.3×10^{-47}	30
	LUX/ZEPLIN	7 ton	1.5×10^{-48}	40
	DarkSide	50 kg	6.1×10^{-44}	100
	Darwin	50 ton	2×10^{-49}	40

4 Detector medium

4.1 Media: LNe, LAr, LXe

Liquid Noble gases have their particular unique properties [126-128], which make them suitable as a detector medium in different kinds of detectors [129]. Liquid noble gases are used for measuring two phenomena: Scintillation, which is the result of the collision of DM particles with the detector medium, and the other one is ionization, which leads to free electrons. Free electrons can either recombine by producing additional scintillation light or escaping and drifting in an electric field to produce secondary scintillation for a charge measurement. For this purpose, there are mainly three liquid noble gases used: Liquid Xenon (LXe), liquid Argon (LAr), and liquid Neon (LNe).

These above-mentioned noble gases have unique advantages but with some limitations. LXe has an advantage over the other two as it has a higher atomic number and density and a higher WIMP-nucleus interaction cross-section. In addition, it is a self-shielding medium, so that it has excellent background rejection power. However, the natural abundance of Xe is very low, around 10^{-5} of Ar. Xenon is won from the atmosphere as a byproduct of LN2 for the steel industry. However, since there were very few big applications, few companies actually refined it to be commercialized. The yearly worldwide production is around 50 tons. On the other hand, Argon is used in very bulk quantities for welding. The natural abundance is about 9×10^{-3}. Therefore even large quantities are readily available, and the cost is relatively low.

Furthermore, the discrimination of NR and ER signals is easily possible in LAr due to a large difference between the decay times of the S1 and S2. However, argon needs special care in terms of background reduction as it contains the radioisotope ^{39}Ar, mostly from earlier atomic tests in the atmosphere. The activity is about 1Bq/kg, which needs to be removed. In addition, LAr needs wavelength shifters to observe the scintillation light at 128 nm, while photomultipliers are used in LXe (175 nm). The wavelength is too short to pass through the window material. We can use the MgF2 window, but they are tough to make. Whereas, 175 nm of Xe light passes through synthetic quartz. This material is also not the easiest to seal, but the technology is reasonably understood and not very expensive.

The other choice of medium is Neon which is better for the coherent scattering neutrino (CNS) experiments as the nuclear recoil energy is inversely proportional to the atomic number. In addition, neon has a lower atomic number than LXe and LAr. Therefore, it helps to obtain a low energy threshold in the DM experiments.

LXe is used by XMASS, XENON, PANDAX, and LUX/ZEPLIN. LAr is a detector medium in DARKSIDE and DEAP, whereas LNe +LAr is used by MiniCLEAN [130].

For better sensitivity, one should need a higher scattering cross-section of DMs. The scattering cross-section is proportional to the neutron number's square, indicating a higher scattering rate. The neutron number of Xe is high, so LXe has an advantage over the other two noble gases.

If the energy of the neutrino source is more than 30 MeV, the maximum recoil energy is above 15 keV in xenon [131]. The scattering rate is nearly 0.1 events per year per kg of xenon and lower for the other two. The scattering rate is too low in the liquid noble gas detectors; hence, they need large detector masses for DM search. As the form factor of the LXe drops to zero for recoil energy 100 keV and 0.5 in the case of Ar.

Table 4.1 Comparison of Noble gases

Noble gas	**At. No./ At. Mass**	**Liquid density (ρ/cm^3)**	**Boiling point at 1 bar (K)**	**Energy loss (dE/dx) MeV/cm**	**Radiation length (cm)**	**Scintillation wavelength (nm)**	**Cost**	**Fraction on earth (ppm)**
Neon	10/20	1.2	27	1.4	24	77	$$	18.2
Argon	18/40	1.4	87	2.1	14	128	$	9340
Xenon	54/131	3.0	163	3.8	2.8	178	$$$$	0.09

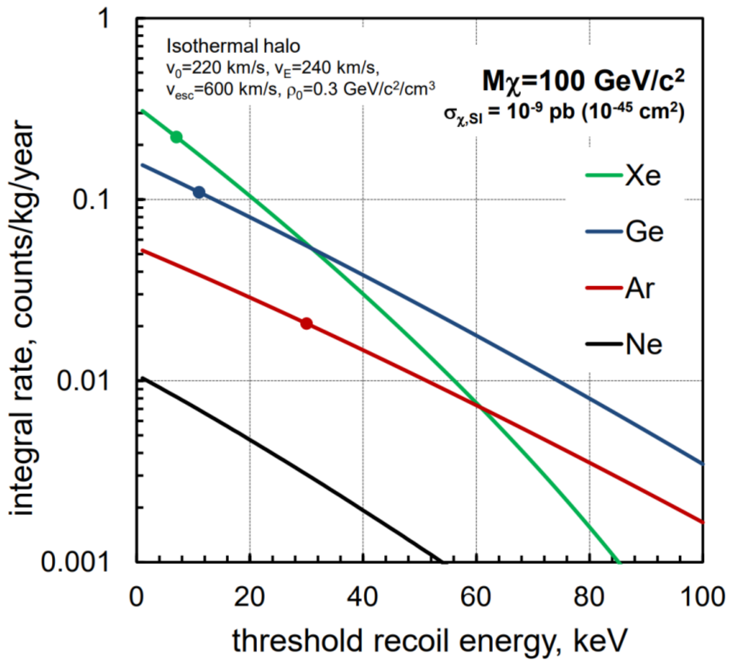

Figure 4.1 Comparison of event rate between the target materials. Figure is taken from ref. [128].

4.2 Liquid Xenon as a detector medium

Table 4.1 shows that LXe is the most expensive noble gas, but due to its large atomic mass, number, density, and scintillation wavelength, it is considered for many noble gas detectors. The event rate is higher in LXe due to its lower energy threshold. The event rates are expressed in terms of counts/kg/keV/day. Figure 4.1 shows that this rate is too low, e.g., for the 100 kg of xenon detector and 100 GeV DM mass with cross-section ~10^{-45} cm^2. Therefore, the detector throughout the year can capture only 1 event. Xenon is the most sensitive due to its higher nucleus mass. All the properties of xenon are as follows:

4.2.1 Properties of Xenon:

1. **Large atomic mass:** The atomic number of xenon is 131, higher than other detector mediums. Xenon is very dense, which means it has a high nuclear charge Z. The absorption of background depends on Z and the density. That implies that it is an excellent shield against radioactivity, in particular gamma rays. Any radioactivity coming from detector construction materials thus tends to get stuck in the outer few centimeters of the detector target.

2. **Stable Isotopes:** Xenon is a favorable choice as a detection medium as it has stable and no long-lived radioisotopes (maximum half-life of ^{127}Xe is 36.3 days). Some of the isotopes of xenon have non-zero nuclear spin, which makes Xe suitable for spin-dependent interactions.

3. **Xenon purification:** Xenon can be purified well from radioactive contaminants. These radioactive elements are the source of the background in the signals (e.g. ^{85}Kr).

4. **Scintillator and ionizer**: LXe has efficient scintillation power rather than other noble gases. This gives a very low energy threshold, which increases the sensitivity of the experiment. The scintillation light in xenon can be captured by photomultipliers, without a need for wavelength-shifters, as is the case of LAr. Additionally, xenon is a good ionizer too.

5. **Shelf shielding capacity:** One of the main features of noble gases is to reduce the surrounding background in the detector due to their stopping power. That is why they are known as self-shielding material. For example, LXe has high stopping power followed by LAr.

The other efficient method to reduce most of the background which comes from outside is fiducialization. It also works for other materials, but it depends on the detector. Moreover, it is expensive. There is a lot of mass in the outer layers of a detector.

The additional shielding material, such as the lead/poly or water shields, is used for background reduction. We have to watch out not to introduce more radioactivity when we take out these materials. This is the reason to use 'ancient lead' from ships transporting lead in ancient times, 2000 years ago and, water with low radon concentration, etc. Radon comes from the natural activity of rocks. We have to remove the Rn and then keep it in a clean environment. There is also recycled steel from old battleships sunk during World War II, i.e., before Hiroshima and Nagasaki and the nuclear tests in the atmosphere, which can be used in scientific experiments.

One of the methods should be to use LXe and LAr, both detectors in the same shield. Then, if the DM signature appears in both detectors, we can be sure about the existence of DM signals. The idea once proposed by C. Rubia stated that:

"*The present WIMP search strategy is not sufficient. If we drive the cross-section more and more down, at some point, we must detect a signal from some* *unexpected rare background. We were lucky since we did not see anything. But if we one day observe a signal, what do we do? We cannot claim discovery since we do not know what the signal is. We need more information*."

Therefore, he was proposing a 10-ton LXe and a 10-ton LAr in the same shield. If we see the signal in both detectors with the right ratio (A-dependence), we can be surer that we observed DM. On the other hand, if the ratio is wrong, or we see the signal in only one detector, it is not WIMPs but something else.

Table 4.2 Physical properties of xenon

<table>
<tr><th>Sn</th><th colspan="2">Properties</th><th colspan="3">Value</th></tr>
<tr><td>1</td><td colspan="2">Atomic number</td><td colspan="3">54</td></tr>
<tr><td>2</td><td colspan="2">Molar mass</td><td colspan="3">131.29</td></tr>
<tr><td rowspan="3">3</td><td colspan="2" rowspan="3">Isotopic abundances</td><td>^{124}Xe (0.095%)</td><td>^{126}Xe (0.089%)</td><td>^{128}Xe (1.91%)</td></tr>
<tr><td>^{129}Xe (26.4%)</td><td>^{130}Xe (4.07%)</td><td>^{131}Xe (21.2%)</td></tr>
<tr><td>^{132}Xe (26.9%),</td><td>^{134}Xe (10.4%),</td><td>^{136}Xe (8.86%)</td></tr>
<tr><td rowspan="2">4</td><td rowspan="2">Density</td><td>Gas (273 K, 1 atm)</td><td colspan="3">5.8971 g L^{-1}</td></tr>
<tr><td>Liquid (165.05 K, 1 atm)</td><td colspan="3">3.057 g cm^{-3}</td></tr>
<tr><td>5</td><td colspan="2">Melting point</td><td colspan="3">161.4K</td></tr>
<tr><td>6</td><td colspan="2">Boiling point</td><td colspan="3">165.05K</td></tr>
<tr><td>7</td><td colspan="2">Triple point</td><td colspan="3">161.31K, 0.805 atm, 3.057 g cm^{-3}</td></tr>
<tr><td>8</td><td colspan="2">Critical point</td><td colspan="3">289.74K, 57.65 atm, 1.155 g cm^{-3}</td></tr>
<tr><td>9</td><td colspan="2">Latent heat of fusion</td><td colspan="3">17.29 kJ kg^{-1}</td></tr>
<tr><td rowspan="2">10</td><td rowspan="2">Heat conductivity</td><td>Gas, 273 K, 1 atm</td><td colspan="3">5.192mWm^{-1} K^{-1}</td></tr>
<tr><td>Liquid, 178 K</td><td colspan="3">71.1mWm^{-1} K</td></tr>
<tr><td rowspan="2">11</td><td rowspan="2">Relative permittivity</td><td>Gaseous Xe</td><td colspan="3">1</td></tr>
<tr><td>Liquid Xe</td><td colspan="3">2</td></tr>
</table>

4.3 Time projection chamber

The time projection chamber (TPC) can provide 3-dimensional track information (x-, y-, and z-coordinates) of the ionization deposited in a gas or liquid volume. Additionally, it is helpful for particle identification by measuring the ionization loss in a magnetic field.

In the late 60s, the multi-wire proportional chamber (MWPC) and drift chamber were introduced for better data tracking. These detector technologies' continuous development helped construct a detector with complex designs for semiconductor electronics for fast readouts. Later in 1976, the TPC was introduced by D.R. Nygren, where MWPC used to readout. Generally, the TPC consists of a gas-filled sensitive volume with a central cathode and the MWPC system with anode on both sides of the TPC.

Figure 4.2 shows the working principle of the TPC. When a charged particle passes through the gas volume of the TPC, it ionizes the gas atoms along its trajectory (point 1). Due to a high field applied between the endplates of the TPC, the released electrons drift in this field towards the anode (point 2). At the anode plane, the electrons can be detected on the readout plane, segmented in the directions perpendicular to the drift direction (point 3).

Many TPCs have been constructed. The first TPC was used for the UA1 experiment in CERN in 1981. Then TPC was also a part of the PEP4 experiment in 1983 at SLAC. Although the use of TPC detectors was proposed earlier, it was delayed because of the availability of high-speed digitizers (FADCs) for thousands of channels and readouts.

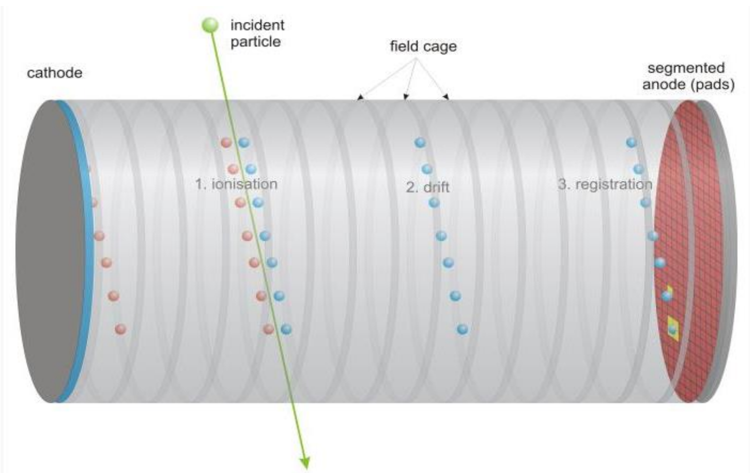

Figure 4.2 Working principle of a TPC. Figure is taken from ref. [132]

Some TPCs have been used in several fixed-target experiments, such as NA35, NA36, and NA49 at CERN. In addition, a TPC is operating for STAR in Brookhaven and ALICE at LHC. Other categories of TPCs are liquid argon and xenon TPCs. Nowadays; nearly all experiments use a TPC with few exceptions, such as XMASS. Even Liquid Xenon Gamma-Ray Imaging Telescope (LXeGRIT) was liquid xenon TPC operating on high altitude balloons.

4.4 Ionization and Scintillation Process in liquid Xenon

When γ-ray or alpha particles interact with the detector medium, the deposited energy in liquid noble gas is transferred to excited atoms, ion-electron pairs, and free electrons. This process can be summarized in an energy conservation equation, firstly proposed by Platzman [133].

$$E_0 = N_i E_i + N_{ex} \times E_{ex} + N_i \epsilon,$$

Where E_0 is the deposited energy in a liquid medium, E_i is the average energy required to produce N_i electron-ion pairs and N_{ex} is the number of excited atoms at the energy level of E_{ex}. ϵ is the average kinetic energy of free electrons.

W-value is defined as the average energy required forming one electron-ion pair in the medium:

$$W = E_0/N_i.$$

The W-value is equal to 15.6 eV in liquid xenon. A medium with a smaller W-value implies that ionization is more efficient than the larger W. Compared with gas xenon, argon, and krypton, liquid xenon has the smallest W-value and, therefore, the largest ionization yield. Except for the low energy region, the W-value has a weak correlation with deposited energy and is considered constant. Deposited energy thus can be estimated by measuring the number of ion-electron pairs. Since the low energy region is particularly interesting for DM search, several experiments [134, 135] were recently conducted to measure the relative ionization yield of low energy radiation.

Scintillation in liquid xenon is due to ultraviolet photons emitted in the de-excitation of an excited atom to the ground state. Both excited xenon atom and ionized xenon atom can break into the excited molecular state (Xe_2^*)called an excited dimer, or excimer for short. For excited atoms, the formation of excimers is attributed to the interaction with the surrounding atoms:

$$Xe^* + Xe + Xe \rightarrow Xe_2^* + Xe$$

Ionized atom form excimer in the process of:

$$Xe^+ + Xe \rightarrow Xe_2^+$$
$$Xe_2^+ + e^- \rightarrow Xe^{**} + Xe$$
$$Xe^{**} \rightarrow Xe^* + heat$$

$$Xe^* + Xe + Xe \rightarrow Xe_2^* + Xe$$

The de-excitation is accompanied by the emission of a photon with the wavelength centered at 178nm. This process is expressed as

$$Xe_2^* \rightarrow 2Xe + h\nu$$

4.5 Dark matter dual-phase detectors

4.5.1 Principle of Dual-Phase method

Being an efficient detector medium, a sample interaction in the active LXe volume produces scintillation photons and free drifting electrons. The direct light (S1) is then detected by two PMT arrays: below the cathode and above the anode in the gas phase. The charges drift in the applied electric field and are extracted from the liquid. They produce proportional scintillation (S2) in the strong homogeneous field above the liquid level, which is also seen by the two PMT arrays. The side walls are usually made reflective with Teflon or poly-tetra-fluoro-ethylene (PTFE) to detect as many photons as possible in the two PMT arrays.

PTFE is a very efficient reflector for the xenon light at 178 nm. Its use as a reflector saves many PMT to observe the light on the side walls. However, with the rather long length of large area PMTs, it would require a large volume outside the active volume beyond the field shaping of the field cage. An additional problem is then the construction of the field cage. It requires an excellent insulator to support the narrowly spaced field-shaping electrodes. However, at the same time, it must be transparent to detect the scintillation light. Also, the front face of the PMTs is at the cathode potential of the PMTs, far below the electric potential of the shaping electrodes. Thus early on, the use of PTFE as a structural component of the field cage was developed [136] and is now applied in all LXe TPCs. PTFE is a good insulator, and it is well-matched in the dielectric constant with LXe. Thus it can replace the liquid even in strong electric fields without disturbing the field distributions.

The schematic diagram of the dual-phase principle is shown in Figure 4.3 (left).

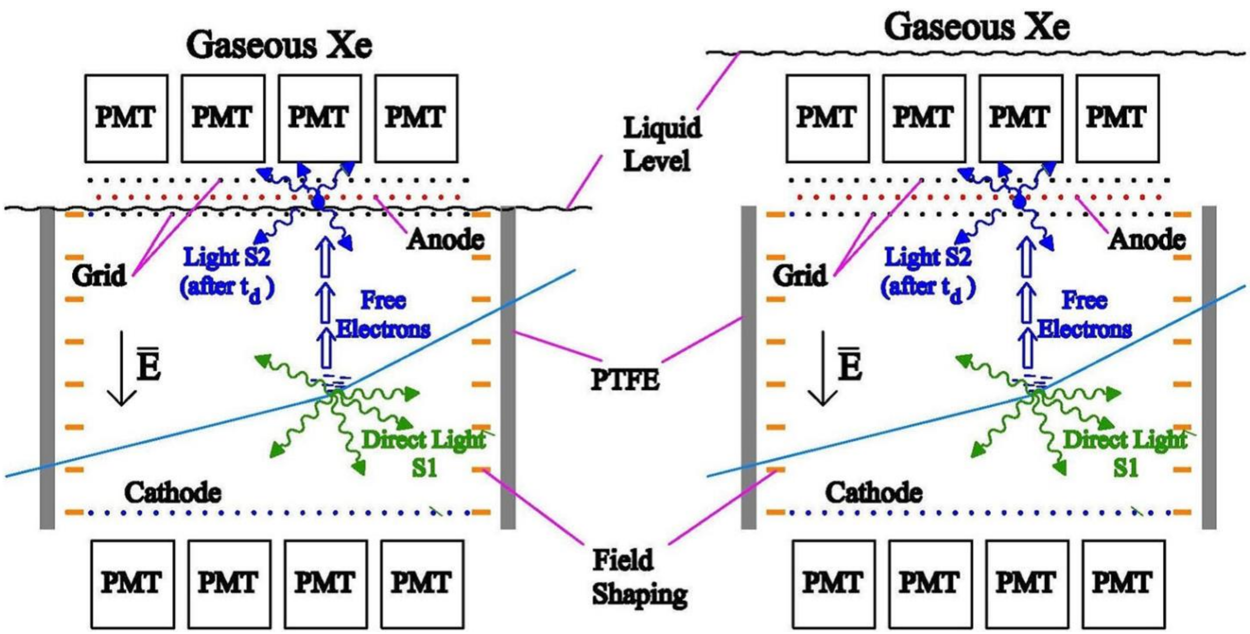

Figure 4.3 Schematic working principle of a DP (left) and an SP (right) LXe detector. The differences are mainly in the position of the liquid level and the diameter of the anode wires. Figure is taken from ref. [6].

A DP detector measures both S1 and S2. Separately both quantities measure the amount of energy deposited by the event. Combined, both measurements can improve the energy resolution far beyond what would be expected from the two measurements separately. This takes advantage of a known anti-correlation [137] between charge and light. Moreover, this can also help to reduce background events.

The DP method is an elegant way to address the lack of adequate charge-sensitive amplifiers. Moreover, this technique is so sensitive that even a single drifting electron can be detected [138]. Practically, however, this simple principle also imposes stringent limitations on detector design.

Thus, the DP method is presently the favored technique for LXe DM detectors. It has been quite successful until now, but it is not without challenges.

4.5.2 Limitations of Dual-phase:

1. Liquid level control: The active volume must include the liquid level. S2 depends on the path length between the liquid level and the anode. Therefore, the anode must be perfectly parallel to the liquid level. Any deviation will make the S2 position-dependent. To compensate for slight deviation from the design and inaccuracies in the mounting of the detector, it is necessary to level it once the liquid is filled. This means all connections to the outside world must be flexible. Three precise level meters around the perimeter of the anode are required to facilitate this procedure. The fine-tuning can then be performed in a lengthy procedure with actual data.

However, the liquid level also depends on the run parameters, e.g., temperature and pressure, as well as recirculation speed. Thus the gap between the anode and liquid level must be controllable. This can be achieved utilizing a mechanically adjustable 'overflow' device. However, the detailed implementation of these functions becomes a challenge when the diameter of the anode goes beyond 1 m, and the mass of the detector is more than a few hundred kilograms.

2. Extraction efficiency: The anode potential controls two different processes, the extraction from the liquid and the gain of the proportional scintillation in the gas gap. The potential must be sufficient to assure good extraction efficiency, but high fields result in a very large gain and the potential formation of electron avalanches or saturation of the readout electronics. Additionally, a very high anode potential might lead to instabilities and spurious HV discharges.
The best choice for the anode potential involves a compromise. For these operating conditions, the PMTs must detect everything from the weak direct scintillation light at low energies to the intense proportional light at high energies. Thus, the dynamic range of the readout will eventually define the effective energy range of the measurements. Fortunately, there is a combination of design parameters that yield adequate performance.

The detectors are normally designed for 100 % extraction efficiency. However, during a long-run period, spurious discharges might occur. In such instances, it is common practice to reduce the anode HV for better HV stability, even if this means reduced extraction efficiency. Practically, efficiencies as low as 50 % are reported in the literature [139].

3. Pulse formation: The gas gap between the liquid and the anode is typically kept at 3–5 mm, and the anode potential is around 5 kV. The anode must be transparent to the scintillation light, and stretched wires or meshes are used to achieve this. The wires must not sag under the influence of gravity or the electric field within the required precision. Meshes are considered simpler, but the manufacturing by etching or electroforming does not produce round conductor cross-sections. At the sharp corners of the conductors, the 1/r field is much higher than that in the parallel gap. This might lead to local avalanche formation. Localized avalanche formation in a fraction of the events may reduce the energy resolution, especially at high energies where statistical fluctuations in the number of S1 photons are small. Evidence can be observed in the pulse shapes of the charge signals (Figure 4.4). The observed initial signals from the PMTs are very fast pulses of the direct light at $t = t_0$. The subsequent pulses are from the proportional light. With the known drift velocity, the arrival time relative to t_0 is a measure of the z-coordinate of the interaction. There is one S1 in an event, but there can be more than one S2 pulse, e.g., when a gamma-ray interacts via Compton scattering.

As mentioned earlier, we observe two event types, NR for WIMP candidates and ER for gamma-ray backgrounds. The light from both types has the same wavelength, but the decay time and the fraction of charge to light (S2/S1) are different. The details of the signal formation have been discussed in a study [138]. Practically, the discriminator against ER events is the ratio S2/S1. The S1 pulse shape is determined by the original light pulse and pulse shaping by the cable connections. It is a very fast and prompt signal. The S2 pulses are produced while the electrons cross the gap between the liquid level and the anode. Therefore, the S2 pulse shape should be a 1 ms wide flat-top pulse. With the usual 10 ns binning, the statistical fluctuation in each bin is large, and it is difficult to detect any structure within the recorded pulse.

The first event in Figure 4.4 shows a single scatter event with the fast S1 signal and a S2 signal about 1 ms wide delayed by the drift time reflecting the z coordinate. However, the S2 pulse does not really look like a flat top. It has a strong enhancement at the end. This is observed in many but not all S2 pulses. The enhancement is produced when the electron has nearly passed the entire gas gap to the anode. At the very end of the path, the drifting electron cloud sees the stronger 1/r field in one of the edges of the conductor. This results in a higher proportional gain and possibly in the formation of electron avalanches.

The second event in Figure 4.4 is probably a γ- ray Compton scattering before being absorbed. Again, there are two S2 signals, one for each interaction point. The distance between the two pulses gives the difference in z-coordinates. As discussed before, the first S2 pulse shows the enhancement, but the second does not.

However, the edges of the second S2 pulse are rounded off at the beginning and the end. This might be the superposition of two pulses with a timing difference of maybe 100 ns, i.e., a second Compton scattering. This also would explain the small step in the falling flank of the pulse. If correct, the additional scattering would have a small scattering angle, i.e., few deposited energy. Therefore, the distance in the z coordinate would be small, less than 0.5 mm. However, of course, we do not have any information about the distance in x - y. Practically this means that two events separated in z by less than a mm cannot be resolved because of the 1 ms width of the pulses. This, of course, compromises the detection of double events, which is used to discriminate against ER background.

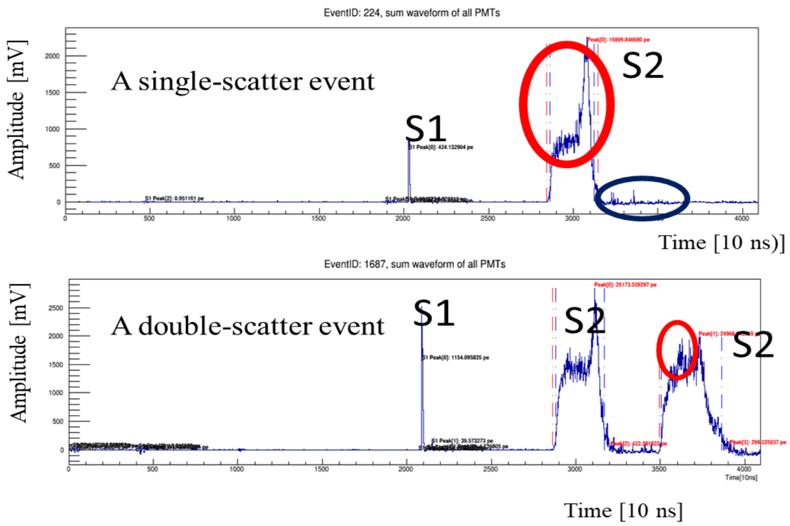

Figure 4.4 Distortion in S2 pulses in single and double scatter events. Figure is taken from ref. [140].

4. **High voltage:** In DP detectors, the anode and its HV connection are in the gas phase. Any disturbance in the field of order 10 kV/cm in the gas can lead to spurious discharges. Such disturbances can be caused by less than perfectly stretched wires on the anode, waves on the liquid level, or sharp points on the HV connection or anode frame. For long-run periods, the anode HV is kept below the optimal value to avoid breakdowns, but this implies reduced extraction efficiency.

4.5.3 Other challenges:

There are some other limitations and handling issues with dual-phase TPC.

1. Difficult to stretch wires or meshes for very large detectors.

2. Difficult to find meshes above 1 m.

3. Meshes of large-size dual-phase detectors not commercially available.

4. Field lines might pass through the meshes and return to the anode

5. Waves and ripples on Liquid Level because of continuous recirculation.

6. In DP no liquid between the liquid level and PMTs so no self-shielding and causes high background.

All these conditions become challenging when the diameter of the anode grows beyond 1 m, and the mass is in the order of several tons. Determining the operating conditions in a DP detector is not an easy task. The number of proportional scintillation photons depends on several parameters, which cannot be chosen freely. Other considerations, like the stability of operation and mechanical tolerances, also enter the optimization process. For example, the anode potential has to be of order 5 kV to extract the electrons into the gas phase efficiently, but such high voltages enhance the probability of spurious breakdowns at any imperfection of the structure, including the connection in the gas. Thus, the voltage is a compromise between the extraction efficiency and stability of operation.

The distance between the anode and the grid wires, typically 5 mm, is another example. This gap is cut in half by the liquid level, and the field above the liquid level is supposedly homogeneous. However, the gap cannot be made significantly smaller because of the mechanical tolerances in a large detector with a diameter of more than 1 m. Furthermore, any deviation due to sagging wires or imperfections in leveling will have a large local effect on the S2 signal. Any gap width significantly larger would require an excessive anode voltage.

In a DP detector, the S2 gain is of order 200–300 photons/electron (Ph/e-). Such a high gain can easily cause the readout to saturate. The S1 light is produced deep inside the active volume, and any given PMT will normally only see a few photons. This is not so for the strong S2 light, as it is produced at the edge of the active volume, and many photons will hit the same PMT.

That is why we need to think about an alternative of the dual-phase to overcome these limitations. On the other hand, the single-phase technique can solve the problems listed above and promises better performance for DM search with very large mass detectors.

5 Detector Development program at SJTU

Charge read out with electro-luminescence in liquid xenon is not a new idea and was tested and established by the Waseda group in Japan 40 years ago. Liquid xenon at that time was a rather young detector medium, not yet well explored, but with very interesting characteristics. Among them was an expected energy resolution predicted to be similar to High-purity germanium (HPGe). It could easily be achieved in gaseous Xe detectors up to 50 bar but was never realized in liquid detectors. Over all the years with many different studies the energy resolution of liquid xenon did not improve. Only in 2003, it was proven that there is an anti-correlation between charge and light signals [137]. The resolution is much better on the weighted sum of the two signals, although not as good as Ge.

This early experiment was successfully concluded, but this approach had not been carried forward. The energy resolution did not improve. The technological challenges at that time were simply too large to replace the standard read out with charge-sensitive amplifiers (CSA) in a typical ionization chamber setup.

The Waseda group [3, 4] in 1979 used the comparatively high energy electrons (1 MeV) from 207Bi. The high electric field strengths required for electroluminescence (EL) occur in the 1/r field around thin wires. The group even proved that the charge measured with electro-luminescence provides the same energy resolution as a CSA. The value they reached was inferior to other ionization chambers, indicating that they still had issues of liquid purity among many other problems. Thus, there was no logical reason to use electro-luminescence. The published results were almost forgotten with passing time.

Finally, there were other experiments with electro-luminescence to achieve charge multiplication in liquid xenon. Contrary to LAr, this is possible, but according to tests by Derenzo et al. [141], it requires very thin wires (< 4 um) to reach a sufficient strength of the 1/r field. This was the final verdict on proportional scintillation in liquid xenon since everybody dreaded using delicate structures with such thin wires. And they also would not give a 'good' energy resolution, but added the fluctuations from the avalanche formation. Instead, the dual-phase (DP) approach was accepted by the experimentalists despite having many challenges.

Here, the single-phase (SP) detector is different from the scintillator detectors where the detector medium is liquid and only measures light. Therefore, here, “SP detector” means the detector which measures light as well as charge or proportional scintillation in the liquid state.

5.1 Background of the idea

The LXe Time Projection Chamber (TPC) at present is the detector of choice for the search of DMs in the form of WIMPs at high masses around 50 $GeVc^{-2}$ and above. It is a powerful instrument, but not without challenges. The detected energies are very small (<50 keVee), i.e. all events are point-like and any structure of the interaction is below the spatial resolution. New detectors are being used deep underground for direct detection of DMs, where they look for rare NR recoils. These DM searches take advantage of the intrinsic properties of LXe. With an expected rate of less than one interaction/kg/day, sufficiently large and efficient detectors are required for DM detection. The target mass for such detectors has increased from the initial 5–10 kg about 15 years ago to the current range of 5–10 tons. As we already discussed, the nuclear recoil of WIMPs can be detected by scintillation light or from liberated charges when an electric field is applied. For comprehensive reviews of LXe detectors, see also[142].

The simplest design principle for LXe DM detectors uses large, single-volume scintillators like the XMASS experiment [77]. However, the deposited energy is rather low (1–50 keVee), and the measured energy and location do not provide much information about background rejection from X-rays and gamma-rays. More information becomes available when the interactions are also registered by additional observables, e.g., by their liberated charge. WIMPs interact with the Xe nucleus producing recoil (NR). Nearly all the background events are ER events. The two event types can be distinguished by the ratio of the charge and light signal (S2/S1). A cut at an appropriate value can suppress the ER background by a factor of nearly 100 [112].

The amount of energy is so small that charge readout with a CSA is impossible [128]. The charges to be measured are much smaller than 0.1 fC, and the capacitance of large anodes is of order many nF. The noise level of even the best amplifiers is far above the signal level. For detection of such low charge signals in liquid detectors, Dolgoshein [2] developed the ‘Dual Phase’ (DP) method. The ionization electrons are extracted from the liquid and generate proportional scintillation in a strong homogeneous electric field in the gas above the liquid. The weak light signal can be detected via noiseless amplification in a photomultiplier tube (PMT). Except for the XMASS experiment, all large LXe DM detectors currently use this principle. However, the DP principle introduces severe restrictions on the geometry and the operating point of detectors. Limitations arise due to obvious conditions such as the liquid level being within the sensitive volume, and the anode being parallel to the liquid level. These conditions become challenging when the diameter of the anode grows beyond 1 m, and the mass is in the order of several tons.

More than 30 years later, the charge measurement in LXe was again investigated by two independent studies, one from Shanghai Jiao Tong University (SJTU) [6] and another one from Columbia Astrophysics Lab (CAL) [5]**.** The results from these two studies are in agreement with the Waseda results. These two new studies open the door for the large single-phase TPC with measurement of electro-luminescence in the LXe but, any such discussion is limited by the fact that the CAL results have two severe drawbacks that are incompatible with high-resolution measurements. These are the shadowing of the light by the anode wires, and a dependence of the pulse shape on the drift path of the electrons in the anode region. There are some erroneous interpretations of the results stemming from an unfavorable geometry of the anode region in the CAL test detector. These assumed drawbacks are easily solved by using the appropriate type of geometry. A separate study by the SJTU group now was able to reconcile the results and eliminate the apparent discrepancies. This reconciliation was presented at the XeSAT2018 conference at Waseda and published the detailed critical analysis of the results from previous studies [9]. For further analysis, the recent study [8] shows the results of field element modeling of electrodes in a large single phase LXe detector.

After the characteristics of SP detectors seem understood, the next step in the development would be a full-scale test in a large underground detector, where the performance at low energies under realistic background conditions can be verified. This would be crucial for future large DM detectors [84].

We hope that a detailed understanding of the presumed drawbacks of single-phase (SP) detectors might replace DP designs in the future with fewer compromises, easier operation, and improved performance.

5.2 Single-phase detector:

The construction of SP detectors is quite similar to DP detectors, but with the liquid level outside the active volume. The anode structure is again an array of three electrodes, two shielding grids with the anode in the center, but all are immersed in the liquid. The anode is made of stretched wires, normally 20 μm gold-plated tungsten. The arrangement of the electrodes resembles a multi-wire drift chamber, with two shielding grids sandwiching the anode. The event generation, charge drift, and S1 detection are identical to the DP operation. When the electrons approach the shielding grid, they encounter the stronger field [143, 144] of the anode and are guided by the field lines around the wires of the shielding grid. The anode potential causes a strong 1/r field around the thin wires. Close to the wire when the field strength exceeds 400 kV/cm, the electrons produce proportional scintillation. Above 700 kV/cm, electron multiplication would set in. The given threshold values were measured by the CAL group [5] and agree with the findings of the Waseda and SJTU groups. Since avalanches introduce additional statistical fluctuations, the anode potential should be chosen such that this value cannot be reached before the electrons hit the wire surface. Practically, proportional scintillation only occurs very close to the wire, normally less than the radius value above the surface. There are no space charge effects since no positive ions are produced. In addition, there are no avalanches since the S2 photons cannot liberate electrons. The S2 gain is different, since the photons are no longer produced over the long distance between the liquid level and the anode, and the S2 pulse will be less than 100 ns.

5.2.1 Principle of operation:

A Single-phase LXe detector is featured with entire immersion in liquid, including the anode structure. An incident particle, e.g. γ-ray, interacts with the xenon atoms in the active volume, and the deposited energy is consumed to ionize and excite xenon atoms along its track. The de-excitation of excited dimers (Xe_2^*) is attributed to the formation of primary scintillation (S1). Electrons, which are released from ionization and free from recombination with xenon ions, are propelled by a potential gradient of ∼1 kV/cm between cathode and shielding grids and drift towards the anode at the velocity of ∼2 mm/μs. Some of the drifting electrons attach to impurities in the volume while others survive and reach the anode. At the final stage, higher field strength accelerates the electrons. The accelerating electrons excite the xenon atoms in the vicinity and de-excitation of these excimers produces secondary photon emission, named proportional scintillation (S2). Proportional scintillation starts at about 400 kV/cm in the liquid. Note that the accelerating E-field is lower than the threshold of electron avalanches, in which the energy resolution deteriorates. The upper and lower PMT arrays measure the S1 and S2 light in liquid xenon simultaneously. The amplitude of S1 and S2 signals carries the information of the deposited energy from the incoming particle.

5.3 Small detector experimental Setup in SJTU:

The active volume of the detector exists between a cathode and an anode structure. Three stainless steel (SS) shaping rings shape a homogeneous drift field between cathode and anode. The cathode is a grid of stretched wires and the anode structure is a stack of three wire grid planes. All grids are made of 20 µm gold-plated tungsten wire stretched on 1 mm thick ceramic frames. The wire spacing is 3 mm, and the wires are soldered to copper strips deposited on the ceramic frames. The opening in the frames defines the active area to 60 × 60 mm^2, i.e. there are 20 wires per grid. All wires on a frame are electrically connected. The spacing of the wire planes is also 3 mm. The anode is the center one with a ground plane on each side to create a field distribution not unlike in the MWPC.

The drift space is 45 mm long. The HV in the cathode was kept at -2 kV for a field of about 450 V/cm. The drift velocity is ~2 mm/μs. The maximum drift time is therefore 23 μs plus the time for the 3 mm gap between grid and anode, or 25 μs in total [6]. The grid was fully transparent for drifting electrons. The upper grid on the opposite side of the anode closes the field. Both grids are kept on ground, and the anode is powered by an independent positive HV power supply. There are two array of 1” Hamamatsu R8520 square PMT used to view the active volume through the anode and the cathode**.** Each array consists of 4 PMTs.

Some gamma rays interactions occur in the outside active volume which affects the actual S1 signals in the active volume. Like DP detector, to avoid such interaction we used 1 cm thick frames of PTFE. The dielectric constant of PTFE and liquid xenon is very similar, is ~2. Therefore, the homogeneity of the electric field in active volume does not affect by PTFE.

There is negative high voltage on PMTs. The direct light (S1) and secondary scintillation (S2) signals are produced in an active volume. However, the field is irregularly shaped and these events would also contribute to the background. An additional grounded grid in front of the PMTs eliminates the field and thus prohibits electrons or space charges from drifting in this region. The UV-quartz can easily withstand the comparatively low field strength in this region. Also, electrons drifting in this space would be directed towards the PMTs which are positive to the cathode. Additionally, there is a blue LED mounted in between the PMTs with appropriate light diffusers. The LED is used to illuminate the PMTs with a low-intensity light to observe the single photoelectron (SPE) signal. The detector is surrounded by a 6” SS tube as a vessel, and this vessel is enclosed in an evacuated 10" SS tube for thermal vacuum insulation. The inner square structure of the detector is surrounded by liquid xenon. Entering gamma-rays can also Compton scatter in this xenon and lose some of their energy. The width of this dead xenon was 13 mm in the corners and up to 30 mm along the sidewalls of the active volume. The pictorial representation of SJTU setup is shown in the Figure

5.1(a). Figure 5.1(b) represents the CAL setup which will discuss in later part of the chapter.

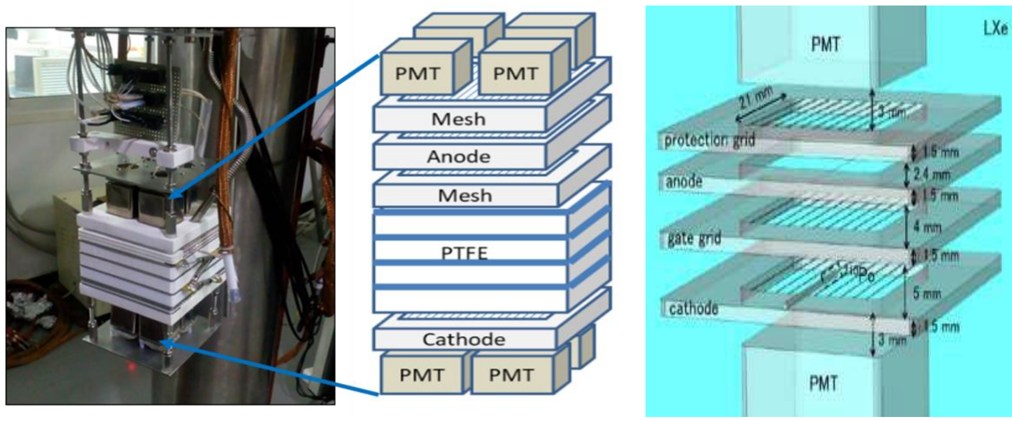

(a) (b)

Figure 5.1a) Picture and pictorial representation of SJTU and b) CAL's setups ref. [5].

5.3.1 Single photoelectron (SPE) calibration:

For a given amount of photons hitting the photocathode the observed signal at the anode depends on two parameters, the quantum efficiency (QE) and the gain of the PMT. The gain depends on the operating voltage whereas the QE is a characteristic of the chosen PMT. In an array of many PMTs a light signal is the sum of the PMT responses, but to measure the amount of light with good resolution the gain of each PMT has to be set such that on average each PMT provides the same anode signal although the QE of the PMTs are all different. Before measuring the light intensity with a PMT array they have to be calibrated to have all the same response. A constant light source equally illuminating the full detector volume is needed.

In most scintillator detectors gamma-ray interactions are used as a source of constant light output. In a large DM detector, this is not possible since the gamma rays would not illuminate the full detector. Thus, the number of photons impinging on the PMT is not known. The only way to achieve a known number of photons is to use a very weak source of light, e.g. from a pulsed LED. The number of photons per PMT must be less than one on average. Then the number of photons on the PMT will follow a Poisson distribution. Most of the time there will be no photon, sometimes one, and two or more will be rare. The distribution of signals will show a narrow pedestal at zero photons and an enhancement for single photoelectron generation above a broad falling distribution of background events (see Figure

5.2). Thus we created a structure with a known number of photoelectrons in the distribution.

Single photo electron calibration is to measure the gain of a PMT at a certain working voltage. Principally, a single photon produces at most one SPE, which is then amplified by a known amount and the measured charge corresponds to 1 PE. The PMT gain can be expressed as

$$\frac{\left(\frac{Q_c}{e}\right)}{N_{PE}}$$

Where Qc is collected at the cathode, e is electron charge and N_{PE} is the number of photoelectrons that can be found with the known PMT gain. The gain of a PMT is adjustable by regulating its working voltage.
Both LED driver and digitizer are synchronously triggered by ~1 kHz test pulse. The output of the LED driver is adjusted to intensity that a PMT in average gets less than one photon per pulse, in practice about 10%, to suppress the double photo electron light.

The energy spectrum of all events is called the SPE spectrum, as shown in Figure 5.2. The SPE peak locates at 3.5×10^5 while the pedestal is at 1.9×10^4, induced by fluctuations of baseline, noise pulses, and electromagnetic interference from the LED driver. The SPE peak position indicates the average gain of PMTs, so the gain value can be derived from the subtraction of SPE and pedestal. The bump ranging from 6×10^5 to 1×10^6 originates from double photoelectrons.

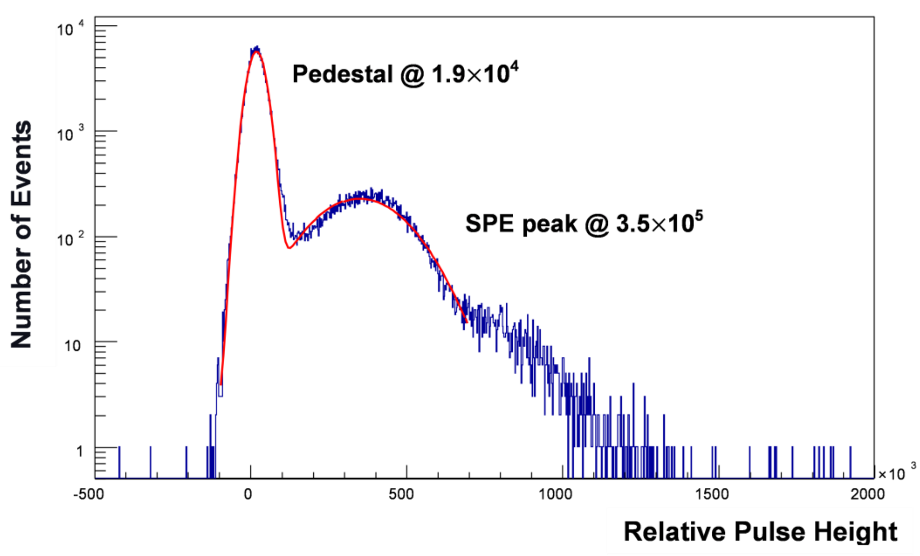

Figure 5.2 SPE spectrum of R8520 (1-inch PMT) at the voltage of -722 V. The gain is 3.3×10^5.

5.3.2 S2 and energy resolution

The proportional scintillation is measured with 3800PE at the +2kV anode voltage. The S2 signals can be seen in the plot S2 vs S1 in Figure 5.3. The lifetime of the electron during the purification is equal to 110 μsec for a maximum electron drift time of 26μsec.

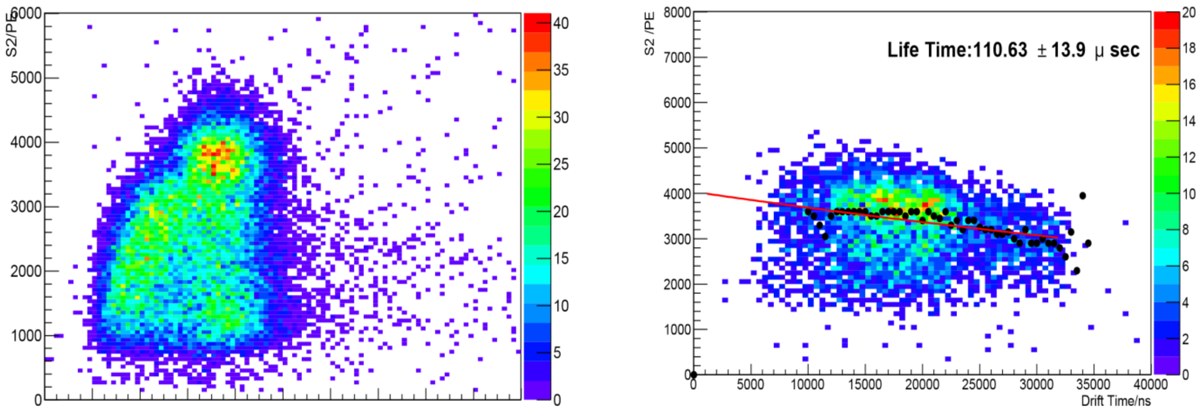

Figure 5.3 Left, S2 vs S1 plot from ref. [6]. The 662 Kev full energy peak is located at the red spot in the plot; right, S2 pulse height of full energy peak vs drift time. An exponential decay fit presents a lifetime of 110 μ sec. The dark spots represent the median of S2 for each drift time bin.

The energy resolution of S1, S2, and combined (S1+S2) induced for 662 KeV gamma rays are 12.8%, 10.4%, and 9.7 %, respectively. This indicates that the energy resolution improves by using a combined energy scale in the system. See Figure 5.4.

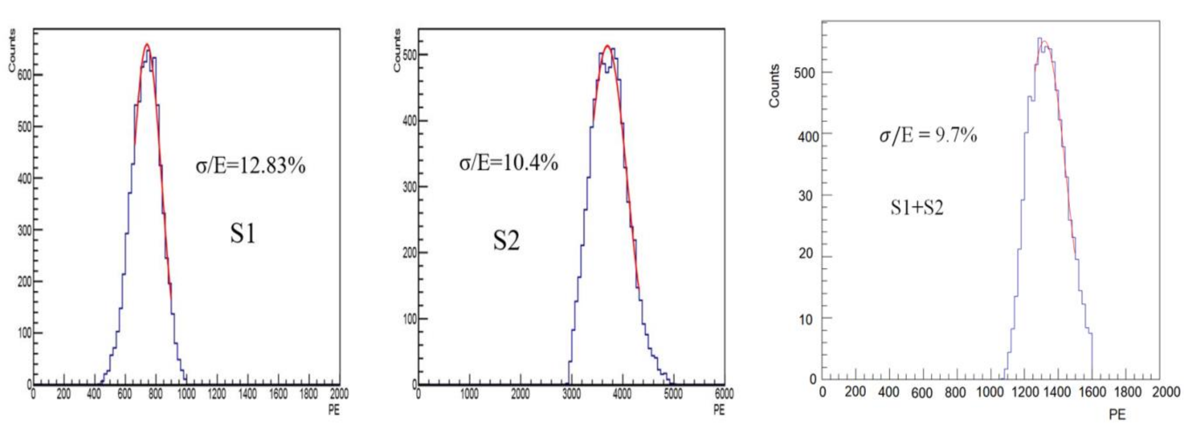

Figure 5.4 662 keV full energy peak in S1, S2, and combined energy spectrum with energy resolution 12.83%, 10.4%, and 9.7% respectively. Figures are taken from ref. [6].

5.4 Geometrical configuration for anode wires at SJTU and comparison with CAL setup:

The geometries were quite similar for SJTU and CAL detectors except for the anode wire configuration. CAL employed a single anode wire located in between the position of the adjacent grid wires (Figure 5.1.b), whereas SJTU had a wire grid as the anode, aligned with the grid wires. The two-wire arrangements are schematically presented in Figure 5.5. All our simulations assume anode electrodes of stretched gold-plated Tungsten wires, a standard element of MWPC. The wire diameter is 20 µm, and the spacing between wires and between wire planes is 3 mm. They are solely used for field shaping and not to achieve position independent detection like the well-known Frisch[145] grids in gridded ionization chambers.

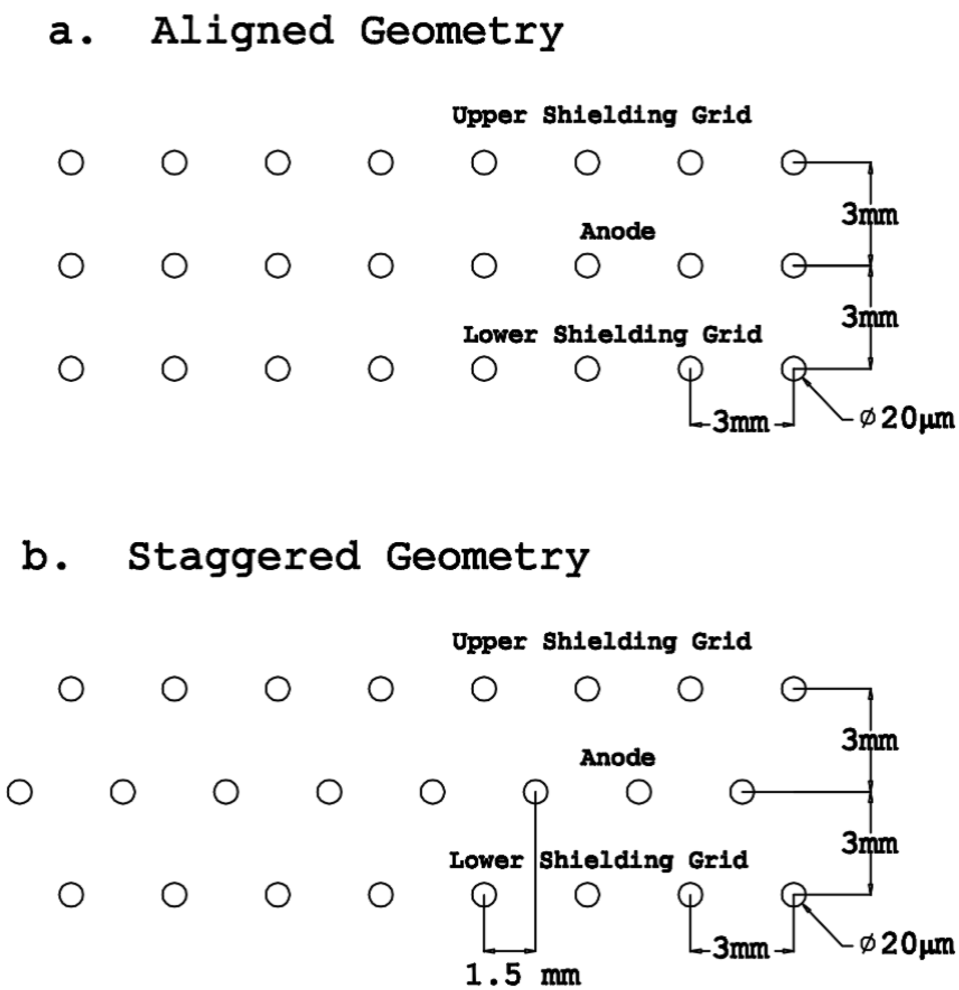

Figure 5.5 Aligned and staggered arrangement for anode and shielding grids. Figure is taken from ref. [8].

5.4.1 Aligned Anode

We have first studied the geometry of a single-phase where the distance between anodes and PMT arrays is only a few cm, much shorter than the Rayleigh scattering length. We note that the detector is fully symmetric, and all results will hold for the top and bottom anode. It is qualitatively concluded that the observed S2 with the aligned geometry will better resemble the response of a conventional Dual-Phase detector [8]. In this geometry, the anode wires are parallel and located in between two wires of the shielding grids above and below. The anode potential is chosen such that the field strength at the wire surface just reaches the threshold for electron multiplication. The drift field is always much lower than the field in the anode gap and the grids are transparent[144]. The drifting electrons are deviated from their straight-line path in the drift region and are compressed into the opening between grid wires. They follow the field lines and will hit the anode wires preferentially from the side. To quantify the effect, we modeled the field in great detail, ensuring that the meshing of the finite element model accounted for the wire diameter of only 20 µm. The overall field distribution in the anode region is displayed in Figure 5.6.a. The applied potentials were 4140 V on the anode with the shielding grids on ground potential. The cathode was -800 V. Only the region of the anode structure with the two shielding grids is shown. As expected the lower grid focuses the drifting electrons which continue their upwards path until they are forced sideways by the field from the upper grid wires. In the plot, we intensified the number of displayed field lines from the cathode to better identify their paths in the zoom of Figure 5.6.b. The lines from the cathode appear like a black band. The low-density lines in Figure 5.6.b originate at the lower grid wire, and no drift electrons follow their path.

In a yet larger magnification, Figure 5.6.c shows the close vicinity of the anode wire. Electroluminescence will start at a threshold of 412 kV/cm (the dashed circle). Electrons from the drift space below will approach the wire in a narrow angular range of 15.5°, symmetrically from both sides. Only electrons within this region indicated in red and within the dashed circle at 17.6 µm can contribute to an S2 signal.

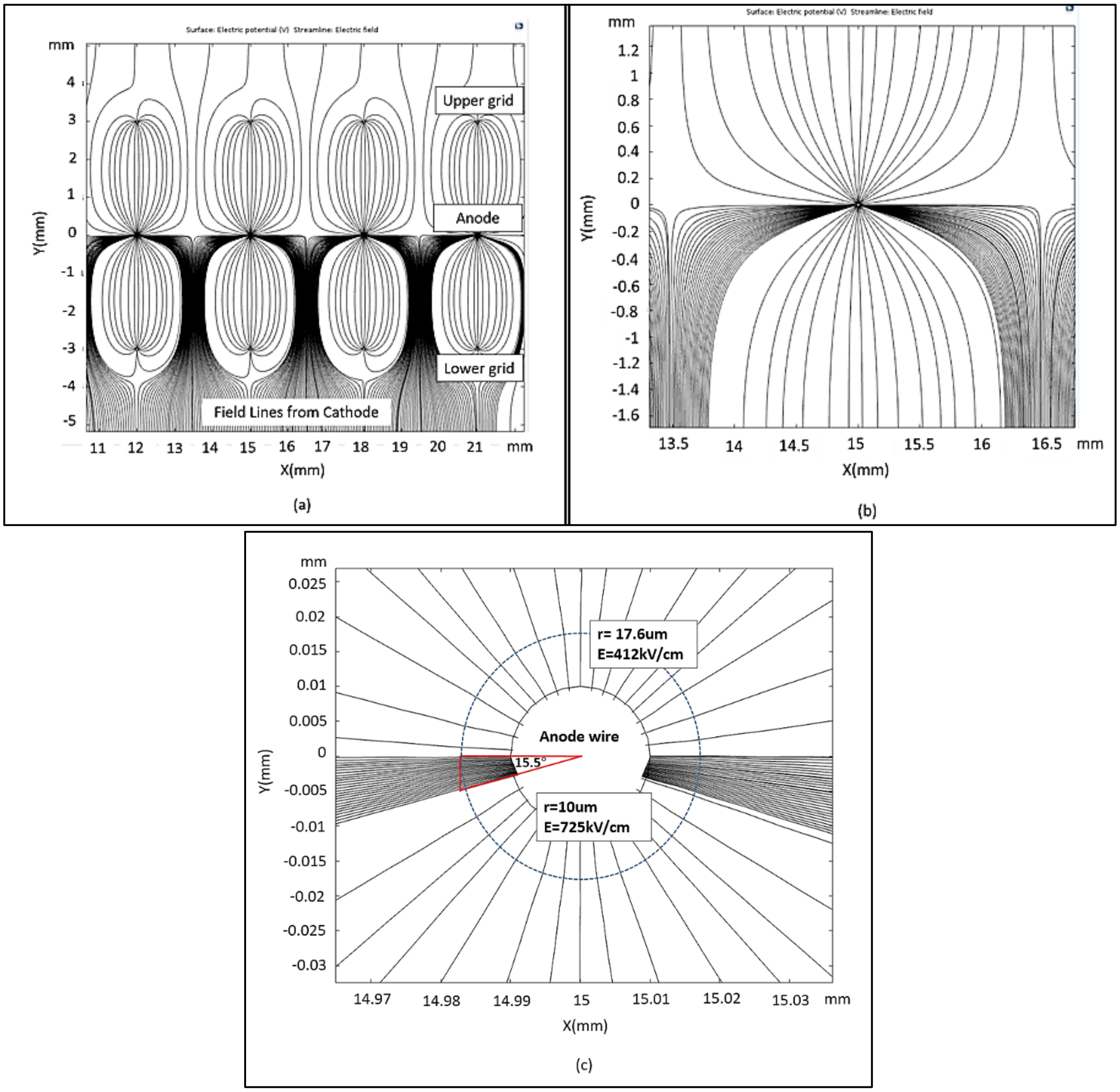

Figure 5.6 a.) Fieldline distribution in the anode region with aligned wires of the detector. The wire diameter is 20um. The spacing between wires is 3 mm. The dense field lines originate on the cathode of the detector and are focused by the grid wires. b.) Zoom in around a single wire. The lines from the cathode are compressed to a very small region and hit the anode wire from both sides. c.) The region in proximity of the wire. The threshold for electroluminescence is at 17.6 µm (dashed circle) from the wire center. Only electrons within the red triangle contribute to the S2 signal. Figures are taken from ref. [8].

The radial boundary of this region is decided by the wire diameter and the anode potential. Choosing the anode potential such that the multiplication threshold is crossed at the wire, the radius of the region with electro-luminescence is given by the 1/r field distribution. Proportional scintillation starts at a field of 412 kV/cm, very high compared to the average field in the gap of order 10 kV/cm.

This means the radius is quite insensitive to the exact wire locations. The angular range, on the other hand, is a consequence of the focusing by the shield wires. By choosing a typical drift field of 1 kV/cm the grid is completely transparent, however, the focusing depends on the ratio the electrons see before and after the grid. Due to the length of the drift region, 1 kV/cm is already on the high side of any typical design. This means the focusing in an actual detector will normally be even stronger.

The S2 light forms a narrow cluster in the PMT array which is at a short distance of only 5 - 10 cm. It now becomes essential that the electrons hit the anode wire from the side. The shadow of the wire is in a horizontal direction, i.e. it for some part falls into a region with no PMTs or PTFE reflectors. The angle of incidence of the electrons on the wire is always below the horizontal. To enhance the signal on the top PMT one can turn the range of hits on the wire by changing the bias of the top grid, leaving all other potentials unchanged. Figure 5.7 demonstrates the effect of asymmetric potentials. The top grid is now on +300 V while the lower grid is still on the ground. The angular range is turned slightly upward. Naturally, the same is true for downward-going photons at the bottom of the detector. Reflections from the gold surface of the wires will also contribute to the cluster in the top, or bottom, array.

The grid voltages can thus be varied to fine-tune for optimal performance. The short distance of 7.6 µm can be passed by the electrons in a very short time. We, therefore, expect very short S2 light pulses.

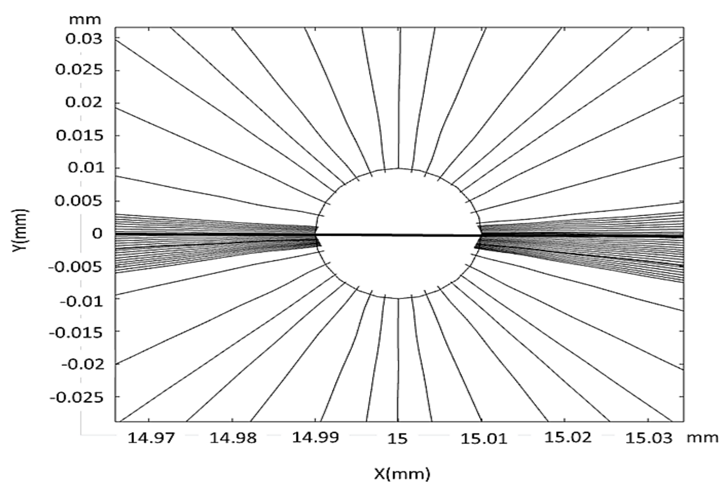

Figure 5.7 Fieldline distribution as in Figure 5.6.c, but with asymmetric grid potentials. The bottom grid is on ground potential and the upper grid is at +300 V. The thick line shows the horizontal. Compared to Figure 5.6c the angular range of incidence is now turned upward. Figure is taken from ref. [8]

5.4.2 Staggered Anodes

A second anode configuration of interest has staggered wires as shown in Figure 5.5b. Naturally, the shift in wire positions changes the field distribution and the electron trajectories. Figure 5.8a shows the simulation of the fields analogous to the previous section. The field lines originating on the cathode are again bent around the grid wire. Now they are focused on the anode wire from below.

In Figure 5.8b, we see the vicinity of the anode wire in a zoom to determine the angle of incidence. The angular range has a slightly larger width than before with 18.7°, but the two ranges from opposites sites are now adjacent. Drifting electrons in an event are only in one of the two angular ranges, not in both. To generate S2 photons the field has again to be above the threshold of 412 kV/cm indicated by the dashed circle.

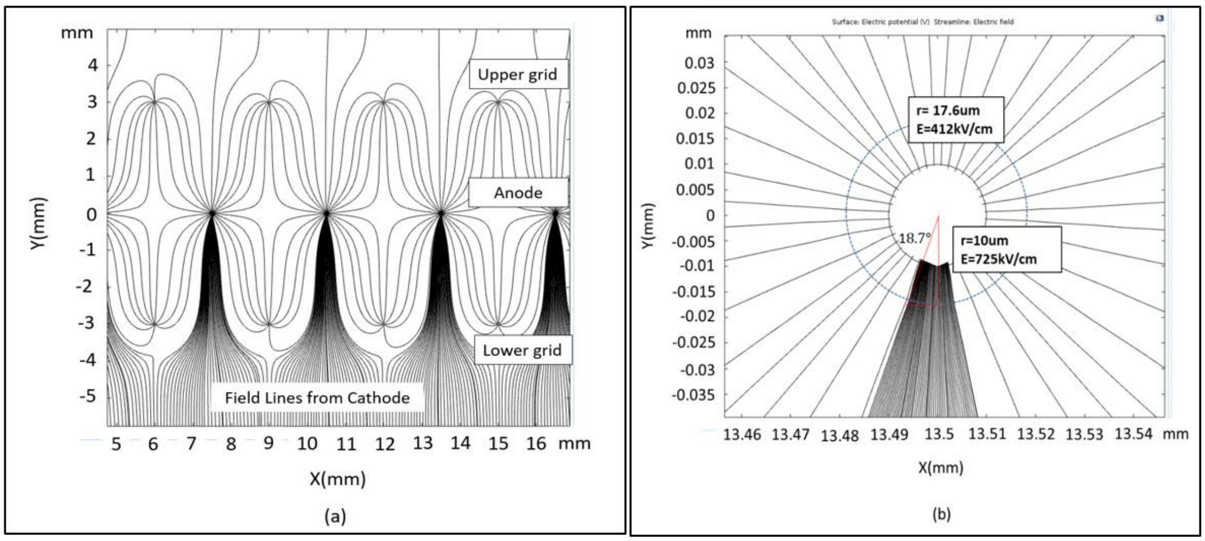

Figure 5.8 a.) Field line distribution in the anode region with staggered wires as in Figure 5.5b. The wire diameter and the pitch are the same as before. The field lines from the cathode are again focused by the grid wires and impinge on the anode from below. The region of electro-luminescence is indicated by the dashed circle. b.) The region in proximity of the anode wire. The two distinct ranges at opposite sides of the anode wire are now adjacent to each other. Figure is taken from [8].

5.5 Assumed disadvantages for DM detectors

The results from SJTU are overlapped with the results from the CAL study and would favor the SP approach. However, the CAL study also observed in their experiment that the drifting electrons followed three different paths in the detector as they used only a single wire in the anode mesh. This, of course, produces different pulse shapes on their anode wire. This would imply a reduction in the energy resolution in large detectors. Furthermore, since the S2 light is produced only in the last few µm before the electron hits the wire surface, they also observed a severe shadowing effect in their top PMT array. This reduces the observable S2 signal when only the top array is used for S2 determination, like in a DP detector. Some of the consequences are listed below, and we try to explain the solution to overcome all of these.

5.5.1 Triple pulse component

The CAL experiment observed the drifting electrons from a ^{241}Am alpha source on the cathode. The range of the alphas is of order 20 µm, i.e., the events are point-like. The ionization electrons drift toward the anode assembly, following the field lines. Close to the shielding grid, the field lines are focused to pass through the spaces in the grid toward the anode. Depending on the exact location of the alpha, the drift path either goes straight up to the anode wire or passes through the adjacent spaces in the grid. The path is different in the three cases, producing different pulses. The different paths are shown on the left side of Figure 5.9. This is the original plot from the CAL publication. However, the implemented geometry is not a good approximation of a DM detector. There will never be only a single anode wire, but an array of wires like in an MWPC. Adding the next adjacent wires will change the field lines for the paths on the two sides. These drifting electrons will be guided to the adjacent anode wires. This is illustrated in the center in Figure 5.9.b, showing the field lines if the adjacent anode wires would have been present. The drift path, and thus, the pulse shape, is then indistinguishable from the central channel. Figure 5.9c shows the field distribution in a detector similar to the CAL detector, but with multiple anode wires. This discrepancy between CAL and SJTU results is caused by the use of a single anode wire.

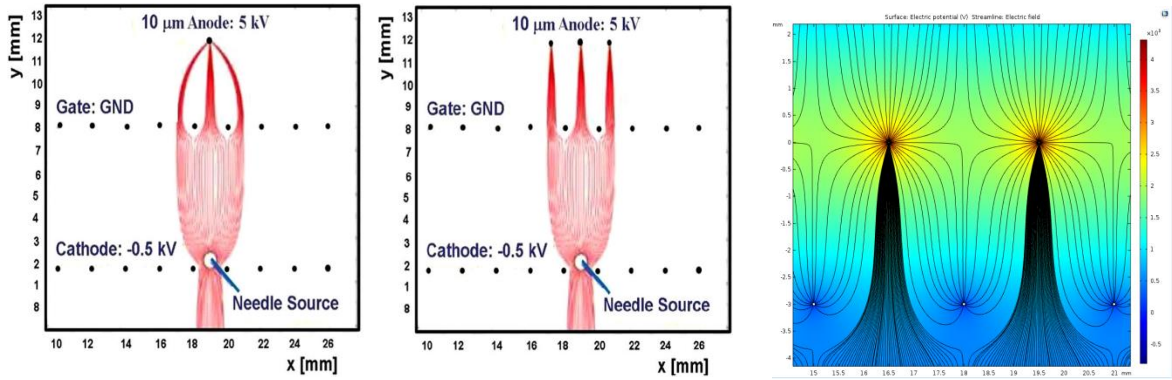

Figure 5.9 Drift paths of ionization electrons from a point source to the anode wire in the CAL experiment. Reproduced from ref.[5]. a) On the left, the original plot, i.e., the case of a single anode wire. The three different flight paths can be identified. b) In the center, the case with three anode wires. The plot was not redrawn but modified by symmetry arguments. All the flight paths are now the same, but the two additional components end on the adjacent anode wires. c) The field simulation for staggered anode mesh in SJTU.

5.5.2 Effect of shadowing

With an anode wire diameter of 10 µm as in the CAL study, the drifting electrons will produce proportional scintillation once the 1/r field is above the threshold (412 kV/cm). Enlarging the wire diameter would push the start of the region farther away from the wire; the field strength at the surface should remain below the threshold for electron multiplication. Staying within these limits practically means that the maximum path length over which proportional scintillation is produced is very short. For easy estimations, it is typically less than the wire radius. Naturally, such a short light source close to the surface of a wire will always cast a shadow.

Figure 5.9a shows that the electrons in the CAL geometry hit the wire from below. Most of the light for the top PMT array is blocked by the wire. The CAL group calculated the relative light on the top and bottom PMT in dependence on its distance from the wire surface. The bottom PMT sees a constant amount of light, but the top PMT not only has much lower light collection efficiency (LCE) but also varies dramatically with distance. With their 10 µm wire, however, proportional light will only be produced in the last 5 µm. Since the electrons are focused on the center of the wire, one might expect that the LCE would be 0 at very small distances from simple ray tracing, but there are reflections. At best, this calculation for LCE is misleading.

Figure 5.6 a shows the field distribution for the SJTU geometry with aligned wires. The length of the electron path is only 7.6 µm. The electrons are deviated around the bottom grid wire and continue until they are bent toward the anode wire by the field lines from the top grid. No electrons are hitting the anode from the bottom, i.e., in the region of maximum shadow for the top PMT. All the electrons approach the wire from the side, and a large fraction of the proportional light will be observed with the top PMT. This is complemented with more photons being seen by the bottom PMT. Thus, both PMTs see an S2 pulse.

5.5.3 S2 efficiency

In the data analysis, the S2 light is used for two purposes, total charge measurement and position determination in x-y. We simulated drift electrons according to the geometry of Figure 5.5a. They were weighted with the local electric field strength obtained from the field distribution of Figure 5.6. The average number of photons is about 20 per electron. About 37% of all photons are impinging on the wire. But some of the photons are reflected on its gold coating. These also contribute to the total charge measurement with the S2 signal. The reflectivity [146] of gold at the xenon wavelength is roughly 30%. Despite shadowing about 74% of the S2 light is emitted into the detector volume.

The group from CAL increased the anode potential to achieve an S2 gain comparable with a dual-Phase detector of about 200–300 photons/electron. Thus they included a factor of 14 from electron multiplication in their signal. But they used very thin wires (10 µm), reducing the effective path length and thus the electroluminescence by 50%. Thicker wires, e.g. 50 µm, could provide an additional signal increase by 2.5. We also can raise the anode potential. We had chosen reduced field strength to avoid fluctuations from electron avalanches. But at very low energies, i.e. our main region of interest, the added fluctuations from small gain enhancements is outweighed by the improved counting statistics. Thus, if the S2 gain should limit the sensitivity at low energies, we can raise the HV and thus enhance the signals. The added fluctuations might be much smaller than the statistical errors from the low counting statistics. We remember that the warning about the added fluctuations stems from gaseous detectors with an avalanche gain of several orders of magnitude.

The overall light yield of S2 depends on many design parameters such as the quantum efficiency and the noise performance of the PMTs. In the large arrays, the light is shared by many PMTs, and at low energies, most of them will only detect a single photoelectron. The total light collection efficiency of a Single-Phase detector can be comparable to a Dual Phase. It depends on the final optimization of several detector parameters, for example the photocathode coverage of the top array. To have a fully symmetric geometry in our design and to optimize the light yield we have chosen a tightly- packed hexagonal array, identical to the bottom array.

The second use of the S2 light is to determine the x-y location of any event. We note that the z coordinate is determined from the timing of the S2 signal relative to S1, which is used as t0.
Since sufficient S2 light is contained in the cluster for x-y determination, in a Dual-Phase detector the event location is normally derived only from the top array. Our Single Phase geometry provides a comparable PMT hit cluster. Therefore, it will not be necessary to also use the light distribution on the opposite PMT array.

It is sometimes reported that the x-y position of an event can also be determined from the opposite PMT array alone, i.e. the bottom array in a Dual-Phase. These observations were obtained in much smaller detectors. For a very large detector, it is not obvious that this is still valid. The S2 photons on their long path through the detector are subject to Rayleigh scattering and possibly multiple reflections on the PTFE walls. Since the Rayleigh scattering length in LXe is of order 30 - 40 cm, the original position information of these photons might be entirely lost on a 2 m path length.

The number of photo electrons in the top PMTs might be too low for an accurate position reconstruction at very low energies. At the lowest energies, a limited amount of multiplication might be a better optimization for detectors. A lower gain does not mean a worse resolution, since the statistics of the measurement is dominated by the number of drifting electrons, which remains unaltered. In the data analysis, most calculations involve both the S2 and S1 signals. In all these cases, the weaker S1 signal dominates the error.

5.6 Electric Field dependence on the geometry

The electric field strength plays an important role to measure the proportional scintillation. The formula for the electric field strength (E) [3],

$$\boldsymbol{E} = \frac{\boldsymbol{V}}{\boldsymbol{r}\left(\boldsymbol{ln}\left(\frac{\boldsymbol{r_2}}{\boldsymbol{r_1}}\right)\right)}$$

Where, r_1, r_2, and r are the radius of the wire, spacing between wire planes, and distance from the center of the wire, respectively.

We have one anode mesh along with two shielding grids, one is above, and the other is below the anode mesh with the spacing of 3 mm. All the wires are 3 mm apart from each other in all meshes. The diameter of wires is 20 µm. Therefore, r_1=10 µm and r_2= 3 mm. The value of r_1 and r_2 is constant in this calculation. The value of r changes as we move away from the center of the wire.

The value of E is maximum at the surface of the wire where r =10µm. As we go away from the wire it increases and due to which the value of E gradually decreases. To avoid the electron multiplication around the anode wire we have set the value of E at the surface as 725 kV/cm [5], which is the threshold point of electron multiplication. To obtain the required electric field at the wire surface we have to set the anode voltage as 4.14 kV. Figure 5.10 shows the electric field strength at different points from the wire center.

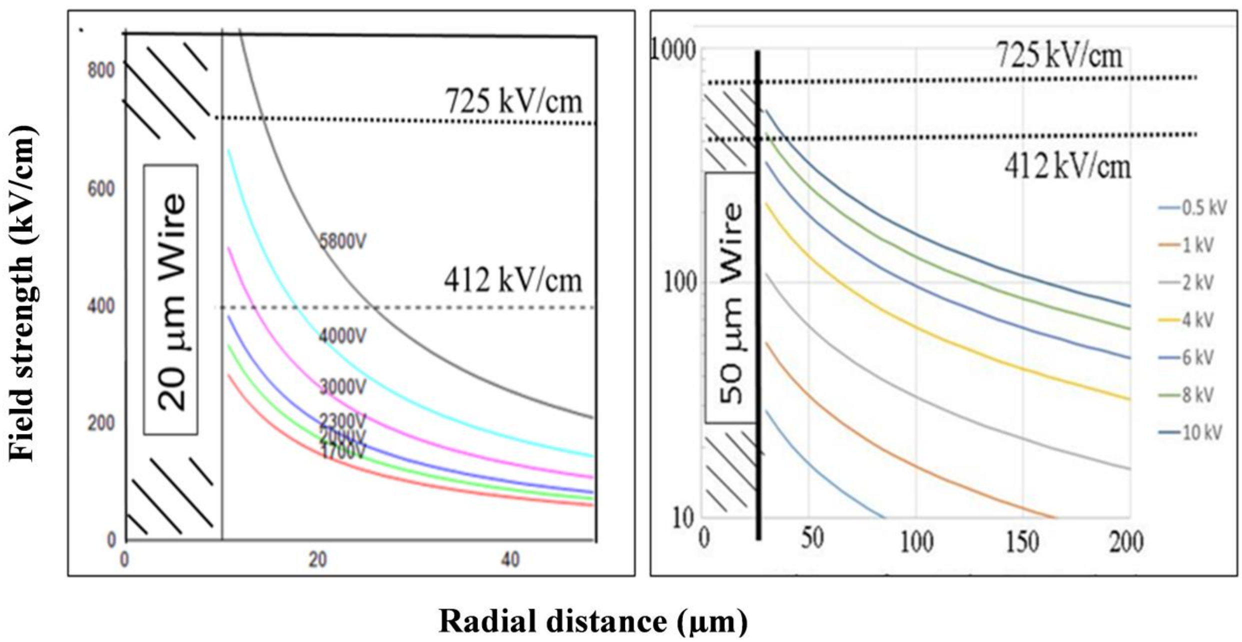

Figure 5.10 The calculation of electric field strength for the distance from the center axis for a 20µm (left) from ref. [6] and 50µm (right) diameter of the anode from ref. [140].

5.7 Electrode design

The most challenging parts of the TPC are the electrodes. All of the electrodes must be transparent so the scintillation light can be observed by the

PMTs. The shielding grid is also fully transparent for the drifting electrons [144], and we do not have extraction inefficiency. Also, meshes are either etched or electro-formed. The metal is not circular in cross section, but approximately square. The radius of curvature in the corners thus produces a higher 1/r field which leads to the undesired electron multiplication for some events. We observed this effect with anode meshes in PandaX I and II, as discussed earlier. But in a DP detector, one can correct for the spike at the end of pulses but lose the energy resolution. In single phase, however, the pulses are much shorter, and there is no way for corrections.

As wire diameter for the anodes 20 µm would be the optimal value. A larger value would provide more amplification which might not be necessary. Naturally, the thinner the wire the more delicate they are. Also the path length over which proportional scintillation occurs becomes shorter. In our case we get 725 kV/cm on the surface of the wire below 5 kV. We remember that a wire diameter of 20 or 50 µm was the standard for most MWPCs. For the shielding grids and the cathode, any diameter would do since no field lines end on these electrodes. But the same arguments concerning mechanical forces and robustness of the structure apply again, besides the requirement of optical transparency.

The spacing of the wires can be 3 – 5 mm. A larger spacing might make the stretching easier and enhance optical transparency, but we should test the final value. . The precision of the wire location is not as critical as in a dual-Phase detector. Within the wire plane the position resolution is determined by the granularity of the PMTs, i.e. much more coarse. Perpendicular to the wire plane the location changes the path length in a dual-Phase, and thus the gain. In a single-phase, the proportional scintillation is only produced in the last 10 µm or approximately radius of the wire. Field simulations show that at such small distances the field does not significantly change even if the wire is dislocated by a mm. This also means that sagging of the wires due to gravity or the electrical field will not significantly reduce the resolution.

5.8 Advantages of 'Single-Phase' technique

The limitation of DP can be overcome by the SP technique:

1. No more Liquid Level control and monitoring

In SP detectors, the liquid level is above the PMT array. Thus it has no more influence. The density of LXe is nearly constant with the variation of temperature and gas pressure. Therefore, the operation of a single-phase detector is much more feasible and free from level control. In the DP detector, presently, the leveling is quite good enough in the DM detectors. XENON uses a diving bell to maintain the liquid level in the detector. However, as we will go to the higher mass detectors with a detector radius of more than a meter, the liquid leveling will not be that easy task. The 1-meter-long wires can sag and disturb the gas gap. The dual-phase detectors have to perform under exceptionally stable circumstances.

2. Anode HV in the liquid

Unlike the DP detector, in the proposed SP detector, all high voltage cables are in the liquid. So there will be no spurious HV breakdown.

3. Better long-term stability

As we do not need to care about the liquid level controlling and high voltage management, it automatically stabilizes the system for better operation.

4. No Extraction Efficiency like in Dual-Phase

There are no extracted electrons in the single-phase detector.

5. Cathode HV for away from PMTs

The SP detector gives the liberty to increase the number of drift spaces. For example, we can instrument a cathode in the center of the detector and two anode arrangements on the top and bottom sides of the detector.

6. Detector Segmentation in z possible

SP technique provides the feasibility to divide the drift spaces in the z-direction in the SP detector system.

7. Improved 'double event' recognition

Detecting the location of the S2 pulses with a large PMT array determines the position of the interaction with good precision, even with the granularity of 3’’ PMTs. Thus, we get a good spatial resolution in the order of a few mm. However, this only applies to single-site events. At high energies, gamma-rays prefer Compton scattering with a small scattering angle, i.e., with low energy deposition. After scattering, they have nearly the same energies and can Compton scatter again. We can reject such an event as ER if we can separate the two interaction sites. The position resolution in the anode plane (x–y) is very good with the PMT array, but the ‘Double Hit’ resolution is not. We can still separate the two locations in the z-coordinate, i.e., in case they are separated in this projection.

8. Active LXe shield for Top PMTs

Present large size Dual-Phase detectors already use the feature of self-shielding in LXe. The field cage of the detector has to be surrounded at the sides by ‘dead’ xenon. 1cm would be sufficient for dead xenon as the dielectric strength of liquid xenon is several 100 kV/cm. But usually, more space (~5cm) uses because we need space for the cables of the lower PMT and the cathode. One also wants to have level sensors during filling.

It is difficult to insert the detector in its vessel if the space is small. This outer layer is thus turned into an active shield against γ - and X-ray backgrounds, e.g. from the radioactivity of the detector vessel and the outside of the detector. The strongest background in the LXe detector stems from the low activity PMTs themselves. In a Dual-Phase detector, it is not possible to shield this background since the anode has to be in low-density gas. In the single-phase geometry, all the volume in front of the PMTs is filled with dense liquid. Photons from the PMTs are attenuated as well. We cannot avoid observing S1 signals from the background interacting in the shield region, but no S2 will be produced if there is no electric field. The region in front of the PMTs is field-free if they are powered on the anode with positive HV, i.e. the photocathode and the case of the PMT is on the ground. In the case of negative PMT HV, we easily can shift the potentials of the anode and the shielding grids. We bias the shielding grids with a potential more negative than the PMTs. Of course, the anode potential has also to be reduced to keep the same field distributions.

Along with all these advantages, in Single-phase TPC we can reduce the maximum drift time and distance by dividing the drift space. This can also help to reduce the effect of attachment to electro-negative impurities and reduce the amount of cathode HV needed.

5.9 Possibility of Pulse Shape Discrimination (PSD) for NR-ER separation in LXe

PSD might be possible by using many faster PMTs for a 'Quasi Background Free' detector. Simulations of PSD look very promising, but it might depend on the effect of the Rayleigh scattering of S1 photons. The Rayleigh scattering length is only about 40 cm in LXe.

PSD technique for background rejection (~10^{-8}) is a quite acceptable technique in LAr detectors. But it is quite difficult to implement this technique in the LXe system due to the small timing differences between NR and ER (2 and ~22 ns), therefore the background reduction will never be that efficient. To use PSD in LXe we need a faster PMT read out and provide a "no reflection environment" which means no PTFE reflectors and only PMTs on all side walls . See Figure 5.11.

There is a simulation study [147] in which the Baker and Cousins algorithm [148] is used. It is predicted that an additional 1/100 in background rejection might be possible in LXe detectors by PSD. There are two likelihoods, one for NR-like events, and the other for ER. The discriminator (Q) is defined by the ratio of the likelihood of NR testing to the likelihood of ER testing.

$$\mathrm{Q} = \frac{\chi^2(y_{NR};n_\alpha)}{\chi^2(y_{ER};n_\alpha)}$$

Where χ is the Baker & Cousins binned likelihood chi-square. The functions y_{NR} and y_{ER} are the time distribution of the theoretical model describing NR and ER signals. However we note again that the PSD technique in LXe has not been established experimentally yet. If we could reach the factor 1/100, the sensitivity of the experiment for DM particles would be greatly enhanced. It might be called a 'Quasi Background Free' detector.

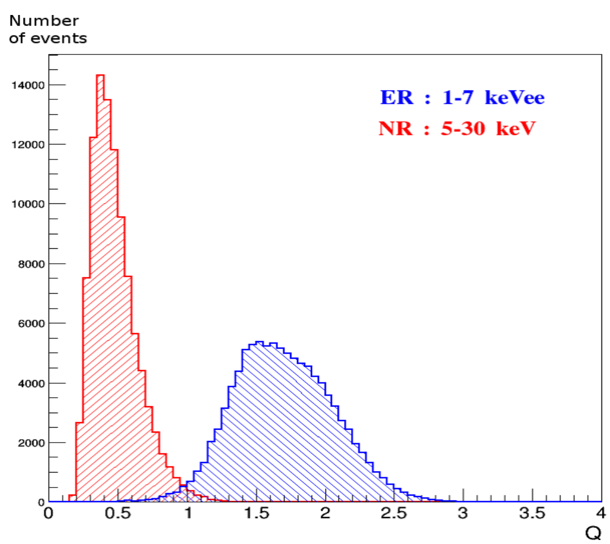

Figure 5.11 Discriminator profiles for NR (red) and ER (blue) events, 10000 events each. Figure is taken from ref. [147].

Table 5.1 Comparison between single and dual-phase techniques

S.No		Dual phase	Single phase
1	Leveling	Anode should be parallel to liquid level. Keep distance in which proportional scintillation takes place(0.1mm)	No need of leveling No leveling of detector Ripples on the liquid surface do not affect the S2 signals
2	S2 pulse	Depends on E/p, electric field strength and pressure above the liquid, any change in them influence the data	Proportional scintillation not sensitive to change in pressure because of large thermal inertia of Liquid Xenon
3	HV connections	Data acquisition has to be interrupted because an excessive current to the anode caused the HV power supply to trip	HV connections are entirely submerged in liquid xenon.
4	Drift charge	Charges drift up to the liquid level to be extracted before they can generate the S2 light	No such condition Electron drift can be used in all direction

By comparing with DP we found that the situation in an SP detector is very different from DP. There is no extraction efficiency, and the S2 production only depends on the first 5–10 μm around the anode wire. Field calculations show that displacing the anode wire by a full 1 mm does not significantly change the field in this region. Although it is convenient to have a strong S2 signal, all the light has to be observed by the same PMTs.

6 Proposal of a large multi-ton LXe single-phase detector

PandaX 4T has increased the detector mass to suppress the ambient background and search the lowest possible cross-section for WIMPs. DARWIN with 50 tons of planned detector mass predicts its sensitivity of the order of 10^{-49} cm^2. Thus, going to a large mass, we are reaching the best sensitivity range but at the same time entering the region of the irreducible neutrino background or "neutrino floor" by coherent neutrino-nucleus scattering (CNNS). The sources of this background are:

1. Solar neutrinos (^{7}Be, pp, ^{8}B neutrinos etc.) for lower DM mass (<10 $GeVc^{-2}$) and

2. Atmospheric and diffuse supernova neutrino background (DSNB) for high DM masses.

Detection of any WIMP signal will promote the further increment in the detector mass for the analysis of properties of that signal. Furthermore, if we get nothing, we must go with even larger mass detectors to reach a better sensitivity level. Ultimately we have to explore the neutrino floor region in any case. A lot of 'new physics' might be hidden there.

The question arises that if no DM signal is detected, what is the future of such massive detectors? What if Nature decided differently? Will all the efforts and time have been invested for nothing? Here, the idea of a large mass observatory comes to mind, not only for DM search but also to investigate other exciting physics areas such as solar neutrino searches, supernovae neutrinos, double beta decay (DBD), and many more. As often during history, many significant findings will be unexpected and unpredicted. Thus the expansion of mass also expands the physics reach of large mass detectors. These detectors not only need a considerable amount of money but also consume a lot of time and effort. To utilize all, we are proposing a low-energy observatory for dark matter detection.

We are looking towards the LXe detector of mass in the range of 50-100 tons. This scales up the detector mass 10 times from the existing detectors. The large mass is not enough to improve the sensitivity, but the detector should have a good background reduction capacity. The large LXe detector will search for solar neutrinos in the low-energy region and better results in DBD in higher interaction energy regions. Furthermore, it provides better discrimination between NR and ER signals by applying the S2/S1 method and maybe the PSD method together.

However, the PSD method has not been established in LXe experiments. Until now, we only have a simulation study [147], which predicts significantly improved results with PSD in LXe. However, this requires much faster PMTs, GHz electronics, and the elimination of all light reflections.

The geometry of the assumed detector provides a cylindrical active volume of 2.5 m diameter and 4 m height, corresponding to roughly 60 tons of LXe. A conventional Dual-Phase detector with these dimensions is shown in Figure 6.1a for comparison. The active volume is delineated by the cathode on negative HV and the anode structure a few mm above the liquid level. The active volume is viewed by the top and bottom PMT arrays with a total of 1914 PMTs. A conventional field cage surrounds the active volume providing the homogeneous electric field. The cathode and the field cage determine the electron drift but do not influence S2 production directly, which will be our central theme.

We can easily achieve two drift spaces with the single-phase technique by removing the cathode to the center and introducing a second anode structure in front of the bottom PMTs, as shown in Figure 6.1b. The liquid level, so critical in its position in a Dual-Phase, is somewhere above the top PMTs. Thus, the detector is now entirely symmetric. Also, precise leveling of the detector is no longer required.

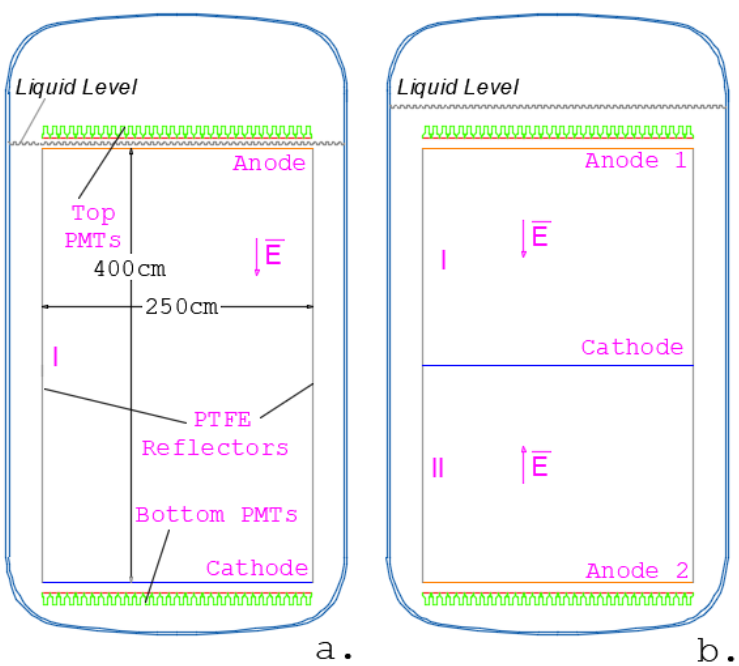

Figure 6.1 Dual-phase and single-phase geometry. In a single-phase, the liquid level is above the upper PMTs. Figure is taken from ref. [8].

A single-phase geometry alleviates the design of the mechanical support since leveling and control of the liquid level is superfluous. All HV connections are now within the LXe, which is an excellent insulator. Thus, we expect much better stability during a long time operation. In addition, it also grants much more freedom in the design. The construction of a multi-ten ton detector is now similar to the arrangement of several modules without increasing the number of readout channels. We mentioned that dividing the active volume will reduce the cathode HV, the diffusion of the drift electrons, and the attachment to electro-negative impurities linearly with the number of drift spaces. We studied a detector according to Figure 6.1 b with two drift regions, each 2 m long. Now we shall strive for another factor 2 by forming four drift spaces.

6.1 Single TPC

A simple way of forming four drift spaces in our detector is to introduce an additional anode structure in the center and provide two more cathodes. Such a design is shown in Figure 6.2a. We need only two PMT arrays, and the number of feedthroughs, cables, and electronic readout channels remains unchanged. However, this design has a significant drawback. We can measure the z - position of an event with perfect accuracy, but we have ambiguity as to the drift space. The narrow cluster in the hit pattern can identify the outer drift spaces (I and IV in Figure 6.2a). For the other two spaces, all the S2 light is produced at the central anode. Thus, an event in space II would be indistinguishable from one at the same distance in space III.

To resolve this ambiguity, we can change the center anode to a staggered wire geometry shown in Figure 5.5 b. The angular range of the electron impact is nearly the same as for aligned anodes, but the electrons approach the anode vertically from only one direction. The shadow of the wire will cover most of the PMT array in this direction, but it will not affect the opposite one. If we include reflections on the wire, we expect the exact light yield but concentrate on the opposite PMT array. The strong asymmetry in light intensity will identify the drift space, II or III, which contained the event. Of course, the z - position is still measured with high accuracy by the drift time within a drift space. Although we can measure the S2 amplitude and z - position, it might be challenging to achieve a good x-y resolution required for the radial fiducial cut. Prior studies with small detectors showed that the x-y could be extracted from the hit pattern at some distance. However, in our case, this distance has grown to more than 2 m, far beyond the Rayleigh scattering length in LXe of 30 - 40 cm [149]. Additional multiple reflections on the PTFE walls might wash out the remaining position information. Although we have an attractive geometry, it might only be used after additional simulation studies and experimental verification that the x-y localization is still sufficient.

6.2 Dual TPC

We still form 4 drift spaces in a less elegant but risk-free way with a Twin TPC detector according to Figure 6.2b. Each of the two TPCs is independent of the other with its own PMT arrays. They have only half the height and are stacked on top of each other. We realize that we need twice the amount of PMTs and readout channels. Moreover, we have to accept a gap between the detectors for the arrays. With the presently favored PMTs, we expect this dead space to amount to 50 cm, determined mainly by the length of the PMTs. In the future, we hope that one can reduce the dead space to less than 10 cm when novel photon sensors become available. There are two very promising developments:

1. A 2" square tube in metal-channel design [150] with an overall length of 25 mm is already available in low RI technology. However, the radioactivity [151] is still higher than the commonly used PMT. A reduction might be possible in the future.

2. We also would expect silicon photomultipliers (SiPMs), often called Multi-Pixel photon counters (MPPCs), will come of age for DM detectors before a 60 ton can be realized.

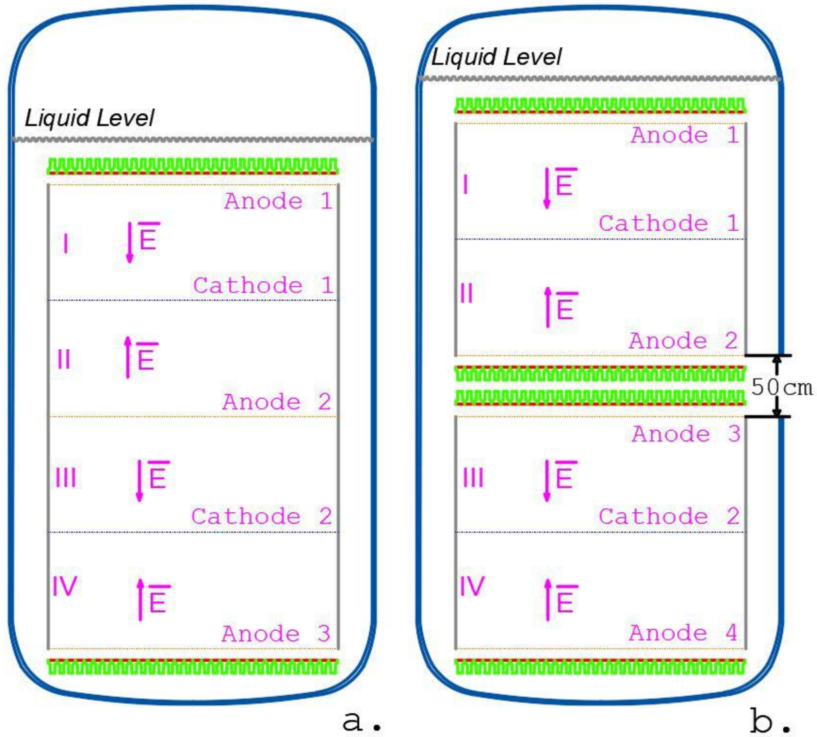

Figure 6.2 Schematic comparison of detectors with four drift spaces (a) Single TPC with the additional anode in the center, (b) Twin TPC with two identical TPCs on top of each other. Figure is taken from ref. [8].

6.3 Prerequisites for the detector

6.3.1 Photon sensors:

Some PMTs are specially designed for LXe working conditions. They are highly sensitive towards the VUV light with low radioactivity and are designed to withstand the low-temperature and elevated pressure when immersed in LXe, i.e., below -100 ℃ and up to 5 bar pressure. Hamamatsu R11410, R8520, and R12699 are some of the photomultipliers in this field. For a detailed comparison, see table 3 below. The last two PMTs in the list have a metal-channel structure and are thus very short in length.

CAL and SJTU used R8520 PMTs for their experiments. These PMTs have square bi-alkali photocathodes measuring 21×21 mm^2 in area. The CAL group used two such PMTs in their experiment, whereas two arrays of 4 PMTs each were used in the SJTU setup in the top and bottom of the detector. These PMTs measure S1 and S2 signals in the system.

For optimizing the detector, we would choose Hamamatsu R12699 PMTs as they have a larger area, 2" × 2" and even shorter length. However, R11410 PMTs are currently used in many experiments since they are 12 stage PMTs with high gain.

R11410 PMT is a 12-stage, circular 3" tube, about 12 cm long without a base. It is optimized to be immersed in LXe and detect the VUV scintillation light. The Quantum efficiency of the tube depends on the selection but is above 30%. So far, the R11410 has a very low internal radioactive background. A distinct disadvantage of this tube is its long envelope. A large array will necessarily include a dead volume in between the tubes. Even more problems in a very large detector stem from the weight, and the buoyancy of the PMTs then submerged in liquid xenon. With a weight of about 300 g and buoyancy of about 600 g, the R11410 will require a very solid and heavy structure to hold the PMTs in place, considering that there will be a few thousand of them. A further drawback of the large construction is a Transit Time Spread(TTS) of 9 ns, rendering background rejection by PSD ineffective, as shown in three independent studies at SJTU [147, 152] and NIKHEF [138]. See Figure 6.3, where Q represents the discriminator. For the TTS of 4 ns, the NR peak is shifted, and ER peak is wider than NR. Discrimination between NR and ER is quite effective with lower TTS. In contrast, at 9 ns TTS, most of the discrimination power is lost.

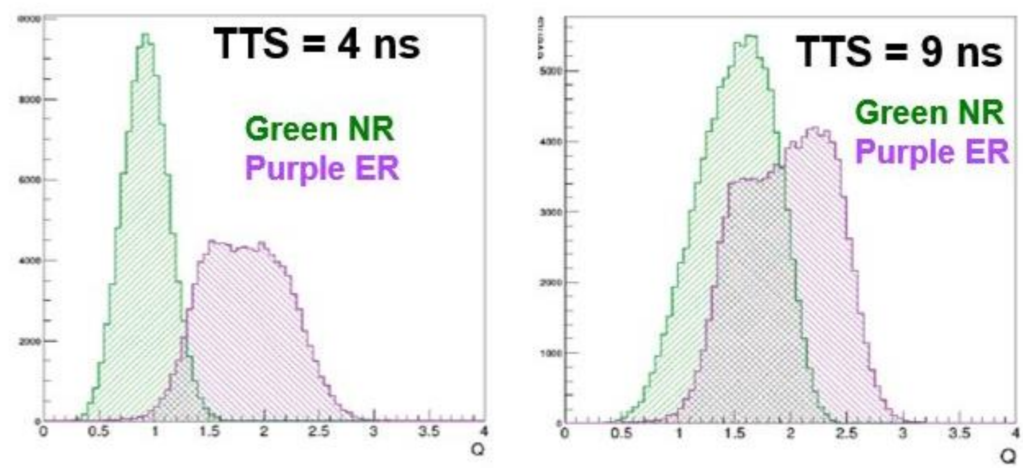

Figure 6.3 Difference between NR and ER signal due to different transit time spread (TTS). The left plot is for the R8778 PMT, 2" hexagonal PMT used in XMASS. The right plot is for the R11410, a 3" round PMT used for XENON and PandaX. Figure is taken from ref. [147].

Hamamatsu R8520-06 is 1-inch square PMT with 10 stages in metal channel technology. They were designed for low radioactivity and later on improved after intensive feedback from the XENON group. XENON 100 used these PMTs [113] designed by Hamamatsu, especially for LXe low-temperature experiments. As a result, they have 70% photoelectron collection efficiency.

Hamamatsu R12699 is a 2" square metal-channel PMT with an overall length of only 14 mm. The original was designed for KEK (High Energy Accelerator Research Organization) with an 8x8 anode matrix adapted to be submersed in liquid xenon. A modification was prepared with only four anodes and low radioactivity. The tube is very fast with 280 psec TTS (FWHM), quantum efficiency above 30 % at 178 nm, and improved collection efficiency to 90 %. It has a maximum pressure rating of 5 bar. The weight of the tube is 103 g, and the buoyancy is less than 2 g. Two of the tubes were counted for radioactivity and found to be about a factor of four higher than the R11420 on a per-area basis. Therefore, Hamamatsu might increase the number of stages by 2 for higher gain and maybe to further reduce radioactivity in the future [153].

Table 6.1 Characteristics of different PMTs

PMT type/parameters	**R8520 1”Square PMT**	**R12699 2” Square PMT**	**R11410 3” round PMT**
Effective area	20.5mm×20.5mm	48.5mm×48.5mm	π×32mm×32mm
Supply voltage	900V	1100V	1500V
Quantum efficiency at 175nm	30%	30-33%	30%
gain	1×10^6	1.5×10^6	5×10^6
Rise time	1ns	1.2ns	5.5ns
Transit time spread(TTS)	750ps	410ps	9ns

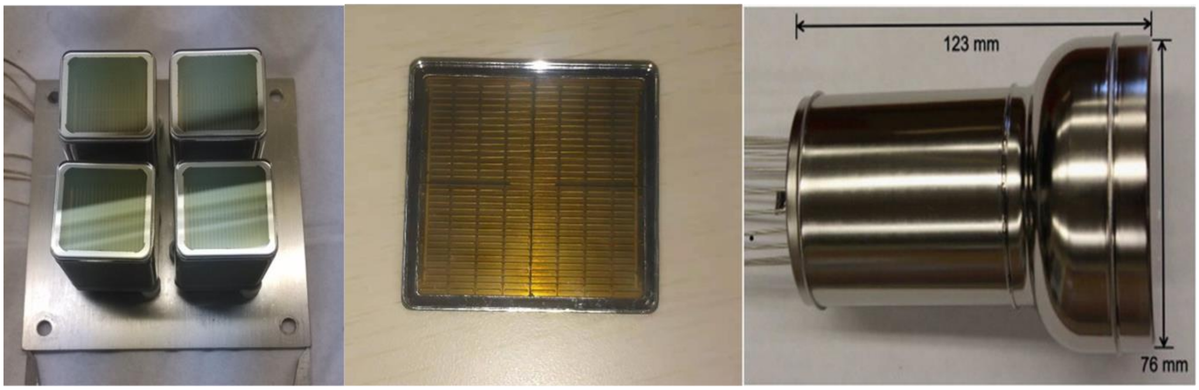

Figure 6.4 Different Hamamatsu PMTs. left, R8520 PMTs; center, R12699 PMT and right, R11410 PMT

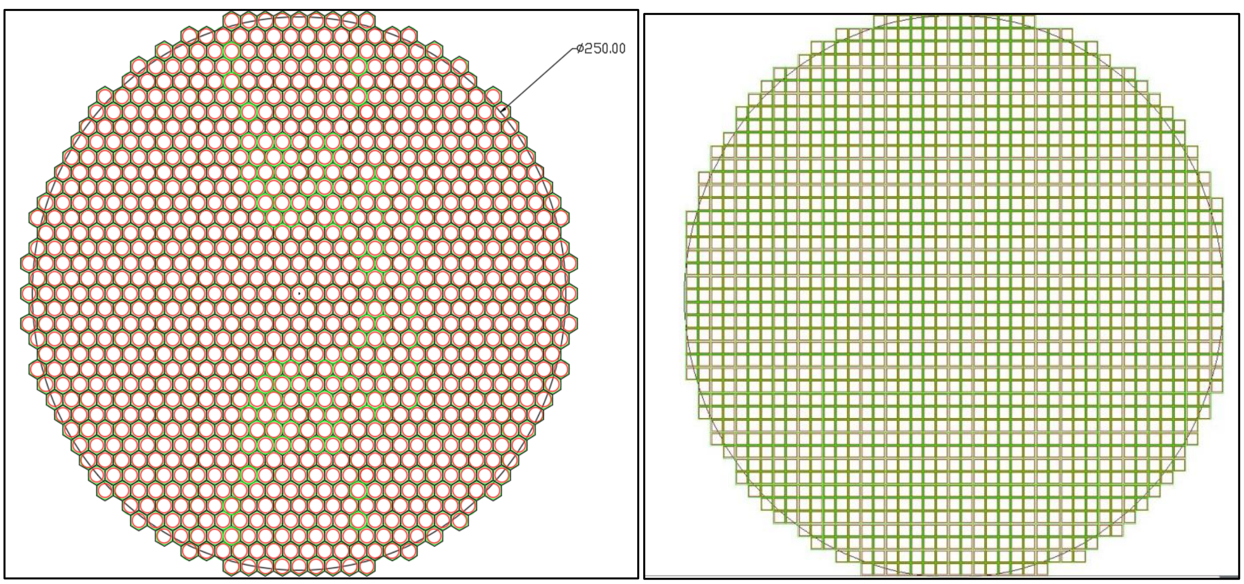

Figure 6.5 Schematic design for top and bottom PMT array. Left, Hamamatsu R11410 round PMTs and Right, Hamamatsu R12699 square PMT.

Apart from these PMTs, **Multi-Pixel Photon counters** (MPPCs) are a good choice for future detectors. They are also called silicon photomultipliers (SiPM). It is a solid-state photodetector that uses multiple avalanche photodiode pixels operating in Geiger mode. However, the present sensors are noisy even at low temperatures. MPPCs have been studied and characterized for use in xenon by MEG (Mu to E Gamma) experiment [154].

6.3.2 PMT Arrangement

We would have two or more anode planes (Figure 6.2) but only two PMT arrays, one on top and one on the bottom. The arrays need changes, in any case. First, we have to reduce the buoyancy of the PMTs for a lighter overall construction with fewer materials causing radioactive background. For this, our preferred choice is 2" R12699 PMTs. However, as most of the current detectors are using 3" PMTs (R11410 from Hamamatsu Photonics), thus first we have chosen the 3" PMTs for our calculation, and then we have considered 2" PMTs too.

The single-phase geometry is fully symmetric as for up and down, i.e., our two arrays are identical. Also, unlike PandaX IV, we would like to have a PMT array extending at least 5 cm beyond the area of the anode. These 'outside' PMTs are very important for position determination at the edges. At least we would like to have ½ ring of outside PMTs. Furthermore, the arrays should be closely packed, providing as much photocathode coverage as possible. For a 2.5-meter diameter, simple counting results in approximately 957 round PMTs for each top and bottom array. Thus, 1914 PMTs in total.

In an initial implementation, due to the limited availability of PMTs, we might have a detector with PTFE reflectors. A PTFE thickness of 1 mm is fully sufficient according to the Michigan tests [155]. We can divide the drift gap into two parts by placing the cathode in the middle and instrumenting anode arrangement above the bottom PMT array.

To avoid all reflection, we need to replace the PTFE wall from the sides with PMTs. To design this detector with a 4 m height, we need a total of 48 hoops with a detector diameter of 2.5m. Each hoop has a perimeter of 7.85 m, corresponding to 100 PMT or 4800 PMTs for the side walls. Together with the top and bottom PMTs, we would have 6714 PMTs.

The number of PMTs increases if we switch towards the 2" PMTs. We need nearly 1500 PMTs for each PMT array and 9180 PMTs for the sidewall, in total 12180 PMTs.

6.3.3 Read Out of PMTs

The readout of a large LXe DM detector followed the same design philosophy as XENON10. The technology has been improving for the last decade, and the readout electronics have a more complex system than before. In addition, for our proposed detector also, the physics reach has extended. The radioactivity of the components is a challenge for the electronics in the detector. However, silicon circuits are pretty clean and only very small in mass. If we could identify clean packaging, large parts of the front-end electronics could be moved to the PMT bases, including local processing power. Otherwise, we need to bring cables to reach 10 m away from the signal due to the water shield all-round the detector. This might affect the pulse shape. The background rejection by the PSD method could be difficult as we need nano-second timing. The present coaxial cables are not adequate for the system as over 10m, and they have attenuation at 1GHz of 40 dB. Balanced transfer lines with flat cables might be better or Micro Coaxial Cables. One study at SJTU [156] tried Flexible Kapton boards provided by the CERN PCB workshop. The length of the cables was 1.5 m maximum, balanced with 100 Ω impedance see Figure 6.6. Beyond this length, we have to switch to a standard flat cable. The base was easy to adapt by changing one resistor value, and on the digitizer side, a pulse transformer got back the 50Ω coaxial geometry. The signal line has two wires. One is the anode connection, the other the positive HV for the divider chain on the base. The HV connection is, of course, an AC ground.

We must reduce the dissipated power per base to lower the detector's heat load with many PMT bases. This would involve increasing the resistance values in the HV divider chain. However, such a change would result in drooping voltages for high energy events, e.g., DBD, which also will be of interest. Therefore a transition to MOSFET buffered PMT bases might become inevitable.

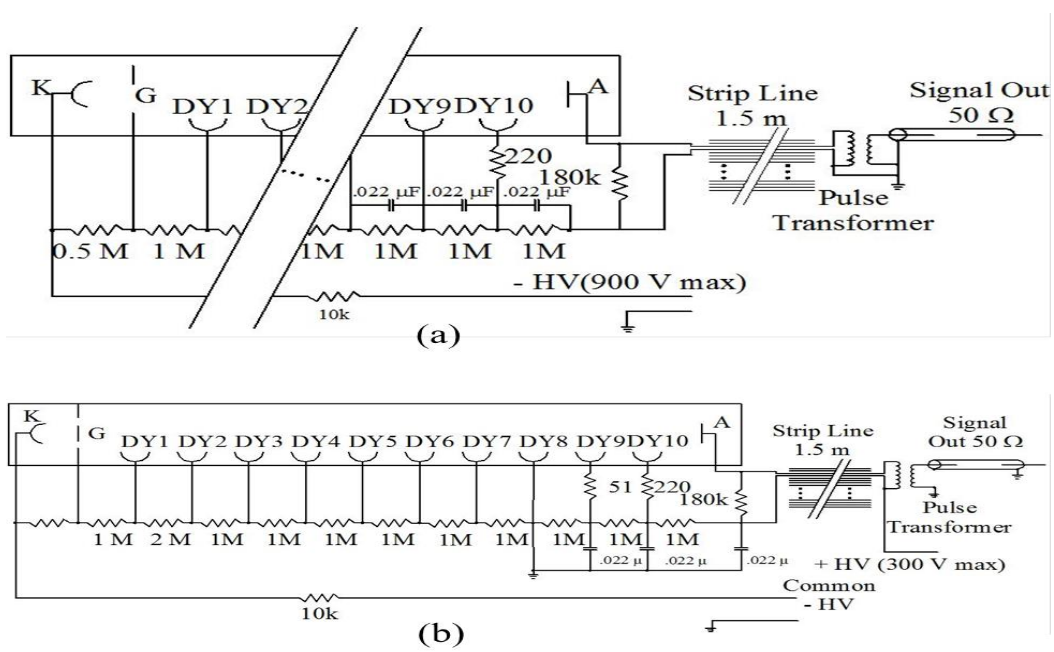

Figure 6.6 a) Proposed Circuit with Kapton Flex Line and Pulse Transformer b) Alternative PMT Connection Scheme. Figure is taken from ref. [156].

6.3.4 Field Cage

The field cage in the LXe TPC plays a vital role in shaping the drift region and has many utilities. First, we have to design the field cage with light weight to reduce the radioactive background. In addition, it should be strong enough to support the weight and buoyancy of the PMTs, and its transparency is such that PMTs can be used at the outside.

The lightest weight structure for field shaping consists of insulating rods, stretching the full height of the TPC, 4 m. For the four drift gaps, every 100 cm, the length of one drift gap, the rod is attached to the electrodes, either anode or cathode. For the first implementation of the TPC with two PMT arrays (top and bottom) and PTFE side walls, we will need to install a thin PTFE liner (1 mm) inside the shaping wire structure. The electrical field of the design should be simulated and studied in detail. Like in all earlier TPCs, the end of the field cage at the anode side will be at approximate ground potential. Therefore, one should make the connection to the ground on the outside of the detector. Thus we can monitor the current through the resistive divider forming all the intermediate potentials.

The upgraded version of the TPC needs special arrangements in the field cage as it should have many PMTs on the sidewalls of the TPC instead of PTFE.

6.4 Simulation study for Single phase (SP) and Dual-phase (DP) method

We have used Monte-Carlo simulation by using root software for the simulation study. Monte Carlo simulation is a problem-solving technique used to approximate the probability of specific outcomes by running multiple trials runs using random variables. Moreover, it obtains the statistics of the output variables of the computational system model, given the statics of the input variables. In each experiment, the value of the random input variables is sampled based on their distributions, and the output variables are calculated using a computational model. A number of experiments are carried out in this manner, and the results are to compute the statistics of the output variable.

6.4.1 With PMT R11410

1. **Geometrical consideration:** We assumed an identical large mass cylindrical detector with a mass of ~ 60 tons for the simulation study. The height and diameter of the detector is 3 meter each. The Hamamatsu R11410 3" have been

chosen for the top and bottom PMT array of the single-phase and the dual-phase detector. The effective photocathode coverage of each array is 63%. For the comparison, the geometrical consideration for SP and DP detectors has been chosen to be the same. The sides of both detectors are covered by the reflector (PFTE) with a reflectivity of 95%. There are five meshes considered in both detectors: cathode, anode, two shielding mesh, and one bottom shielding mesh below the cathode. The diameter of the wires is 50 µm, and the wire spacing in the meshes is 3 mm. Thus the optical transparency of each mesh is 95%. The anode wire and the two shielding meshes are also 3 mm apart from each other.

First, considered a photon that can generate at a random point in a cylindrical volume that is 2.8 meters in height and 2.9 meters in diameter. It means the boundary condition of generating photons is 5cm inside the actual radius of the detector and 10 cm inside from the upper and lower sides of the detector. Assuming the center of the detector is the origin, we generate 10000 events randomly in the detector system with a maximum radius of 1.45 meters and the z-position between -1.4 to +1.4 m.

2. Photon collection efficiency: The total number of photons collected in the DP and SP models is 4969 and 6053, respectively, with 3-inch PMTs. The photocathode coverage area of these PMTs is 63%. Thus, the photon collection efficiency in the SP detector is ~22% more than the DP detector.

3. Reflection on PTFE: The average number of reflections on the PTFE surface before capturing a photon by PMTs in the DP and SP detectors is approximately the same as 1.74 and 1.73, respectively.

4. Distance traveled by the photons: The absorption length of UV photons in the LXe is generally assumed to be 10 meters. Considering this, the distance covered by the photon in the detector chamber before hitting the PMT is 4.37 meters in DP and 3.85 meters in SP.

5. Direct photon hits in the PMTs: Direct hits are 1212 and 1786 in DP and SP, respectively. Therefore, 47% more photons directly hit the PMTs in the SP model than DP.

6. Total internal reflection: This phenomenon occurs in DP, where photons get reflected in the liquid and try to jump from the liquid to the gaseous phase. The simulation study shows a total of 38% of photons reflected from the liquid level. Some photons get lost due to absorption, and ~33% of reflected photons are captured by the PMTs. Figure 6.7 e shows the total number of reflections on the liquid level. In the Figure 6.7 e, “without condition” means that the total number of photons reflected on the liquid surface irrespective of lost or captured afterward, whereas “with condition” means the number of photons who get captured by PMTs after reflecting from the liquid surface with absorption length less than 10 m.

6.4.2 With PMT R12699

The efficiency of the detector increases by using R12699 Flat 2" PMT instead of R11410 PMTs. The photocathode coverage area is 72% in the top and bottom array each. For a detailed comparison see **Table 6.2**.

Table 6.2 Comparison of the DP and SP detector’s parameters with different PMTs

	DP with 3”PMT	SP with 3” PMT	DP with 2” PMT	SP with 2” PMT
Number of photon capture	49.69 %	60.53%	54.11%	65.72%
Average reflection	1.74	1.73	1.64	1.6
Average travelled distance (mm)	4373	3856	4226	3749
Direct hits	1212	1786	1385	2046
Total internal reflections*	1272	______	1317	______
Total internal reflection without condition	3798	______	3619	______

* These are the total number of photons which are captured by the PMTs after reflections on the liquid level.

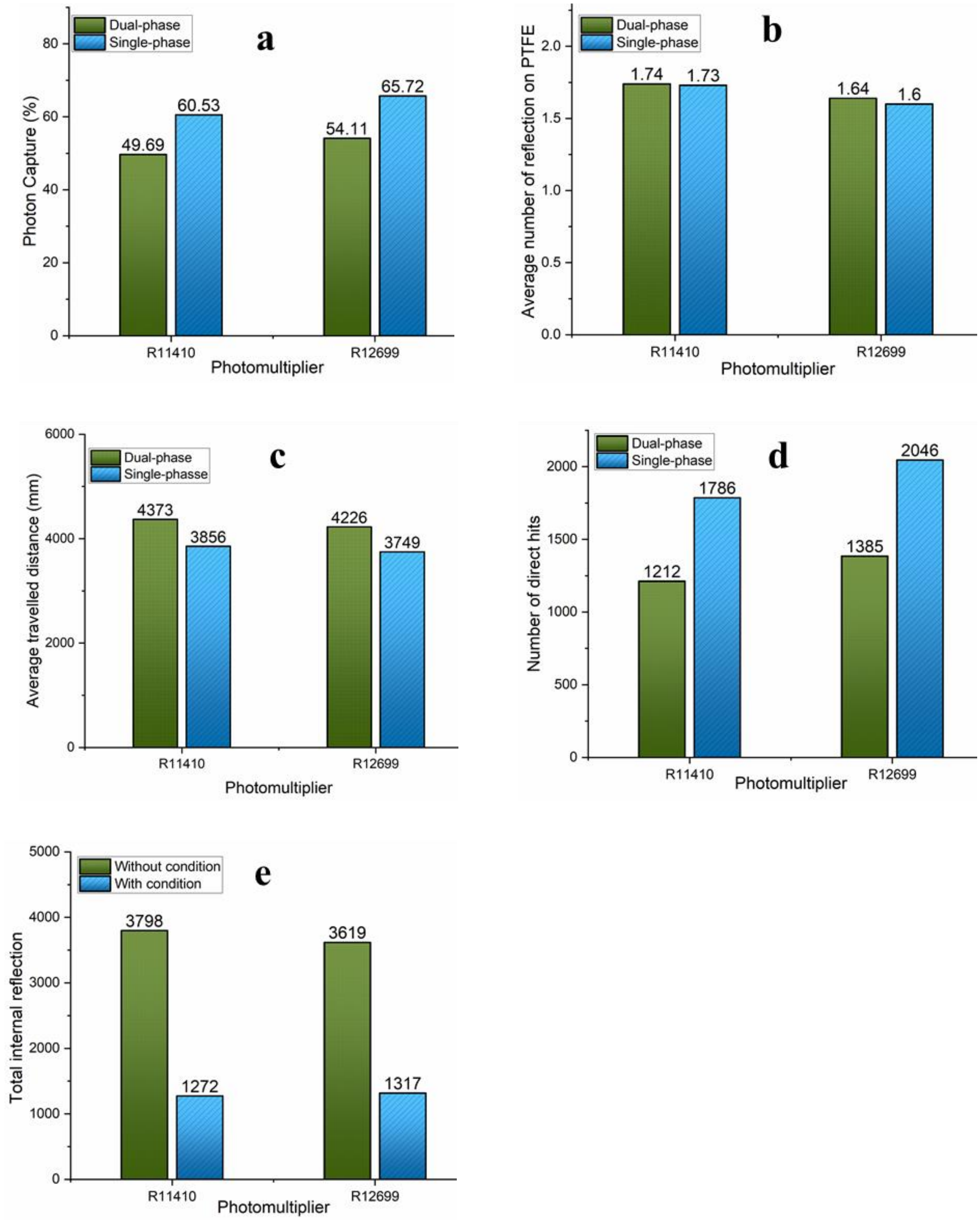

Figure 6.7 Bar graph representation of the simulation results. Comparison between single and dual-phase TPC for two type of PMTs (Hamamatsu R11410 and Hamamatsu R12699). a) Total number of photons capture by the PMTs. b) Number of reflection on PTFE surface. c) Average distance traveled by the photons. d) Number of photons directly hit the PMTs. e) Total internal reflections in dual-phase detector.

6.5 Detector with no reflections

The upgraded version of the single-phase detector would be free from reflectors, and PMTs will be used on all sides of the detector. For this, we will select the flat R12699 Hamamatsu PMTs.

In the detector having reflectors on the cylindrical wall, photons move isotropically in the detectors, and many of them hit reflector sides where some of the photons get lost, and the rest reflect into the system. These reflections continue until the photon hits any of the PMT in the top or bottom array. These reflections inside the detectors reduce the photon collection efficiency of the detector. In addition, increased path length also decreases the number of photons because of more absorption. To overcome this challenge, we are proposing a reflector-free detector. This type of detector can be called 'Quasi-background-free' if we reduce the background so that it nearly vanishes. If PSD can be established, it would be possible to minimize the background by a factor of 100. For PSD, we have to eliminate all reflection. Although the procurement of PMTs for such a large detector is a matter of concern, we can achieve it by approaching the final size of the experiment in several steps.

6.6 Requirements for the large detectors system

A large detector would need an adapted infrastructure because the xenon mass is so much larger. Most of the part we can use similar to PandaX IV experiment. Some of the parts need to be enlarging which would work well. There will be some new techniques apply for the few system such as cooling, liquid purification etc. It is note that although we need to do some engineering work too for our detector, the all part of it fully understood and available now.

6.6.1 Staged approach

The upgradation of the proposed detector which will free from reflectors and instead of reflecting material (i.e. PTFE) we will plan to use PMTs around the cylindrical wall of the detector. This requires lot of PMTs. The production of such a huge amount of PMTs including spares will take some time, several years in the best scenario. We might experience a similar delay procuring the full amount of xenon. Until now the required xenon mass was in the range of the 'on-stock' gas. Now we move to a demand exceeding the current worldwide yearly production. With some investment gas suppliers would be able to enhance their production with time. Still we would look at a development time of many years.

It would be better to think towards a staged approach for a large mass detector. Most of the infrastructure will be dimensioned for the final detector size; this implies the vessel, the shielding tank, the cooling, the purification system, and the xenon handling and storage facility. Initially, we would insert only two drift gaps with the full diameter, i.e. we fill the detector with about a half of the full xenon mass. The detector will be read by ~2000 tubes on the two face plates with PTFE panels covering the side walls.

Thus our detector would look like an oversized PandaX II, but in single phase technology. When more tubes and more xenon become available the detector will be upgraded increasing its mass and replacing the PTFE reflectors with PMTs. We also have to add more read-out modules and cabling for the side PMTs. Finally, the detector will reach its full functionality.
The masses and the number of PMTs for the different stages are given in the following **Table 6.3**

Table 6.3 Requirement of PMTs for the large mass LXe detector

Detector	**Total mass**	**Active mass**	**Fiducial mass**	**Side walls**	**Number of PMTs 2" R12699**	**Number of PMTs 3" R11410**
2 drift gap or 4 drift gap	~78 ton	60 ton	~53 ton	PTFE	~3020	1914
				PMT	~12000	6714

First we can plan to setup 20 ton of xenon in a 60 ton system. Later, we will go with larger mass according to availability of xenon and electronic components such as PMTs. In this way we can start our detector soon to study the physics. This would be much more difficult in DP detector because of liquid level control.

6.6.2 Recirculation – purification

The LXe detectors should have radio-pure materials and a highly cleaned assembly. Earlier times, detectors needed to be vacuum baked for cleaning. But now a continuous circulation system is used to clean the xenon and recirculate it during the operation. There is a gas handling system for recirculation and purification of the xenon. For the small detector system in SJTU [157], we have also adopted the gas handling system which provides continuous recirculation and purification of the xenon. The Figure 6.8 shows the gas handling system. LXe heated, evaporated, and by using a diaphragm pump throughout a getter with 5 SLPM (standard liter per minute) gas flow. This is for the small detector, but for the larger one we need a high gas flow getter like PandaX-4T. PandaX-4T used two hot SAES getters through two separate circulation loops with stable flow rates of about 80 and 30 SLPM respectively [123].

The maximum drift time is 500µsec for 100cm of drift gap. The electron attachment to impurities is governed by the concentration of the electro-negative impurities which scales like a volume. After an initial cleaning, the concentration depends on the impurities entering the system. Leaks in the detector system scale with the length of seals and outgassing scales with the surface area. It is relatively easier to purify the large size detector since the maximum drift length is reduced to 1/4. Although, the purity will only get better very slowly. The lifetime of the ionization electron only needs to be large relative to 500 µsec rather than 2 msec of a dual-phase detector of similar mass. So, the chemical purity can be significantly relaxed. These considerations do not hold for radioactive substances such as ^{85}Kr and radon. For these radio impurities, a fixed background rate goal sets a concentration requirement proportional to 1/volume, so the removal of these gets tougher.

Apart from the gaseous purification method, the novel LXe liquid purification and recirculation method are being used by the XENON nT [114]. According to first unconfirmed comments the cleaning of the LXe is considerably faster than the gas purification. We have to wait for the final results from XENON nT, to select the best method.

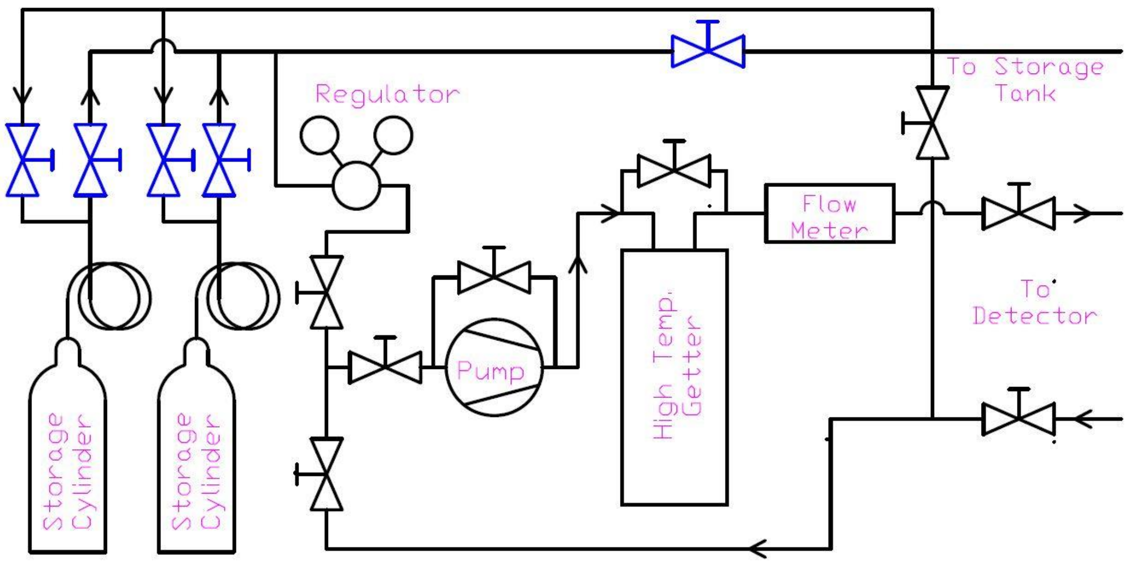

Figure 6.8 Schematics of the gas handling and supply system. The figure is taken from ref. [157].

6.6.3 Cooling

6.6.3.1 Remote Cooling

The cooling system including the Pulse Tube Refrigerator (PTR) is made from unknown raw materials. It is impossible to control the radioactive materials in all its parts. The only way to reduce all these sources of background is to move the cooling system to the outside of the shield. This cooling method was developed for XENON100. Background reduction is possible when cooling system at a distance of more than 1 m, e.g. for XENON100 and PandaX I and II. For XENON 1T it was nearly 10 m because of the 5 m thick water shield.

The PTR with its cold finger is located in a small vessel, connected to the gas volume above the liquid in the detector with a thermally insulated steel tube. The Xe gas from the detector thus reaches the cold finger and is cooled to form droplets on the cold finger. The droplets are collected with a funnel and guided with a small diameter tube through the gas tube back to the top of the detector. The liquid is propelled by gravity since the gas connection tube is mounted under an angle of 5° to the horizontal. In the detector the liquid from the cooling unit just drips back into the liquid volume. The whole process is called 'remote cooling'.

From the first tests this cooling method performed very well with the requested long time stability.

6.6.3.2 Indirect Cooling with a PTR

The PTR is a cryo-cooler used for most of the LXe detectors. It was developed by Tom Haruyama of KEK for MEG [158]. However, the invention of PTR was long before that but used for the lower temperatures. Haruyama optimized it for LXe temperatures and transferred the design to the Iwatani company. One of the first PTRs with 100W power with a 3.5 kW He- compressor was used for the XENON10 experiment [112]. Iwatani then marketed a full range of PTRs between 24 W and 150 W at -100°C. The XENON100 experiment [158] used a PC150 with a 7 kW Linde air-cooled He-compressor. In this combination the actual cooling power was close to 200 W.

The PTR cold head is connected to a cylindrical copper cold finger that reaches into the inner detector vessel. Thus one can change or repair the PTR unit without opening the detector volume. But most of all, it keeps some 'dirty' instrumentation in the thermal vacuum, e.g. temperature sensors and cables. This so-called indirect cooling method was first used for XENON10 and afterwards in all XENON and PandaX detectors.

Note that the PTR is always cooling with its full power. To reduce the cooling power and thus adjust the temperature of the detector a resistive heater is mounted on top of the cold finger. The heating power to counteract an excessive cooling by the PTR is controlled by the temperature with a PID controller.

6.6.3.3 Emergency Cooling

Liquid nitrogen (LN2) in a cooling coil is used for emergency cooling, for example in case of a power failure [112]. This is an entirely separated unit which is activated when the pressure on top of the liquid rises beyond a set point. Once the pressure returns below a second, lower set point the flow of nitrogen flow is stopped again. Thus, the detector is kept within a safe temperature and pressure range as long as LN2 is available, i.e. at least 24 hours on a standard LN2 dewar. The essential units, i.e. pressure sensor, solenoid valve, and pressure controller are powered by an uninterruptible power source (UPS).

6.6.3.4 Cooling a Very Large LXe detector

The very large LXe detector proposed here is considerably larger than any other DM detector deployed so far. Although we can try to improve the thermal insulation and reduce the heat losses through vessel connections and electrical cables, the heat load will be beyond the cooling power of a standard PTR. In a recent survey of cooling methods, we identified LN2 driven cooling as the best solution for cooling above 2 kW power.

The proposed solution would leave most of the cooling system untouched, but would replace the PTR with a copper rod ending in a LN2 reservoir. The copper rod is dimensioned in diameter such that at the maximum required cooling power the temperature at the end of the cold finger is -100° C. The copper rod therefore just shifts the temperature. Again the cooling unit operates constantly at full power. A heater module in the cold finger counteracts again the excessive cooling power. The heater power is controlled by the same PID controller according to the temperature at the cold finger.

Such a cooling system was originally built at CAL around 2005. It was used for a small detector within the XENON experimental development program. Finally, even the recent single-phase tests at Columbia were executed with the same system. The cooling system is described in [7]. The LN2 cooler can easily replace the PTR module as shown in the comparison of the two modules in Figure 6.9.

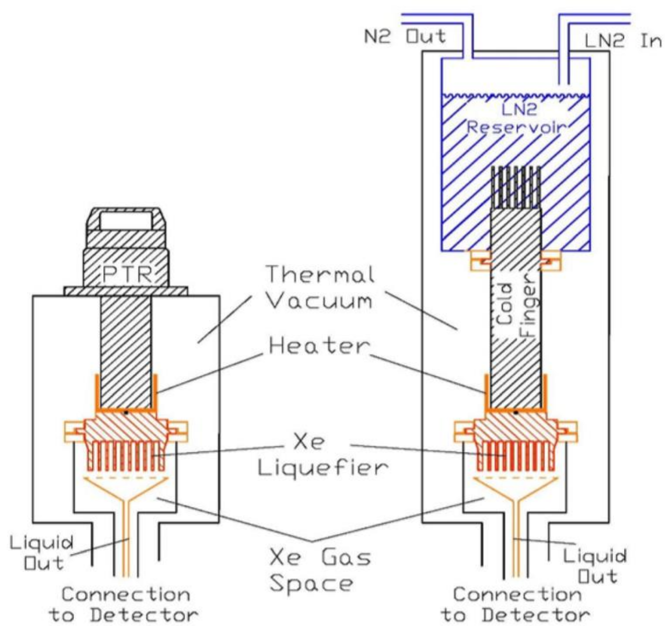

Figure 6.9 Schematics of cold finger. Figure is taken from ref. [7].

6.6.4 Modular cooling system

The cooling of a LXe detector is a rather complex system. An integral design of all the various functions does not lend itself for easy modifications when the need arises. Therefore starting with PandaX I all PandaX detectors were instrumented with a modular cooling design. All the functions like heat exchanger, emergency cooling, and PTR were set up in separate vessels connected with on large tube for xenon gas and the cooled liquid in the center. All the various modules connect to this tube. It resembles the bus structure in a computer which connects to all modules. It was therefore named the 'Cooling Bus' [159]. Figure 6.10 shows the cooling bus used for PandaX I and II.

Figure 6.10 Cooling bus system for PandaX detector. Figure is taken from ref. [159].

6.6.5 Active internal shield

Liquid xenon fills the space all around the TPC separated by the PTFE panels from the active volume. The contained xenon can be used as an active veto against some background. This active veto is observed by the veto PMTs which are installed on outside of the active volume. XENON100 was the first LXe DM detector with an active veto shield. The shield was also extended above the top PMT and below the active volume.

It is sometimes suggested that the instrumentation of the active volume can be replaced by a larger x - y fiducial cut. However, the two veto regions are not exactly the same. Particles originating in the vessels, inner or outer, will interact in the active shield with a high probability. They are definitely background radiation and might produce another interaction in the active volume. If the shield is passive, the second interaction in the active volume might be interpreted as the only part of the event. It might become a false positive DM candidate if the NR - ER discrimination is not accurate in this event.

6.6.6 Shielding with a water shield

A water tank with at least 5 m of water in all directions shields the cryostats of XMASS, XENON 1T + nT, LUX/LZ, and PandaX IV against radioactivity from the rock and concrete around the labs. When the water in the shield is instrumented with PMTs, it acts as a water Cerenkov detector and tags muons and cosmic rays passing in the vicinity of the detector. Associated events in the LXe detector can be vetoed [111] with an overall efficiency of 50% [109]. Even higher efficiencies can be observed when the water is replaced by liquid scintillator.

The importance of the instrumentation in the water shield depends on the depth of the lab. The LNGS with XENON is already very deep, but still an active shield has an advantage. The CJPL on the other hand is already so deep that the instrumentation is not necessarily required.

A 5 m thick water shield reduces the background better than the passive lead/poly shield used for former detectors. But one must watch the radon emanated from the tank walls. Once entered into the water the radon also gets close to the detector and there is not much attenuation for decay products.

6.6.7 ^{85}Kr removal with distillation column

Commercial xenon contains a small amount (0.1–1 ppm) of krypton, which has a radioactive isotope, ^{85}Kr (half-life of 10.76 years) in a concentration of about 10^{-11} in natural krypton. The concentration sounds very small; still it is a significant background in a large DM experiment. The XMASS group developed a distillation column to remove this admixture of krypton. The same column was used for the XENON100 experiment. For the larger experiments XENON 1T, XENON nT, and PandaX, new columns with higher capacity were developed by the groups. The original design parameter was a krypton reduction by a factor 1000, but finally much better background reductions are achieved. The XMASS group achieved a

Kr/Xe value of 2.7 ppt [77] with a flow rate of 4.7 kg/h. 1.2 tons of xenon was processed in 10 days before it was introduced into the detector. The krypton concentration was measured by atmospheric pressure ionization mass spectroscopy.

For krypton removal, we will probably need a larger column. But in a tight set up all the contaminants are present from the initial filling. Thus, for a certain concentration, the column does not have to be any larger as long as the clean-up time is no issue. Since the xenon filling will be acquired over several years, we can run the distillation column already while the construction of the detector is on-going, i.e. without a delay to the experiment even with a modest column size.

Continuous online use of the distillation column is also possible. But one has to consider that the column removes the krypton together with 1 - 2 % of xenon.

6.6.8 Radon removal

As the sensitivities of the DM detectors are increased from one generation to the next different background sources become important and must be reduced. In XENON10 and PandaX I the radioactivity from construction material was dominant. With these reduced sufficiently in XENON100 and PandaX II ^{85}Kr became important. With the successful use of the krypton distillation for XENON 1T and nT and PandaX IV radon becomes dominant. Like krypton radon is a noble gas which mixes well with xenon and homogeneously fills all the active volume. A fiducial cut cannot be used to reduce this background.

The main source of this background is ^{222}Rn with a half-life of 3.8 days. It emanates from the detector material and the gas system. Figure 6.11 shows the decay chain of Rn-222. Lead-210 (^{210}Pb) is the isotope with the longest half-life (22 years) in the decay chain. Among radon daughters down to ^{210}Pb, the main source of background comes from the beta decay of Lead-214 (^{214}Pb) to the ground state of Bismuth-214 (^{214}Bi). In XENON-100, gas purification system was used with distillation column for radon removal. The radon reduction capability of the distillation column was determined to be $R > 27$ [160]. For XENON1T the radon removal technique was improved to reach an estimated value of radon removal down to 10 µBq/kg, which is ~5 times better than XENON-100.

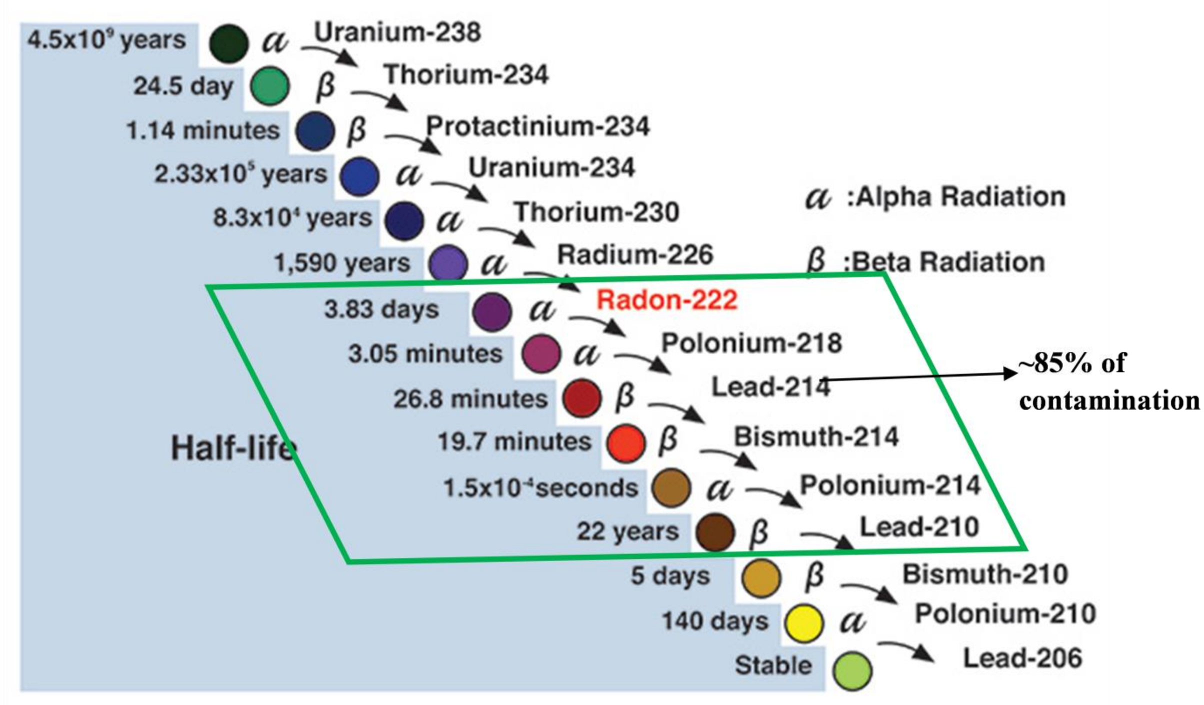

Figure 6.11 The decay chain of radon-222. Figure is taken from ref. [161]

7 Physics Reach of a Large, Low Energy Detector

The various dark matter experiments have been continuously employed in the search of WIMPs for more than 30 years. During this journey, there have been a lot of changes in the techniques and methods, by which we have successfully explored the sensitivity of the DM detectors. The LXe detectors are approaching the neutrino floor which is an irreducible background but still there is no WIMP particle found yet. As the size of the detector is increasing, the probability of finding WIMPs increases. It is right that a large target mass provides better sensitivity but we have foreseen that the hypothesis of WIMPs might be fallacious. Then our detector can also search other DM particles and explore other physics.

Recently, there is a heightened interest in high energy events, e.g., from the neutrinoless double beta decay of ^{136}Xe with a Q-value of 2458 keV. Since the natural abundance of ^{136}Xe is 8.9%, similar to present LXe DM detectors, the future LXe DM detectors will also contain a large amount of this isotope. Even at such high energies, the two electrons will form a single-site event, and the length of the track will be much smaller than the spatial resolution of the TPC readout. Due to the reduced S2 gain, the signals can now all be within the limits of the electronics with no saturation. The remaining effects from PMT saturation can easily be corrected.

There are other physics searches such as axions, neutrinos etc. A plenty of neutrino detectors have been operating for many years, but the present energy threshold value for these detectors is high enough and cannot reach for very low energy neutrinos range. Super-k has an energy threshold value is greater than 250 keV. The proposed detector will be low energy LXe detector which can have an energy threshold of less than 50 keV. Therefore, it will be able to find out the low energy neutrinos in the less than 50 keV scale.

7.1 Double Beta Decay

Double beta decay (2νββ) is a nuclear process. The normal β decay is prohibited by energy conservation. But two simultaneous decays would be allowed. The nucleus decays by increasing the proton number by 2 and keep the same nucleon number as the initial nucleus. Two electrons and antineutrinos are emitted. This can be written as

$$\boldsymbol{(Z, A) \rightarrow (Z + 2, A) + 2e^- + 2\overline{\nu e}} \qquad \textbf{(1)}$$

Where Z is the proton number (atomic mass) and A represents nucleon number (atomic mass).

The double beta decay is observed in two types of the decay process, first one is a normal, second-order process like equation 1, where two electrons are emitted with two-electron antineutrinos. A second one is a hypothetical decay where electrons would be emitted with no neutrinos. This would imply that the neutrino is its own antiparticle in these cases. This process is known as neutrinoless double beta decay (0νββ). It shows lepton number violation and points towards Majorana neutrinos [162].
This process can be written as,

$$(\boldsymbol{Z}, \boldsymbol{A}) \rightarrow (\boldsymbol{Z}+\mathbf{2}, \boldsymbol{A})+\mathbf{2}\boldsymbol{e}^{-} \qquad \textbf{(2)}$$

These two processes can be understood by the Feynman diagrams in Figure 7.1.

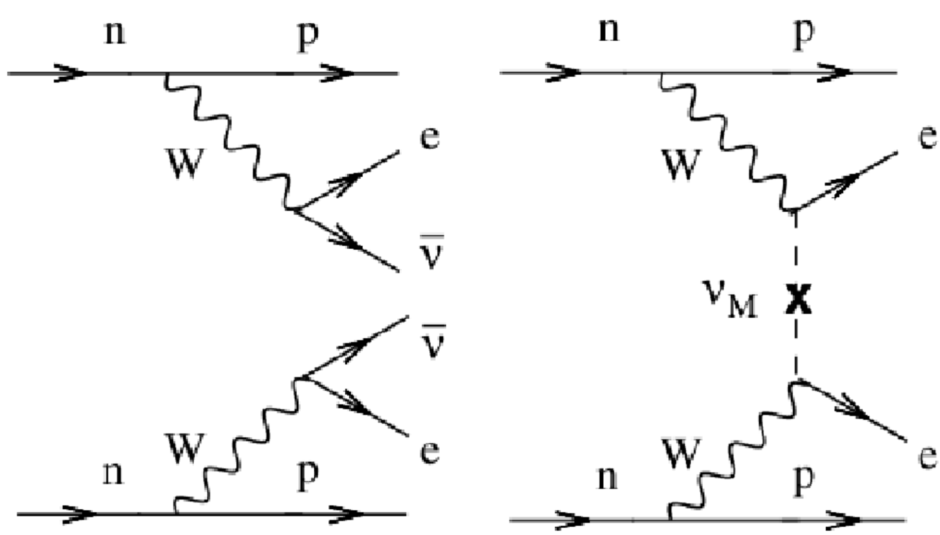

Figure 7.1 Left, 2 neutrinos double-beta; right, neutrinoless double beta decay. Figure is taken from ref. [162].

7.1.1 Large scale isotope separation with Source on-off Experiments for DBD

We can adopt an original proposal [11] given by Professor Yoichiro Suzuki for XMASS in 2000. With isotope separation natural Xe can be divided nearly into two halfs, the isotopes above and below 131.5. The lower sample contains nearly all odd isotopes, whereas nearly everything above 131.5 is even. Odd isotopes are used for detection of solar neutrinos or for spin dependent DM search. On the other hand even isotopes are used for double beta decay and spin independent DM. We have two choices: If we have 100 ton of xenon we can use two 50 ton detectors in the same shield simultaneously for the two samples. Or we can fill a single 50 ton detector with the two samples sequentially.

Double beta decay occurs in just a few naturally occurring radioactive isotopes. For xenon it is just ^{136}Xe which can have this decay mode. As the natural abundance of ^{136}Xe is 8.9%, for 100 ton of xenon we shall have 8.9 ton of ^{136}Xe in the 'even' sample, and nothing in the other one. Both samples will have the same background since the same shield is used. Therefore we can subtract the background sample (<131.5) from the signal sample (>131.5). This will enhance the sensitivity to DBD tremendously. In comparison, the final experiment with the PandaX III detector was proposed to have 1 ton of 90 % enriched ^{136}Xe. This makes 900 kg with no background subtraction possible.

SP detector also give the feasibility to fill the detector with less liquid as we can run with 25 ton each, instead of 50 ton.

Since nearly all the odd nuclei are in the sample with lower isotopes one can use this measurement to differentiate between spin-dependent and spin-independent Wimp interactions. Spin-independent interactions, of course, would occur in both samples with the same rate.

7.1.2 Present DBD experiments:

The PandaX-III experiment uses high-pressure TPCs to search for 0vbb of ^{136}Xe, with high energy resolution and sensitivity at the CJPL-II. The prototype of the detector has a mass of 20kg of ^{136}Xe (90 % enriched). The detector was run for different calibration sources [163]. Figure 7.2 shows the detector response to ^{241}Am gamma source in 5 bar Xe (99%)+(1%) TMA, the energy spectrum originates from ^{241}Am and its daughter ^{237}Np, the energy resolution is 14.1% FWHM at the 59.5 keV peak. The first phase of the detector will contain 200kg of ^{136}Xe has been under commissioning. The half-life sensitivity to $0\nu\beta\beta$ is expected to be about 10^{26} years for an exposure of 3 years [164].

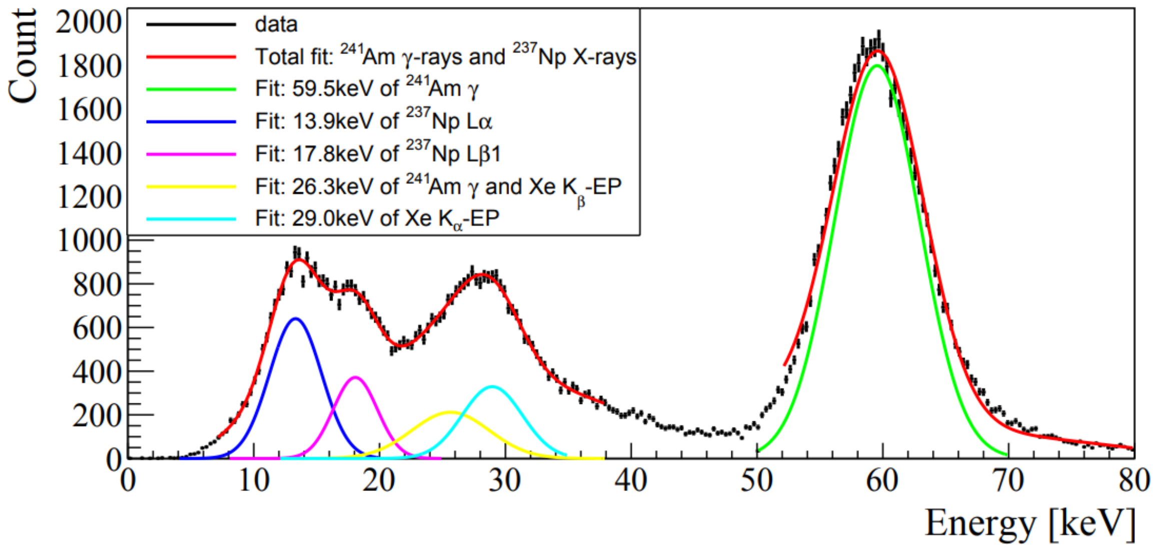

Figure 7.2 The energy spectrum of the 241Am events in 5 bar Xe-(1%) TMA gas mixture with all selection criteria applied. The figure is taken from ref. [163].

NEXT (Neutrino Experiment with a Xenon TPC) is a 0νββ experiment operated at the Canfranc Underground Laboratory (LSC). It is the high pressure xenon gas TPC. The NEXT-HD module with a mass in the ton range will be able to improve by more than one order of magnitude the current limits in $T_{1/2}^{0\nu}$, thus exceeding $T_{1/2}^{0\nu} > 10^{27}$ yr. For a complete overview of the detector consider [165].

AXEL is a high-pressure TPC for 0νββ decay search. The project is in the R&D phase. The detector consists of a large mass extendable to 1-ton enriched high-pressure ^{136}Xe gas, good energy resolution (aiming 0.5 % FWHM at 2.48 MeV which is a Q value of ^{136}Xe). The Figure 7.3 shows the mechanism of the AXEL detector in which ionized electrons drift toward the Electroluminescence Collection Cell (ELCC) plane and produce light signals[166].

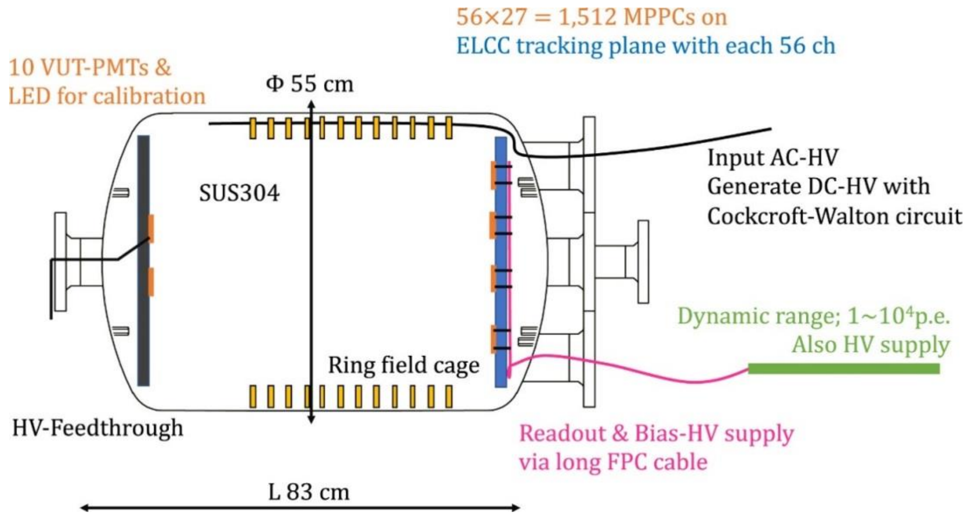

Figure 7.3 Overview of AXEL detector. The figure is taken from ref. [166].

7.1.3 Other DBD experiment

The MAJORANA collaboration constructed the DEMONSTRATOR, an array of germanium detectors, to search for neutrinoless double-beta decay of germanium-76. For the Feynman diagram see Figure 7.4. It will contain 40 kg of germanium; up to 30 kg will be enriched to 86% in ^{76}Ge. The goal of the MARJONA collaboration is to determine whether a future 1-ton can achieve a background goal of one count per ton-year in a 4-keV region of interest around the ^{76}Ge 0νββ Q-value at 2039 keV. According to the published result [162], the lower limit on the ^{76}Ge 0vbb half-life of 2.7 × 10^{25} yr.

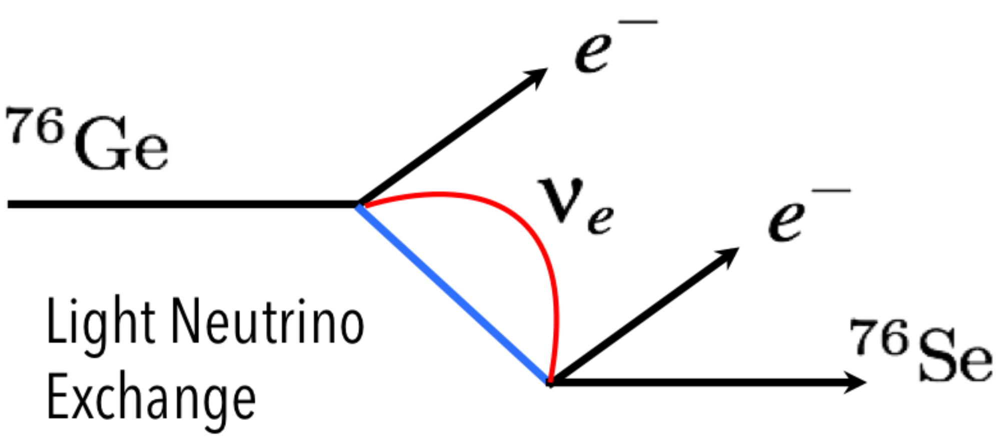

Figure 7.4 The Feynman diagram of 0vbb for ^{76}Ge. Figure is taken from ref. [167].

7.2 Axions

Although the axions have not been found yet, it is predicted that if they exist then they must be produced in an extreme environment like a supernova.

The axion is determined by the axion- photon coupling and the axion-electron coupling. The first one is looking for the axion as a product of the Primakoff effect. The Primakoff effect is the process of theoretical coupling between axions and photons. In general, axions are not supposed to interact with photons. The effect predicted that, if photons are subjected to intense magnetic fields i.e. in the stellar cores, they transform into axions. When a star explodes in a supernova, it should eject the axions out into the universe. If axions run into a magnetic field, they should turn back into photons with some detectable energy.

XMASS detector examined the axion-electron coupling by which solar axions were produced. The model-independent limit on the coupling for mass less than 1 keV is 5.4×10^{-11} (90% C.L.) for the axion mass range 10 – 40 keV [168].

The recent results from **XENON 1T** show a surprising excess of events in their ER data [2.41]. The source of this unexpected rate of events observed has not been confirmed. The data of XENON1T were compared to known backgrounds, a surprising excess of 53 events over an expected 232 events was observed. This excess of events could be caused by the presence of tiny amounts of tritium as it emits electrons with the same energy. The second interpretation is that these events are solar axions as the energy spectra of these are similar to the axions produced in the Sun. Yet another possibility would be that the excess is due to neutrinos having a magnetic moment larger than the value in the SM model. Out of these three explanations the observed excess is most consistent with a solar axion signal. According to data observation, the solar axion hypothesis has a significance of 3.5 sigmas. The significance of both the tritium and neutrino magnetic moment hypotheses together corresponds to 3.2 sigmas. But, both interpretations are also consistent with the data.

We have to wait for further results on the axion, but one can assume that with a large mass LXe detector there will be a good chance to explore axion region.

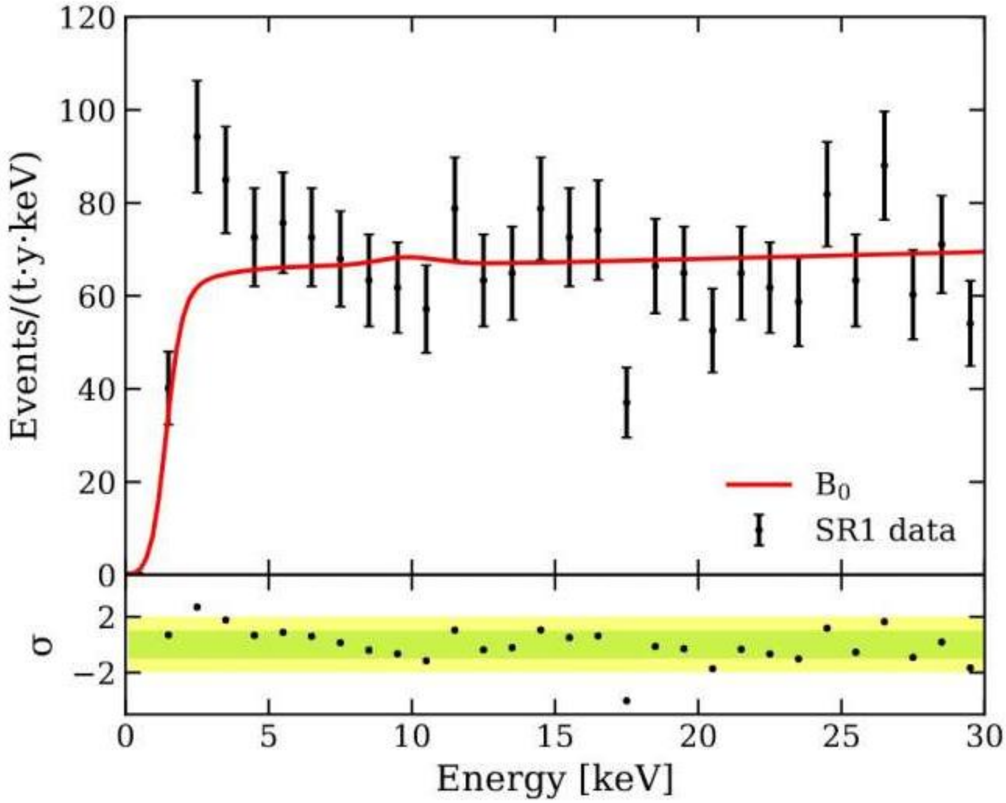

Figure 7.5 The excess observed in XENON1T in the electronic recoil background at low energies, compared to the level expected from known backgrounds indicated as the red line. Figure is taken from ref. [10].

7.3 124-Xe double electron capture

Two-neutrino double electron capture (2νECEC) is a second-order weak process in which two orbital electrons are simultaneously captured by a proton-rich nucleus and provides the new channel to measure the neutrinoless mode of the decay analogous to DBD. In this process, the X-rays and auger electrons are emitted from the de-excitation of the daughter atom. The decays of the 2νECEC process have been seen for the isotopes ^{78}Kr, ^{130}Ba, and ^{124}Xe.
The process of 2νECEC on ^{124}Xe is

$$\mathbf{{}^{124}Xe+2e^{-}\rightarrow{}^{124}Te+2\nu e}$$

Here, two K-shell electrons in the ^{124}Xe atom are captured simultaneously, a daughter atom of ^{124}Te is formed with two vacancies in the K-shell and de-excites by emitting atomic X-rays and/or Auger electrons.

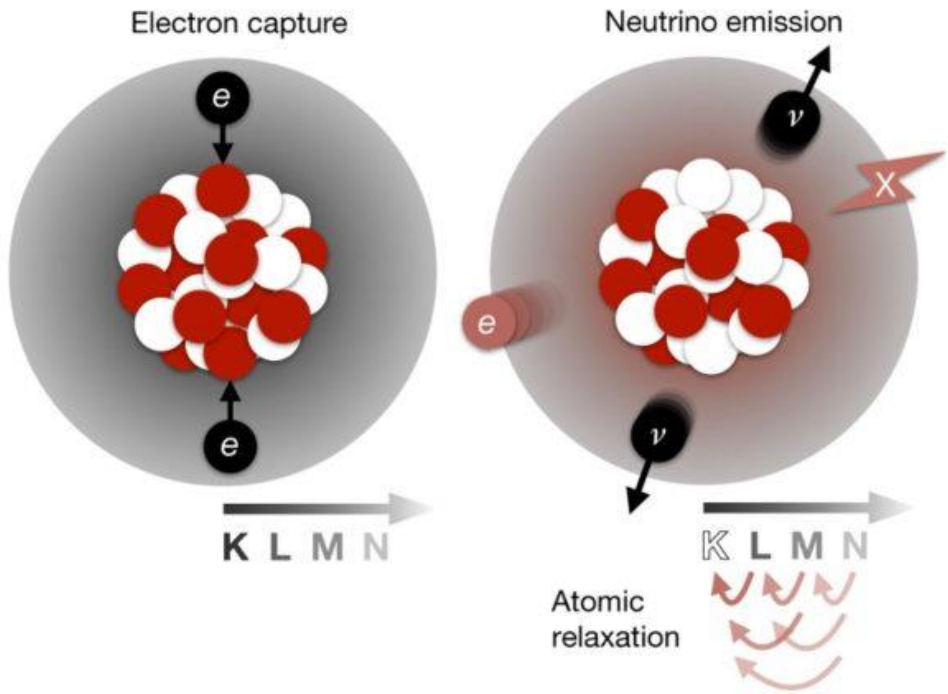

Figure 7.6 Two-neutrino double electron capture. The figure is taken from ref. [169].

The NEXT experiment examined the 124-Xe 2νECEC process by using the background data (125.9 days) of the NEXT-White experiment and simulated signal data [170]. It is the second phase of the NEXT program deploying 5 kg of xenon gas. The total background rate of 24.7 μHz (780 counts/year) is measured in NEXT-White. By using this background rate for the NEXT-100 experiment, the predicted sensitivity to the 2νECEC half-life of 6×10^{22} y with 1Kg of 124-Xe for a 5-year run.

XMASS detector also searched for 2νECEC on 124Xe [171], but no significant excess over the expected background was found. The lower limit on 124Xe and 126Xe 2νECEC are half-life values of 4.7×10^{21} years and 4.3×10^{21} years at 90% CL, respectively.
XENON observation of 2νECEC in 124 Xe with XENON1T detector found the half-life 1.8×10^{22} [169] and the significance of the signal is 4.4 sigma.

The double electron capture of ^{124}Xe only occurs with a single isotope. The technique of isotope separation can use for 2νECEC detection in large LXe detector. Naturally here the 'signal sample' would be the one with isotopes less than 131.5. Again with the background subtraction technique would improve the sensitivity of the experiment by a large margin in our detector.

7.4 Neutrinos

The neutrino is a particle postulated by W. Pauli in 1930. They are one of the most abundant particles in the Universe. As they have no electric charge they cannot interact via electromagnetic interactions. Since they are leptons they cannot couple via strong forces and only interact via the weak force. According to the Standard Model, neutrinos have been considered as massless particles, but there are experimental proofs that indicate the existence of neutrinos with a finite mass. Therefore, a search for a non-zero mass of neutrinos comes into the picture. Neutrino oscillation is one of the methods for the non-zero-mass neutrino search. There are three flavors, electron neutrino, muon neutrino and tau neutrino, and their antiparticles.

7.4.1 Atmospheric neutrinos

Atmospheric neutrinos are typically produced around 15 kilometers above Earth's surface. They form when a cosmic ray interacts with Earth's atmosphere. These particles generally are protons, though they can also be helium or heavier nuclei. When they strike an atomic nucleus in our atmosphere, there is a cascade of particles. These are short-lived particles, primarily pions, made of two quarks. They are unstable, so they rapidly decay into a muon (μ^+ or μ^-) and a muon-neutrino (ν_μ) or muon anti-neutrino ($\bar{\nu}_\mu$). The muon is also an unstable particle, but it further decays. For an instance, μ+ decays into positron, electron neutrino and muon antineutrino. Therefore, most of the atmospheric neutrinos are muon neutrinos. This we can easily understand by the left side of Figure 7.7 from [172]. The Super-Kamiokande experiment [173] in Japan found that many fewer muon neutrinos were arriving than predicted. Muon neutrinos oscillated into different types of neutrinos, causing a slight excess of electron neutrinos and a deficit of muon neutrinos. However, it took the enormous Super-Kamiokande detector, filled with 50,000 tons of ultrapure water, to gather sufficient data, 5,400 atmospheric neutrino interactions.

To calculate the flux ratio and zenith angle of the atmospheric neutrinos proves the existence of neutrinos oscillation[172]. This flux ratio increases with energy above 1 GeV because muons begin to reach the ground before decay. The results of three independent studies [174-176] are shown on the right side of Figure 7.7. The first detections of atmospheric neutrinos were made in 1965 in deep mines in South Africa [177] and the Kolar Gold Fields in India [178].

In the Kolar Gold fields experiment, they have used two neutrino telescopes to detect muon produced in the interaction of neutrinos. There is 95% of muon generated from the neutrino interactions. Thus, on taking this into account, our detector would perform better in eliminating muon flux from the outer surrounding because of the deepest underground laboratory. Therefore, this detector would detect muons generated from the atmospheric neutrino interactions inside the detector. These neutrinos produce from the cosmic rays. For the background, we can adopt the isotope separation technique for the DBD with a switch on-off method for the background where we can switch off the background by running without ^{136}Xe.

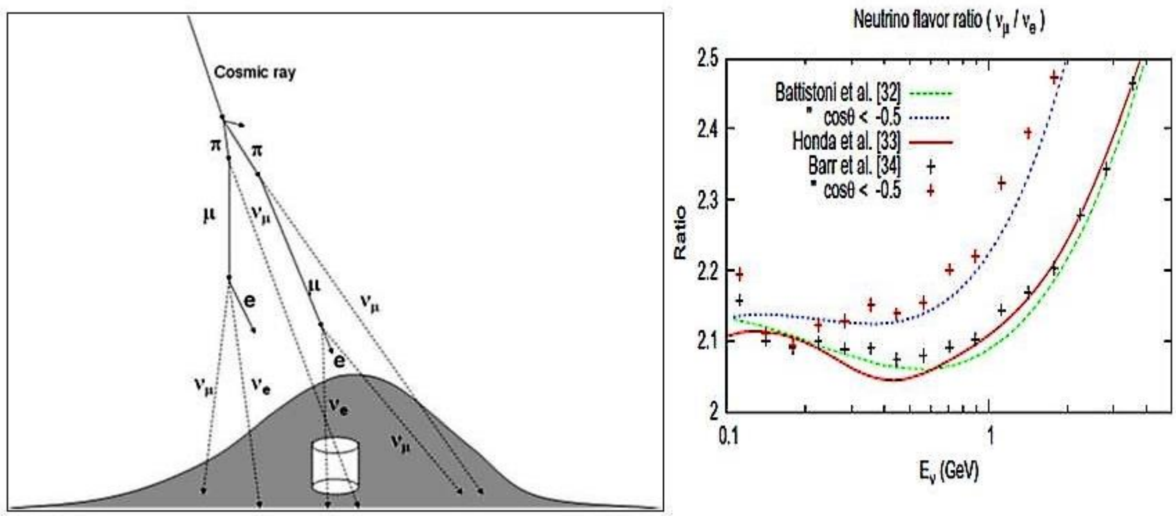

Figure 7.7 Left, Production of neutrinos by cosmic-ray interactions with the air nucleus in the atmosphere[172]. The typical height of the neutrino production is 15 km above the ground. Right, Comparison of the flavor ratio r from three calculations [174-176]. This figure is taken from ref. [179].

7.4.2 Solar Neutrinos

The discovery of neutrino oscillation indicates the presence of non-zero-mass neutrinos [180]. Therefore, the quest of finding solar neutrinos came into existence. The search for solar neutrinos existed before but the experiments were very difficult due to the small energies.

Solar neutrinos are the product of nuclear fusion reactions in the Sun. Therefore, largest portion of neutrino's flux in Earth comes from Sun. For luminosity of the Sun, protons convert in the alpha particle, positron and neutrinos with 25 MeV of thermal energy. This process fulfills the nuclear fusion reaction and can be written as:

$$4p \rightarrow \alpha + 2e^{+} + 2\nu_e + 25\text{MeV}$$

Most of the solar neutrinos generated by the proton-proton (pp) reaction but have energy (0.42 MeV) below the detection threshold for most of the solar neutrino experiments. There are other reactions also produce solar neutrinos such as Beryllim-7 (^{7}Be) captures a proton to form Boron-8 (^{8}B) and then ^{8}B decay into Beryllium-7 (^{7}Be) and finally produce 2-alpha particles.

$$^{7}Be + p \rightarrow {}^{8}B + \gamma$$
$$^{8}B \rightarrow {}^{8}Be^{*} + e^{+} + \nu_e$$
$$^{8}Be^{*} \rightarrow 2\alpha$$

The neutrinos produce in this process have a maximum energy of less than 15 MeV. However this is a rare event, Super-K and SNO experiments are sensitive to these high energy neutrinos.

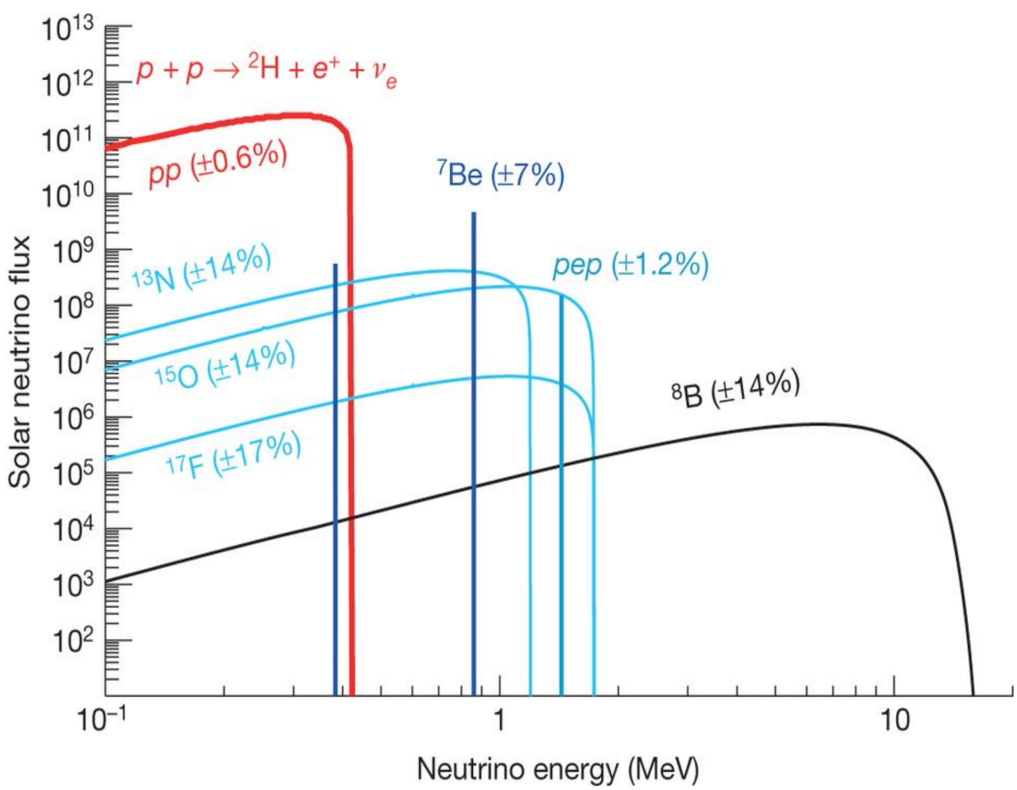

Figure 7.8 Solar neutrino flux. Figure is taken from ref. [181].

7.4.3 Supernova neutrinos

When the core of the massive stars reaches ~1.5 times the mass of the sun, the temperature rises to over 100 billion degrees, and then it collapses due to its gravity and forms a neutron star. The explosion of the massive star is generally known as supernova. All the binding energy of the star is in the form of neutrinos. The energy range is nearly 10 - 30 MeV. These neutrinos come in all flavors and are emitted over a timescale of several tens of seconds. The multi-ton detectors will be able to capture many CNNS events in the case of galactic supernovae [182]. Moreover, the DM experiments may observe the pre-supernova neutrinos too [183].

The proposed multi-ton detector can be helpful for the detection of a large number of coherent neutrino-nucleus scattering events, which is sensitive towards all types of neutrinos. Thus, the detector will be used as a neutrino observatory to detect different types of neutrinos and used to study a supernova if any of them will occur in the future. Like the other DM experiment, the detector can reduce the background from the observation of pre-supernova [183] and predict the future one. Moreover, this detector will have a low energy threshold, providing excellent sensitivity for the supernova neutrinos.

7.4.4 Extra-Terrestrial Neutrinos

The extra-terrestrial neutrinos are those who come from outside the solar system. The first observation of these kinds of neutrinos was found in the IceCube neutrino observatory in 1987. The data collected by the detector between 2010-12, showed 28 neutrino candidates with high energy neutrino flux. The events found have energies between 30 to 1200 TeV [184].

7.4.5 Neutrinos experiments

The ICARUS T600 neutrino detector measures 65 feet long and is filled with Liquid Argon (LAr) of 760 tons. The idea of ICARUS as a neutrino detector was first proposed by C. Rubbia [185] in 1977 with a LAr TPC. It was situated in INFN Gran Sasso Laboratory (LNGS) in Italy. In the beginning, this detector with a total active mass of 476 tons [186], was developed in LNGS. ICARUS collected about 3000 neutrino events from the CNGSCERN to Gran Sasso neutrino beam corresponding to 8.6×10^{19} protons on target (POT) [34]. The detector moved to the Fermi lab in 2017 and is prepared for further operation.

XMASS detector at the Kamioka Observatory in Japan is a scintillation detector using LXe as a detector medium. In the field of neutrino search, XMASS is looking for solar neutrinos (pp/ 7Be) and neutrinoless double beta decay (0νββ).

The Super-Kamiokande (Super-K) detector [180] is a 50,000-ton tank of water located in a mine named Mozumi in Japan. The energy threshold of the neutrino detector is 3.5 MeV and the energy resolution is 14.2 % for solar and supernova neutrinos at energy 10 MeV [173].

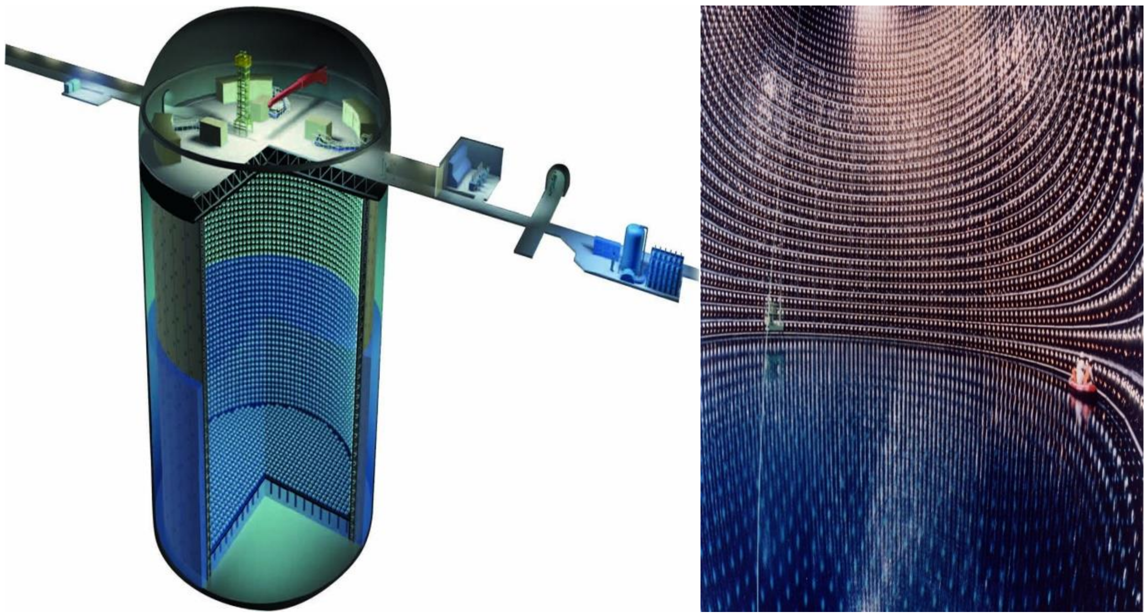

Figure 7.9 Left, Schematic overview of super-k detector and right, inside the detector. Figure is taken from ref. [188].

The Hyper-Kamiokande (Hyper-K) [187] detector is located in the Kamioka mine, Hida city, Gifu prefecture, Japan. The detector consists of a fiducial volume 10 times larger than that of Super-K. The rejection efficiency of cosmic-ray muons reaches more than 99.9% with the Hyper-Kamiokande detector.

The Jiangmen Underground Neutrino Observatory (JUNO) is a neutrino experiment located in the south of China, Jiangmen city in Guangdong province. It is designed to discover neutrino mass hierarchy and the search for solar neutrinos, atmospheric neutrinos, supernova neutrinos, indirect dark matter neutrinos, and many more neutrino searches [189]. It is a liquid scintillator detector with 20 kton of mass and uses large and small PMTs to measure scintillation.

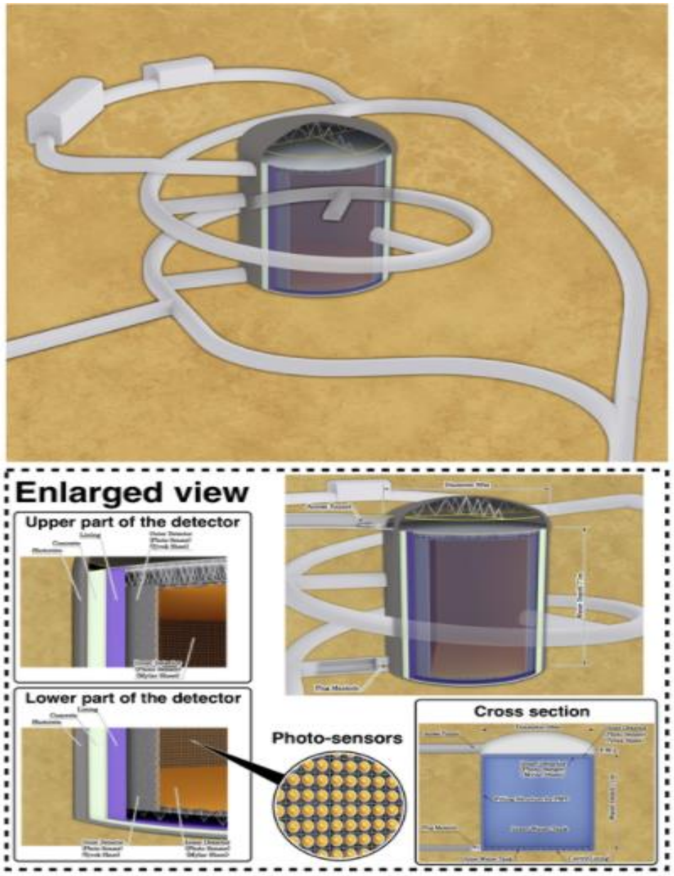

Figure 7.10 Schematic overview of the hyper-k detector. Figure is taken from ref. [187]

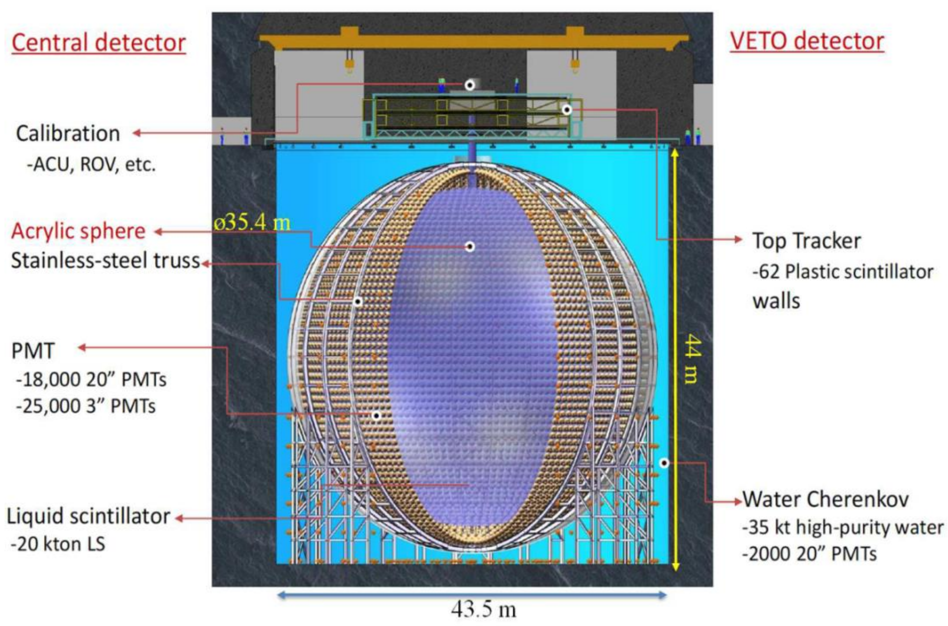

Figure 7.11 A schematic view of the JUNO detector. Figure is taken from ref. [189].

The other dedicated neutrino experiment at SNO (Sudbury Neutrino Observatory) near Sudbury, Ontario [190]. The new detector named SNO+ [191] introduced using the same SNO detector but using a liquid scintillator. It will be able to study low energy solar neutrinos, geo-neutrinos, and reactor neutrinos as well as to conduct a supernova search.

The Deep Underground Neutrino Experiment (DUNE) [192] consists of two neutrino detectors placed in an intense neutrino beam. One detector records particle interactions near the source of the beam at FERMI lab. The second detector is situated in the Sanford Underground research laboratory, 1300 kilometers away from the first one. It consists of 70,000 tons of LAr. This makes it suitable to collect supernova neutrinos if any will happen in the future.

IceCube [67] at the Amundsen, Scott South Pole is a giga-ton detector. When neutrinos interact with the ice, it creates other particles such as muons. The particles move through the detector and the particle's direction and energy are detected.

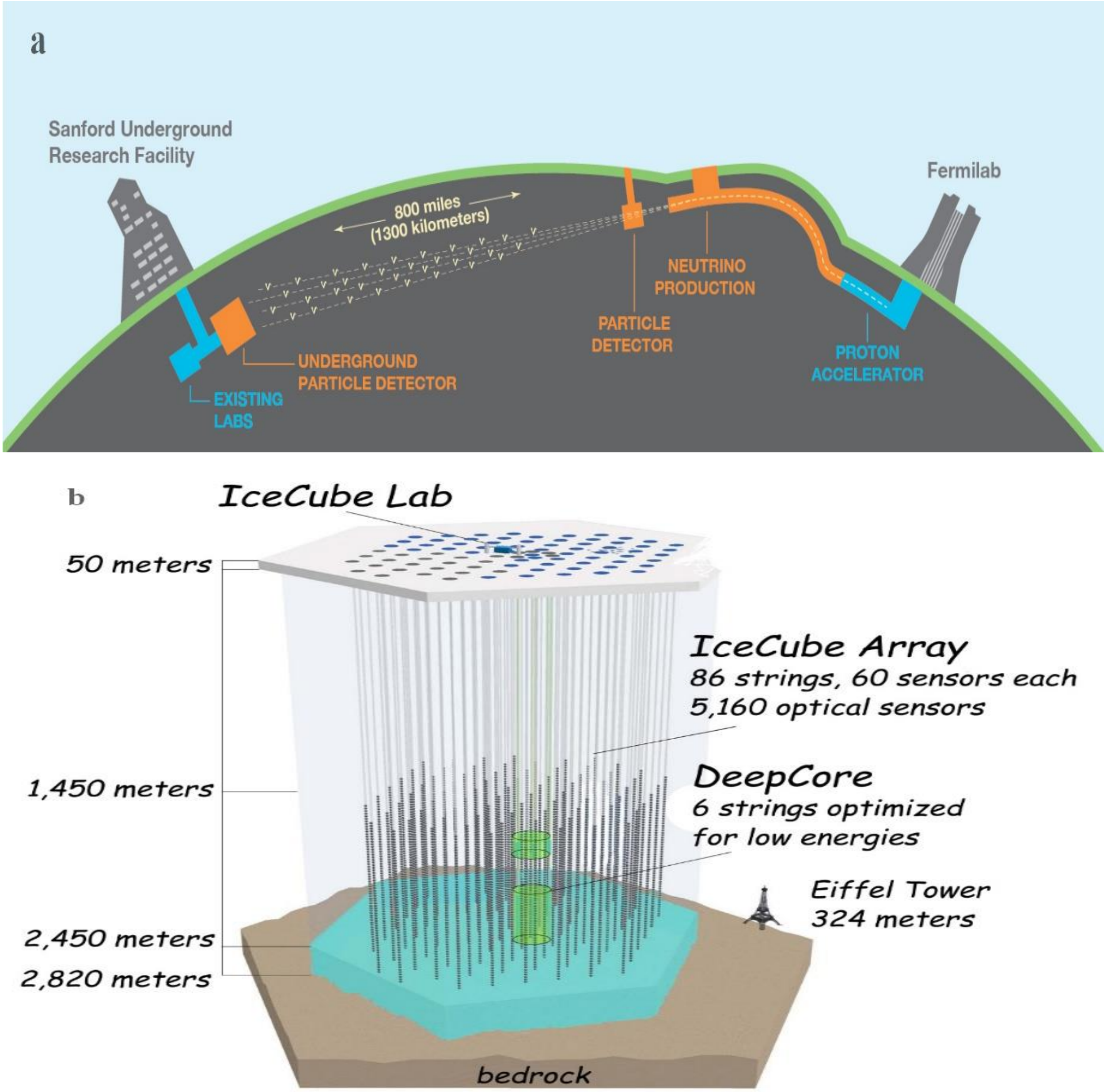

Figure 7.12 Pictorial representation of a) Dune lab from ref. [193] and b) Icecube lab from ref. [194].

8 Summary and outlook

Dual-phase (DP) TPCs are powerful tools, and in recent years, they have tremendously contributed to the search for dark matter (DM). The DP approach is an ingenious way to achieve sensitivity in low energy charge measurements. However, in the future, with ever-larger detectors, the DP technique might be too difficult to implement and might limit performance. Moreover, effects neglected until now might become a limiting factor, e.g., ripples and waves on the liquid level caused by liquid returning from purification.

Proportional scintillation around thin wires in LXe offers several unique features that might be beneficial. The evaluation of electroluminescence in LXe for DM applications was renewed by two teams, one from Columbia Astrophysics Lab (CAL) and the other from SJTU. They both explicitly conclude that the SP method can be used for future DM detectors. The single-phase LXe scheme offers many advantages for the design, operation, and stability of the detector. Removing the constraint that the drifting electrons must pass the liquid level has many consequences. The significant difference is that electrons can drift in any direction, i.e. we can configure multiple drift spaces.

We propose geometry with four drift spaces resulting in a reduction of the cathode HV by a factor of 4. At the same drift field, the attachment to electro-negative impurities of the drifting electrons is approximately reduced by the same factor, while electron diffusion is reduced by a factor of 2. For the anodes on top and bottom, we recommend aligning the anode wires with the shielding grids. An elegant realization of the TPC would have an additional anode structure in the center of the detector. An ambiguity in the drift space occupied by the event can be resolved by using staggered anode geometry. For achieving an adequate x-y position, we thus prefer geometry with two independent TPCs of half the length mounted on top of each other. In between the TPCs, two additional photon sensor arrays would eliminate the x-y positioning challenge.

We realize that if WIMPs are not detected with the next generation of detectors in the 4 – 8 ton range, we must make a large DM detector. If the signals are detected we want to understand DM, which means we need a very massive detector to acquire many events for analysis. Instead of wasting a lot of effort, time, and money we might as well build a very large detector now. This detector could be designed for a much larger energy range, and thus address many physics questions.

For the next generation of LXe WIMP detectors, the SP technique provides the opportunity for far-reaching physics research in DM (WIMP) search. Our proposed detector will be designed for a much larger energy range. There might be a lot of unknown physics to explore which we can study. Thus we aim is to build a large LXe WIMP detector that will work as an observatory to find exciting areas such as DBD, neutrinos, axions, and many more. With this detector, we can explore low-energy neutrinos (<50 keV range) and look for atmospheric neutrinos at an energy greater than 0.1 GeV. Similarly, for DBD search at high energies (MeV range).

For the effective use of the detector, we can use an isotope separation suggested by Y. Suzuki for all these searches mentioned above by separating the xenon into two parts, such as an even-isotope rich sample and an odd isotope sample. For example, we apply to search DBD by looking into isotopes greater than 131.5 and searching low-energy neutrinos in the odd sample (<131.5)—moreover, double electron capture search by the single isotopes in odd isotopes sample. We can use an isotope separation distillation column to separate isotopes of Xenon like the ARIA distillation column for the removal of ^{39}Ar. In this way we will separate the full range of xenon isotopes.

9 References

1. Profumo, S., L. Giani, and O.F. Piattella, *An introduction to particle dark matter*. Universe, 2019. **5**(10): p. 213.
2. Dolgoshein, B., V. Lebedenko, and B. Rodionov, *NEW METHOD OF REGISTRATION OF IONIZING-PARTICLE TRACKS IN CONDENSED MATTER*. 1970, Moscow Engineering Physics Inst.
3. Masuda, K., et al., *A liquid xenon proportional scintillation counter.* Nuclear Instruments and Methods, 1979. **160**(2): p. 247-253.
4. Miyajima, M., et al., *A self-triggered liquid xenon drift chamber by the use of proportional ionization or proportional scintillation.* Nuclear Instruments and Methods, 1979. **160**(2): p. 239-246.
5. Aprile, E., et al., *Measurements of proportional scintillation and electron multiplication in liquid xenon using thin wires.* Journal of Instrumentation, 2014. **9**(11): p. P11012.
6. Ye, T., K. Giboni, and X. Ji, *Initial evaluation of proportional scintillation in liquid Xenon for direct dark matter detection.* Journal of Instrumentation, 2014. **9**(12): p. P12007.
7. Giboni, K.L., et al., *A LN 2-based cooling system for a next-generation liquid xenon dark matter detector*. Nuclear Science and Techniques, 2020. **31**(8): p. 1-11.
8. Juyal, P., et al., *On the electrode configurations in a large single phase liquid xenon detector for dark matter searches.* Journal of Instrumentation, 2021. **16**(08): p. P08028.
9. Juyal, P., et al., *On proportional scintillation in very large liquid xenon detectors.* Nuclear Science and Techniques, 2020. **31**(9): p. 1-8.
10. Aprile, E., et al., *Excess electronic recoil events in XENON1T.* Physical Review D, 2020. **102**(7): p. 072004.
11. Suzuki, Y., *Low energy solar neutrino detection by using liquid xenon*, in *Low Energy Solar Neutrino Detection*. 2001, World Scientific. p. 81-90.
12. Alexander, T., et al., *DarkSide search for dark matter.* Journal of Instrumentation, 2013. **8**(11): p. C11021.

13. Nowak, J. and D. Collaboration, *Separating 39Ar from 40Ar by cryogenic distillation with Aria for dark matter searches.* European Physical Journal C: Particles and Fields, 2021.

14. Kapteyn, J., *No. 230. First attempt at a theory of the arrangement and motion of the sideral system.* Contributions from the Mount Wilson Observatory/Carnegie Institution of Washington, 1922. **230**: p. 1-27.

15. Jeans, J.H., *The motions of stars in a Kapteyn universe.* Monthly Notices of the Royal Astronomical Society, 1922. **82**: p. 122-132.

16. Oort, J.H., *Observational evidence confirming Lindblad's hypothesis of a rotation of the galactic system.* Bulletin of the Astronomical Institutes of the Netherlands, 1927. **3**: p. 275.

17. Zwicky, F., *On the Masses of Nebulae and of Clusters of Nebulae.* The Astrophysical Journal, 1937. **86**: p. 217.

18. Faber, S.M. and J. Gallagher, *Masses and mass-to-light ratios of galaxies.* Annual review of astronomy and astrophysics, 1979. **17**(1): p. 135-187.

19. Rubin, V.C. and W.K. Ford Jr, *Rotation of the Andromeda nebula from a spectroscopic survey of emission regions.* The Astrophysical Journal, 1970. **159**: p. 379.

20. Spergel, D.N., et al., *First-year Wilkinson Microwave Anisotropy Probe (WMAP)* observations: determination of cosmological parameters.* The Astrophysical Journal Supplement Series, 2003. **148**(1): p. 175.

21. Ade, P.A., et al., *Planck 2013 results. I. Overview of products and scientific results.* Astronomy & Astrophysics, 2014. **571**: p. A1.

22. Zwicky, F., *Die rotverschiebung von extragalaktischen nebeln.* Helvetica physica acta, 1933. **6**: p. 110-127.

23. Rubin, V.C., *Dark matter in spiral galaxies.* Scientific American, 1983. **248**(6): p. 96-109.

24. Begeman, K., A. Broeils, and R. Sanders, *Extended rotation curves of spiral galaxies: Dark haloes and modified dynamics.* Monthly Notices of the Royal Astronomical Society, 1991. **249**(3): p. 523-537.

25. Clowe, D., et al., *A direct empirical proof of the existence of dark matter.* The Astrophysical Journal Letters, 2006. **648**(2): p. L109.

26. Bergström, L., *Non-baryonic dark matter: observational evidence and detection methods.* Reports on Progress in Physics, 2000. **63**(5): p. 793.

27. Ryden, B., *Introduction to cosmology*. 2017: Cambridge University Press.

28. Penzias, A.A. and R.W. Wilson, *A measurement of excess antenna temperature at 4080 Mc/s.* The Astrophysical Journal, 1965. **142**: p. 419-421.

29. Shu, F.H. *cosmic microwave background*. 2019, November Available from: https://www.britannica.com/science/cosmic-microwave-background.

30. Cyburt, R.H., et al., *Big bang nucleosynthesis: Present status.* Reviews of Modern Physics, 2016. **88**(1): p. 015004.

31. Particle Data, G., et al., *Review of Particle Physics.* Physical Review D, 2012. **86**(1): p. 010001.

32. Nelson, C., et al., *The MACHO Project HST Follow-Up: The Large Magellanic Cloud Microlensing Source Stars.* arXiv preprint arXiv:0902.2213, 2009.

33. Rahal, Y., et al., *The EROS2 search for microlensing events towards the spiral arms: the complete seven season results.* Astronomy & Astrophysics, 2009. **500**(3): p. 1027-1044.

34. Farnese, C. and I. collaboration, *The ICARUS experiment.* Universe, 2019. **5**(2): p. 49.

35. Aguilar, A., et al., *Evidence for neutrino oscillations from the observation of ¯νe appearance in a ¯νμ beam.* Physical Review D, 2001. **64**(11): p. 112007.

36. Aguilar-Arevalo, A., et al., *Dark matter search in nucleon, pion, and electron channels from a proton beam dump with MiniBooNE.* Physical Review D, 2018. **98**(11): p. 112004.

37. Ko, Y., et al., *Sterile neutrino search at the NEOS experiment.* Physical review letters, 2017. **118**(12): p. 121802.

38. Alekseev, I., et al., *Search for sterile neutrinos at the DANSS experiment.* Physics Letters B, 2018. **787**: p. 56-63.

39. Peccei, R.D. and H.R. Quinn, *CP Conservation in the Presence of Pseudo particles.* Physical Review Letters, 1977. **38**(25): p. 1440-1443.

40. Duffy, L.D. and K. Van Bibber, *Axions as dark matter particles.* New Journal of Physics, 2009. **11**(10): p. 105008.

41. Sikivie, P., *Experimental tests of the" invisible" axion.* Physical Review Letters, 1983. **51**(16): p. 1415.

42. Shokair, T., et al., *Future directions in the microwave cavity search for dark matter axions.* International Journal of Modern Physics A, 2014. **29**(19): p. 1443004.

43. Arik, M., et al., *Search for solar axions by the CERN axion solar telescope with He 3 buffer gas: Closing the hot dark matter gap.* Physical review letters, 2014. **112**(9): p. 091302.

44. Irastorza, I.G., et al., *The International Axion Observatory (IAXO).* arXiv preprint arXiv:1201.3849, 2012.

45. Kim, J.E., *Weak-interaction singlet and strong CP invariance.* Physical Review Letters, 1979. **43**(2): p. 103.

46. Dine, M., W. Fischler, and M. Srednicki, *A simple solution to the strong CP problem with a harmless axion.* Physics letters B, 1981. **104**(3): p. 199-202.

47. Abbott, R., et al., *Gwtc-2: Compact binary coalescences observed by ligo and virgo during the first half of the third observing run.* Physical Review X, 2021. **11**(2): p. 021053.

48. al, R.S.e., *Laser Interferometer Space Antenna (LISA) A Response to the Astro2010 RFI for the Particle Astrophysics and Gravitation Panel.* April 2009.

49. Anelli, M., et al., *A facility to Search for Hidden Particles (SHiP) at the CERN SPS.* arXiv preprint arXiv:1504.04956, 2015.

50. Åkesson, T., et al., *Light dark matter eXperiment (LDMX).* arXiv preprint arXiv:1808.05219, 2018.

51. Battaglieri, M., et al., *US cosmic visions: new ideas in dark matter 2017: community report.* arXiv preprint arXiv:1707.04591, 2017.

52. Battaglieri, M., et al., *Dark matter search in a Beam-Dump eXperiment (BDX) at Jefferson Lab.* arXiv preprint arXiv:1607.01390, 2016.

53. Armengaud, E., et al., *Searching for low-mass dark matter particles with a massive Ge bolometer operated above ground.* Physical Review D, 2019. **99**(8): p. 082003.

54. Fabbrichesi, M., E. Gabrielli, and G. Lanfranchi, *The dark photon.* arXiv preprint arXiv:2005.01515, 2020.

55. Baltz, E.A., *Dark matter candidates.* arXiv preprint astro-ph/0412170, 2004.

56. Antoniadis, I., *A possible new dimension at a few TeV.* Physics Letters B, 1990. **246**(3-4): p. 377-384.

57. Griest, K. and M. Kamionkowski, *Supersymmetric dark matter*. Physics Reports, 2000. **333**: p. 167-182.

58. Collaboration, A., *The ATLAS experiment at the CERN large hadron collider*. 2008.

59. Chatrchyan, S., *CMS collaboration.* PHYSICAL REVIEW D Phys Rev D, 2013. **87**: p. 052006.

60. Gaskins, J.M., *A review of indirect searches for particle dark matter*. Contemporary Physics, 2016. **57**(4): p. 496-525.

61. Morselli, A., B. Canadas, and V. Vitale, *The Indirect Search for Dark Matter from the centre of the Galaxy with the Fermi LAT.* arXiv preprint arXiv:1012.2292, 2010.

62. Halzen, F. and D. Hooper, *The indirect search for dark matter with IceCube.* New Journal of Physics, 2009. **11**(10): p. 105019.

63. Tanaka, T., et al., *An indirect search for weakly interacting massive particles in the sun using 3109.6 days of upward-going muons in Super-Kamiokande.* The Astrophysical Journal, 2011. **742**(2): p. 78.

64. Athron, P., et al., *Model-independent analysis of the DAMPE excess.* Journal of High Energy Physics, 2018. **2018**(2): p. 1-30.

65. Goy, C. *Indirect search for dark matter with AMS*. in *Journal of Physics: Conference Series*. 2006. IOP Publishing.

66. Aguilar, M., et al., *First result from the Alpha Magnetic Spectrometer on the International Space Station: precision measurement of the positron fraction in primary cosmic rays of 0.5–350 GeV.* Physical Review Letters, 2013. **110**(14): p. 141102.

67. Aartsen, M., et al., *Multipole analysis of IceCube data to search for dark matter accumulated in the Galactic halo.* The European Physical Journal C, 2015. **75**(1): p. 1-16.

68. Goodman, M.W. and E. Witten, *Detectability of certain dark-matter candidates.* Physical Review D, 1985. **31**(12): p. 3059.

69. Drukier, A.K., K. Freese, and D.N. Spergel, *Detecting cold dark-matter candidates.* Physical Review D, 1986. **33**(12): p. 3495.

70. Cebrian, S., et al., *First results of the IGEX dark matter experiment at the Canfranc Underground Laboratory.* Nuclear Physics B-Proceedings Supplements, 2001. **95**(1-3): p. 229-232.

71. Agnese, R., et al., *Search for low-mass dark matter with CDMSlite using a profile likelihood fit.* Physical Review D, 2019. **99**(6): p. 062001.

72. Ma, H., et al. *Results of direct dark matter detection with CDEX experiment at CJPL*. in *Journal of Physics: Conference Series*. 2020. IOP Publishing.

73. Adams, D., et al., *Improved Limit on Neutrinoless Double-Beta Decay in Te 130 with CUORE.* Physical review letters, 2020. **124**(12): p. 122501.

74. Angloher, G., et al., *Limits on WIMP dark matter using sapphire cryogenic detectors.* Astroparticle Physics, 2002. **18**(1): p. 43-55.

75. Bernabei, R., et al., *The dama/libra apparatus.* Nuclear Instruments and Methods in Physics Research Section A: Accelerators, Spectrometers, Detectors and Associated Equipment, 2008. **592**(3): p. 297-315.

76. Ajaj, R., et al., *Search for dark matter with a 231-day exposure of liquid argon using DEAP-3600 at SNOLAB.* Physical Review D, 2019. **100**(2): p. 022004.

77. Abe, K., et al., *XMASS detector*. Nuclear Instruments and Methods in Physics Research Section A: Accelerators, Spectrometers, Detectors and Associated Equipment, 2013. **716**: p. 78-85.

78. Lang, R.F., *The CRESST-II Experiment.* arXiv preprint arXiv:0805.4705, 2008.

79. Cebrian, S., et al., *First results of the ROSEBUD dark matter experiment.* Astroparticle Physics, 2001. **15**(1): p. 79-85.

80. Aprile, E., et al., *Physics reach of the XENON1T dark matter experiment.* Journal of Cosmology and Astroparticle Physics, 2016. **2016**(04): p. 027.

81. Akerib, D., et al., *Results from a search for dark matter in the complete LUX exposure.* Physical review letters, 2017. **118**(2): p. 021303.

82. Zhang, H., et al., *Dark matter direct search sensitivity of the PandaX-4T experiment.* Science China Physics, Mechanics & Astronomy, 2019. **62**(3): p. 1-9.

83. Agnes, P., et al., *DarkSide-50 532-day dark matter search with low-radioactivity argon.* Physical Review D, 2018. **98**(10): p. 102006.

84. Aalbers, J., et al., *DARWIN: towards the ultimate dark matter detector*. Journal of Cosmology and Astroparticle Physics, 2016. **2016**(11): p. 017.

85. Freedman, D.Z., *Coherent effects of a weak neutral current.* Physical Review D, 1974. **9**(5): p. 1389.

86. Cabrera, B., L.M. Krauss, and F. Wilczek, *Bolometric detection of neutrinos.* Physical Review Letters, 1985. **55**(1): p. 25.

87. Ianni, A., *Review of technical features in underground laboratories.* International Journal of Modern Physics A, 2017. **32**(30): p. 1743001.

88. Wu, Y.-C., et al., *Measurement of cosmic ray flux in China JinPing Underground Laboratory.* arXiv preprint arXiv:1305.0899, 2013.

89. Aprile, E., et al., *Lowering the radioactivity of the photomultiplier tubes for the XENON1T dark matter experiment.* The European Physical Journal C, 2015. **75**(11): p. 1-10.

90. Zhang, T., et al., *Low background stainless steel for the pressure vessel in the PandaX-II dark matter experiment.* Journal of Instrumentation, 2016. **11**(09): p. T09004.

91. Pretzl, K., *Cryogenic Detectors*, in *Particle Physics Reference Library*. 2020, Springer. p. 871-912.

92. Shutt, T., et al., *Measurement of ionization and phonon production by nuclear recoils in a 60 g crystal of germanium at 25 mK.* Physical review letters, 1992. **69**(24): p. 3425.

93. Luke, P., et al., *Calorimetric ionization detector.* Nuclear Instruments and Methods in Physics Research Section A: Accelerators, Spectrometers, Detectors and Associated Equipment, 1990. **289**(3): p. 406-409.

94. Ibe, M., et al., *Migdal effect in dark matter direct detection experiments.* Journal of High Energy Physics, 2018. **2018**(3): p. 1-36.

95. Tovey, D., et al., *Measurement of scintillation efficiencies and pulse-shapes for nuclear recoils in NaI (Tl) and CaF2 (Eu) at low energies for dark matter experiments.* Physics Letters B, 1998. **433**(1-2): p. 150-155.

96. Kim, S., H. Kim, and Y. Kim, *Scintillator-based detectors for dark matter searches I.* New Journal of Physics, 2010. **12**(7): p. 075003.

97. Amaré, J., et al., *First results on dark matter annual modulation from the ANAIS-112 experiment.* Physical review letters, 2019. **123**(3): p. 031301.

98. Park, H., et al., *Neutron beam test of CsI crystal for dark matter search.* Nuclear Instruments and Methods in Physics Research Section A: Accelerators, Spectrometers, Detectors and Associated Equipment, 2002. **491**(3): p. 460-469.

99. Amaré, J., et al. *ANAIS-112 status: two years results on annual modulation*. in *Journal of Physics: Conference Series*. 2020. IOP Publishing.

100. Coarasa, I., et al., *ANAIS-112 sensitivity in the search for dark matter annual modulation.* The European Physical Journal C, 2019. **79**(3): p. 1-8.

101. Adhikari, G., et al., *Initial performance of the COSINE-100 experiment.* The European Physical Journal C, 2018. **78**(2): p. 1-19.

102. Adhikari, G., et al., *Search for a dark matter-induced annual modulation signal in NaI (Tl) with the COSINE-100 experiment.* Physical review letters, 2019. **123**(3): p. 031302.

103. Aguilar-Arevalo, A., et al., *Constraints on light dark matter particles interacting with electrons from DAMIC at SNOLAB.* Physical review letters, 2019. **123**(18): p. 181802.

104. Liu, Z., et al., *Constraints on spin-independent nucleus scattering with sub-GeV weakly interacting massive particle dark matter from the CDEX-1B experiment at the China Jinping underground laboratory.* Physical review letters, 2019. **123**(16): p. 161301.

105. Jiang, H., et al., *Limits on light weakly interacting massive particles from the first 102.8 kg× day data of the CDEX-10 experiment.* Physical review letters, 2018. **120**(24): p. 241301.

106. Amole, C., et al., *Dark matter search results from the complete exposure of the PICO-60 C 3 F 8 bubble chamber.* Physical Review D, 2019. **100**(2): p. 022001.

107. Akerib, D., et al., *The lux-zeplin (lz) experiment.* Nuclear Instruments and Methods in Physics Research Section A: Accelerators, Spectrometers, Detectors and Associated Equipment, 2020. **953**: p. 163047.

108. Agnes, P., et al., *The veto system of the DarkSide-50 experiment.* Journal of Instrumentation, 2016. **11**(03): p. P03016.

109. Aprile, E., et al., *The XENON1T dark matter experiment.* The European Physical Journal C, 2017. **77**(12): p. 1-23.

110. Abe, K., et al., *A direct dark matter search in XMASS-I.* Physics Letters B, 2019. **789**: p. 45-53.

111. Abe, K., et al., *Search for exotic neutrino-electron interactions using solar neutrinos in XMASS-I.* Physics Letters B, 2020. **809**: p. 135741.

112. Aprile, E., et al., *Design and performance of the XENON10 dark matter experiment.* Astroparticle Physics, 2011. **34**(9): p. 679-698.

113. Aprile, E., et al., *XENON100 dark matter results from a combination of 477 live days.* Physical Review D, 2016. **94**(12): p. 122001.

114. Aprile, E., et al., *Projected WIMP sensitivity of the XENONnT dark matter experiment.* Journal of Cosmology and Astroparticle Physics, 2020. **2020**(11): p. 031.

115. Akerib, D.S., et al., *First results from the LUX dark matter experiment at the Sanford Underground Research Facility*. Physical review letters, 2014. **112**(9): p. 091303.

116. Schumann, M., et al., *Dark matter sensitivity of multi-ton liquid xenon detectors.* Journal of cosmology and astroparticle physics, 2015. **2015**(10): p. 016.

117. Agostini, F., et al., *Sensitivity of the DARWIN observatory to the neutrinoless double beta decay of 136Xe.* The European Physical Journal C, 2020. **80**(9): p. 1-11.

118. Li, J., et al., *The second-phase development of the China JinPing underground Laboratory.* Physics Procedia, 2015. **61**: p. 576-585.

119. Cao, X., et al., *PandaX: a liquid xenon dark matter experiment at CJPL.* Science China Physics, Mechanics & Astronomy, 2014. **57**(8): p. 1476-1494.

120. Tan, A., et al., *Dark matter results from first 98.7 days of data from the PandaX-II experiment.* Physical review letters, 2016. **117**(12): p. 121303.

121. Chen, X., et al., *PandaX-III: Searching for neutrinoless double beta decay with high pressure 136 Xe gas time projection chambers.* Science China Physics, Mechanics & Astronomy, 2017. **60**(6): p. 061011.

122. Liu, J., X. Chen, and X. Ji, *Current status of direct dark matter detection experiments.* Nature Physics, 2017. **13**(3): p. 212-216.

123. Meng, Y., et al., *Dark matter search results from the PandaX-4T commissioning run.* arXiv preprint arXiv:2107.13438, 2021.

124. Agnes, P., et al., *First results from the DarkSide-50 dark matter experiment at Laboratori Nazionali del Gran Sasso.* Physics Letters B, 2015. **743**: p. 456-466.

125. Agnes, P., et al., *Low-mass dark matter search with the DarkSide-50 experiment.* Physical review letters, 2018. **121**(8): p. 081307.

126. Bernabei, R., et al., *Liquid noble gases for dark matter searches: An updated survey.* International Journal of Modern Physics A, 2015. **30**(26): p. 1530053.

127. Schumann, M., *Dark matter search with liquid noble gases.* arXiv preprint arXiv:1206.2169, 2012.

128. Chepel, V. and H. Araújo, *Liquid noble gas detectors for low energy particle physics.* Journal of Instrumentation, 2013. **8**(04): p. R04001.

129. Feltesse, J. and L.N. Gas, *Warm Liquid Detectors.* Nucl. Instrum. Meth. A. **283**.

130. Rielage, K., et al., *Update on the MiniCLEAN dark matter experiment.* Physics Procedia, 2015. **61**: p. 144-152.

131. Bueno, A., et al., *Observation of coherent neutrino-nucleus elastic scattering at a beta beam.* Physical Review D, 2006. **74**(3): p. 033010.

132. Time Projection Chamber. *Working principle of a TPC*. 2021; Available from: https://www.lctpc.org/sites/sites_custom/site_lctpc/content/e8/e57671/e21013/TPCeng.jpg.

133. Platzman, R., *Total ionization in gases by high-energy particles: An appraisal of our understanding.* The International Journal of Applied Radiation and Isotopes, 1961. **10**(2-3): p. 116-127.

134. Mu, W. and X. Ji, *Ionization yield from nuclear recoils in liquid-xenon dark matter detection.* Astroparticle Physics, 2015. **62**: p. 108-114.

135. Manzur, A., et al., *Scintillation efficiency and ionization yield of liquid xenon for monoenergetic nuclear recoils down to 4 keV.* Physical Review C, 2010. **81**(2): p. 025808.

136. Yamashita, M., et al., *Scintillation response of liquid Xe surrounded by PTFE reflector for gamma rays.* Nuclear Instruments and Methods in Physics Research Section A: Accelerators, Spectrometers, Detectors and Associated Equipment, 2004. **535**(3): p. 692-698.

137. Aprile, E., et al., *Observation of anticorrelation between scintillation and ionization for MeV gamma rays in liquid xenon.* Physical Review B, 2007. **76**(1): p. 014115.

138. Hogenbirk, E., et al., *Precision measurements of the scintillation pulse shape for low-energy recoils in liquid xenon.* Journal of Instrumentation, 2018. **13**(05): p. P05016.

139. Wang, Q., et al., *Results of dark matter search using the full PandaX-II exposure.* Chinese Physics C, 2020. **44**(12): p. 125001.

140. Giboni, K.L., *On future multi-ton dark matter detectors with proportional scintillation in LXe*. 2018: XeSAT2018, Waseda, Japan.

141. Derenzo, S.E., et al., *Electron avalanche in liquid xenon.* Physical Review A, 1974. **9**(6): p. 2582.

142. Aprile, E. and T. Doke, *Liquid xenon detectors for particle physics and astrophysics.* Reviews of Modern Physics, 2010. **82**(3): p. 2053.

143. Gatti, E., et al., *Considerations for the design of a time projection liquid argon ionization chamber.* IEEE Transactions on Nuclear Science, 1979. **26**(2): p. 2910-2932.

144. Bunemann, O., T. Cranshaw, and J. Harvey, *Design of grid ionization chambers.* Canadian journal of research, 1949. **27**(5): p. 191-206.

145. Frisch, O.R., *Isotope analysis uranium sample by means of their alpha ray groups*. British atomic energy.

146. Loebich, O., *The optical properties of gold.* Gold bulletin, 1972. **5**(1): p. 2-10.

147. Namwongsa, P., et al., *Electron Recoil rejection by decay time measurement in large liquid Xenon detectors.* Journal of Instrumentation, 2017. **12**(04): p. P04019.

148. Baker, S. and R.D. Cousins, *Clarification of the use of chi-square and likelihood functions in fits to histograms.* Nuclear Instruments and Methods in Physics Research, 1984. **221**(2): p. 437-442.

149. Ishida, N., et al., *Attenuation length measurements of scintillation light in liquid rare gases and their mixtures using an improved reflection suppresser.* Nuclear Instruments and Methods in Physics Research Section A: Accelerators, Spectrometers, Detectors and Associated Equipment, 1997. **384**(2-3): p. 380-386.

150. Model R12699 by Hamamatsu Photonics KK, J.

151. L. Baudis (XENON Coll.), p.c., *Two Hamamatsu R12699-406-M4 tubes were measured in the GATOR detector of the Zurich group at the LNGS.*

152. Giuliani, F., *A nonstandard Pulse Shape Discrimination parameter to discern recoiling e- and nuclei in LXe scintillator detectors*. XeSAT2018, WASEDA University, Tokyo, Japan, to be published.

153. Yoshizawa, H., private communication.

154. Ogawa, S. and M.I. Collaboration, *Liquid xenon calorimeter for MEG II experiment with VUV-sensitive MPPCs.* Nuclear Instruments and Methods in Physics Research Section A: Accelerators, Spectrometers, Detectors and Associated Equipment, 2017. **845**: p. 528-532.

155. Haefner, J., et al., *Reflectance dependence of polytetrafluoroethylene on thickness for xenon scintillation light.* Nuclear Instruments and Methods in Physics Research Section A: Accelerators, Spectrometers, Detectors and Associated Equipment, 2017. **856**: p. 86-91.

156. Elsied, A., K. Giboni, and X. Ji, *Alternative connection scheme for PMTs in large, low energy LXe detectors.* Journal of Instrumentation, 2015. **10**(01): p. T01003.

157. Giboni, K., et al., *A liquid xenon development and test system.* Journal of Instrumentation, 2014. **9**(04): p. T04006.

158. Haruyama, T., et al. *LN2-free Operation of the MEG Liquid Xenon Calorimeter by using a High-power Pulse Tube Cryocooler*. in *AIP Conference Proceedings*. 2006. American Institute of Physics.

159. Gong, H., et al., *The cryogenic system for the Panda-X dark matter search experiment.* Journal of Instrumentation, 2013. **8**(01): p. P01002.

160. Aprile, E., et al., *Online 222Rn removal by cryogenic distillation in the XENON100 experiment.* The European Physical Journal C, 2017. **77**(6): p. 1-8.

161. Martin (Mort) Schmidt. *Vapor intrusion fundamentals: Part 16 – radon*. 2015; Available from: http://www.coxcolvin.com/vapor-intrusion-fundamentals-part16-radon/.

162. Avignone III, F.T., S.R. Elliott, and J. Engel, *Double beta decay, Majorana neutrinos, and neutrino mass.* Reviews of Modern Physics, 2008. **80**(2): p. 481.

163. Lin, H., et al., *Design and commissioning of a 600 L time projection chamber with Microbulk Micromegas.* Journal of Instrumentation, 2018. **13**(06): p. P06012.

164. Wang, S., *PandaX-III high pressure xenon TPC for Neutrinoless Double Beta Decay search.* Nuclear Instruments and Methods in Physics Research Section A: Accelerators, Spectrometers, Detectors and Associated Equipment, 2020. **958**: p. 162439.

165. Gomez-Cadenas, J., *Status of NEXT and prospects for a future Next Array apparatUS with Improved CApAbilities (NAUSICAA).* PoS NEUTEL2017, 2018. **32**.

166. Obara, S., et al., *AXEL: High-pressure Xe gas TPC for BG-free 0v2β decay search.* Nuclear Instruments and Methods in Physics Research Section A: Accelerators, Spectrometers, Detectors and Associated Equipment, 2020. **958**: p. 162803.

167. Majorana. *The MAJORANA neutrinoless double-beta decay experiment*. 2019; Available from: https://www.npl.washington.edu/majorana/majorana-experiment.

168. Abe, K., et al., *Search for solar axions in XMASS, a large liquid-xenon detector.* Physics Letters B, 2013. **724**(1-3): p. 46-50.

169. Aprile, E., *Observation of two-neutrino double electron capture in 124Xe with XENON1T.* Nature, 2019. **568**(7753).

170. Martínez-Lema, G., et al., *Sensitivity of the NEXT experiment to Xe-124 double electron capture.* Journal of High Energy Physics, 2021. **2021**(2): p. 1-25.

171. Abe, K., et al., *Search for two-neutrino double electron capture on 124Xe with the XMASS-I detector.* Physics Letters B, 2016. **759**: p. 64-68.

172. Kajita, T., *Atmospheric neutrinos and discovery of neutrino oscillations.* Proceedings of the Japan Academy, Series B, 2010. **86**(4): p. 303-321.

173. Suzuki, Y., *The super-Kamiokande experiment.* The European Physical Journal C, 2019. **79**(4): p. 1-18.

174. Honda, M., et al., *New calculation of the atmospheric neutrino flux in a three-dimensional scheme.* Physical Review D, 2004. **70**(4): p. 043008.

175. Barr, G., et al., *Three-dimensional calculation of atmospheric neutrinos.* Physical Review D, 2004. **70**(2): p. 023006.

176. Battistoni, G.a.F., A. and Montaruli, T. and Sala, P. R., *The FLUKA atmospheric neutrino flux calculation.* Astropart. Phys., 2003. **19**: p. 269--290.

177. Reines, F., et al., *Evidence for high-energy cosmic-ray neutrino interactions.* Physical Review Letters, 1965. **15**(9): p. 429.

178. Achar, C., et al., *Detection of muons produced by cosmic ray neutrinos deep underground.* Physics letters, 1965. **18**(2): p. 196-199.

179. Gaisser, T.K., *Atmospheric Neutrinos.* Nuclear Physics B - Proceedings Supplements, 2011. **221**: p. 85-89.

180. Fukuda, Y., et al., *Evidence for oscillation of atmospheric neutrinos.* Physical Review Letters, 1998. **81**(8): p. 1562.

181. Francisco R. Villatoro. *Borexino observed neutrinos from the first pp reaction in the sun's core*. 2014; Available from: https://francis.naukas.com/files/2014/08/Dibujo20140829-Solar-neutrino-energy-spectrum-borexino-nature-com.jpg.

182. Chakraborty, S., P. Bhattacharjee, and K. Kar, *Observing supernova neutrino light curve in future dark matter detectors.* Physical Review D, 2014. **89**(1): p. 013011.

183. Raj, N., V. Takhistov, and S.J. Witte, *Presupernova neutrinos in large dark matter direct detection experiments.* Physical Review D, 2020. **101**(4): p. 043008.

184. Collaboration, I., *Evidence for high-energy extraterrestrial neutrinos at the IceCube detector.* Science, 2013. **342**(6161).

185. Rubbia, C., *The liquid-argon time projection chamber: a new concept for neutrino detectors*. 1977.

186. Rubbia, C., et al., *Underground operation of the ICARUS T600 LAr-TPC: first results.* Journal of Instrumentation, 2011. **6**(07): p. P07011.

187. Di Lodovico, F. and H.-K. Collaboration. *The hyper-kamiokande experiment*. in *Journal of Physics: Conference Series*. 2017. IOP Publishing.

188. T. Kajita. *Super-kamiokande detector* 2016; Available from: https://www.japan.go.jp/tomodachi/2016/newyear2016/dr_takaaki_kajita.html.

189. Giaz, A., *Status and perspectives of the JUNO experiment.* arXiv preprint arXiv:1804.03575, 2018.

190. McDonald, A.B., *The Sudbury Neutrino Observatory: Observation of flavor change for solar neutrinos.* Annalen der Physik, 2016. **528**(6): p. 469-480.

191. Kamdin, K., *Understanding the sno+ detector*. Physics Procedia, 2015. **61**: p. 719-723.

192. Krasnov, I., *DUNE prospects in the search for sterile neutrinos.* Physical Review D, 2019. **100**(7): p. 075023.

193. Deep Underground Neutrino Experiment. *An international experiment for neutrino science*. 2020; Available from: https://www.dunescience.org.

194. CENTER, N. *Into the ice: Completing the icecube neutrino observatory*. 2021; Available from: https://newscenter.lbl.gov/2010/12/17/completing-icecube/.

10 Acknowledgements

To be a student of Shanghai Jiao Tong University is a big achievement in itself. I am fortunate to get admission to the department of physics and astronomy at SJTU as a doctoral student. First, I would like to express my sincere gratitude to my supervisor Dr. Karl Ludwig Giboni, for his continuous support during my Ph.D. study and related research, for his patience, motivation, and immense knowledge of the subject. His guidance helped me in all the time of research and writing of this thesis. He is not only a thesis guide for me but also a pathfinder. I remember that when I met him for the first time in the university after a long conversation through emails. I was a bit nervous that day, but all the nervousness went away when I met him due to his kind and friendly behavior. We had a light conversation about my previous study and some other stuff. He introduced me to the other fellow students on that day and gave a laboratory tour. To this date, I am always thankful for his constant concern and support. I am not writing this just for the sake of writing. Still, I believe that I and other fellow students, teachers, and staff also appreciate him because of his friendly nature and ability to pass on the knowledge with his experiences. He not only guides me in the research field but also provides life lessons. With his lifetime experience in the Dark matter field and related studies, I have learned and understood a lot about this field. He shared his experiences and challenges in the science field, which helped me enlighten the field's deep knowledge. I have a lot more to say about him, but words do not justify his dedication and commitment in the research area.

I want to thank Prof. Xiangdong Ji and Prof. Jianglai Liu for their continuous support. They had been providing us their constant support during the pandemic times. I got a chance to meet Prof. X. Ji only once when he gave a lecture on Morjona Neutrinos, which was quite interesting. I admire him because of this way of presenting. Although I did not get a chance to connect with him personally, his guidance and support have always been with us.

I want to thank Prof. Jianglai Liu too. He is a young ideal for everyone. He has helped us whenever we need any suggestions and assistance. Unfortunately, I did not get a chance to work with him, but I attended his classes in the first year of my study. He is genuinely an excellent teacher. His insightful comments and suggestions always admire me.

My sincere thanks also go to Dr. Zhao Li for helping me in the laboratory work and Dr. Xun Chen for dealing with any simulation and software work.

As I am the single student in the project under my supervisor, I did not get enough time to mingle with other students. But I met many of them during seminars and PandaX collaboration meetings. I want to thank every student of the PandaX group whom I met and shared life experiences and academic learnings. I want to mention that, although I was not working with other students, when I needed them, they always helped me.

I want to thank the School of Physics and Astronomy for giving me a chance to enhance my knowledge. These years of my doctoral study in the SJTU will immensely positively change my further progress.

Lastly, I would like to thank my family members who have always supported me through thick and thin. They have always encouraged me towards achieving my goals throughout my study. My parents and my in-laws have always played a vital role. It is hard for every parent not to see their child for a long time, but they always inspire us to pursue our dreams and ambitions. A Special thanks to my brother Gaurav Juyal who has helped me with proofreading and English composition for my thesis. I cannot imagine my life and my doctoral study without the support of my husband, Vinay Naithani. He has been with me with every step. When I experience any trouble and confusion, he continuously supports me and provides solutions to deal with challenges. He always believes in my ability and encourages me to do my best. My Ph.D. study and thesis are possible because of all of them.

11 Published Papers

1. P. Juyal, K. L. Giboni, X. Ji, J. Liu, On the electrode configurations in a large single phase liquid xenon detector for dark matter searches, JINST 16 P08028, (2021), https://doi.org/10.1088/1748-0221/16/08/P08028

2. Pratibha Juyal, Karl-Ludwig Giboni, Xiang-Dong Ji, Jiang-Lai Liu, On proportional scintillation in very large liquid xenon detectors, Nucl. Sci. Tech. 31,379 93 (2020). doi: 10.1007/s41365-020-00797-4

3. Karl Ludwig Giboni, Pratibha Juyal, Elena Aprile, Yun Zhang, Junji Naganoma, A LN2-based cooling system for a next-generation liquid xenon dark matter detector, NUCL SCI TECH 31, 76 (2020). doi.org/10.1007/s41365-020-00786-7

4. P. Chaiyabin, K.L. Giboni, K. Han, X. Ji, P. Juyal, C. Kobdaj, J. Liu, J. Lomon, N. Pasaja, P. Poolcharuansin, S. Rujirawat, P. Songsiriritthigul, Y. Yan and L. Zhao, Novel field cage design for the PandaX III double beta decay experiment, 2017 JINST 12 P10014